Methods for Physiological Artifact Correction in Oscillating Steady State Imaging

by

Amos Cao

A dissertation submitted in partial fulfillment
of the requirements for the degree of
Doctor of Philosophy
(Biomedical Engineering)
in The University of Michigan
2020

Doctoral Committee:

Professor Douglas C. Noll, Chair
Professor Jeffrey A. Fessler
Associate Research Scientist Jon-Fredrik Nielsen
Associate Professor Nicole Seiberlich

Amos A. Cao

amoscao@umich.edu

ORCID iD: 0000-0003-0465-7053

ACKNOWLEDGEMENTS

It is often said that doing a Ph.D. is a non-linear process. Now that I am concluding mine, I can verify that this is indeed the case. I am grateful that my meandering path has been full of remarkable people who have helped me improve as a scientist and as a person. I feel honored to recognize a fraction of their influence in the following pages.

First and foremost, I thank Doug Noll, my research advisor and dissertation chair, for whom I owe much of my understanding and intuition of MRI. In addition to a great teacher, Doug is an excellent mentor who has always enabled me to work on what I find meaningful. Doug has helped me develop independence as a researcher by letting me fail in a controlled way, yet providing direct support when I have needed it. Most importantly, Doug has always provided me feedback that was free from judgement, which has taught me to see value in my own work, rather than seek the validation of others. I hope to emulate these qualities of mentorship in the future.

I thank Jon-Fredrik Nielsen for the technical mentorship that had enabled much of the work presented in this thesis, long before he agreed to serve on my committee. I owe any early success I had on the 3T system to Jon and his ingenious pulse programming platform, TOPPE. I am grateful to Jon for allowing me the freedom to contribute changes into TOPPE that hopefully will help a future student as Jon has helped me. I also am appreciative of the many times that Jon would entertain my impromptu questions and project ideas, usually as I walked past his office door on the way in or out of the building.

I thank Jeff Fessler for being a role model in both research and teaching. I had long held a belief that I had missed the boat on learning linear algebra and signal processing, based on the fact that I did not know how to do matrix multiplication in my 4th year of graduate school. Despite this, Jeff graciously allowed me to attend his lab meetings and offered his time to answer my questions. The patience he exhibited in these interactions helped me build confidence to formally take an EECS signal processing class. The methods I learned in that class are the basis for the majority of this thesis.

The final committee member I thank is Nicole Seiberlich. In the short time that I have known her, Nicole has provided invaluable feedback about my work and continuously challenged me to consider a broader picture. I am grateful for her taking time from her start at Michigan to help me complete my ending. I am also grateful for her contagious enthusiasm for MRI, which has helped me maintain the energy to finish my work.

I owe great thanks to Joan Greve for being my first mentor at Michigan. Joan has taught me many succinct lessons on good scientific practices that I will carry forever, such as to always be skeptical of my data, or to start problem solving with simple approaches. I am grateful that I learned to conduct animal research from Joan, who has always emphasized and exhibited empathy toward the animals that help us understand and improve human life. Working with Joan was the deciding factor in choosing Michigan, and I am thankful for her continuous encouragement and support.

Thank you to my contemporaries who have made Michigan a great place to work: Anish, Cameron, Caroline, Claire, Colleen, David, Dinank, Jonas, Kathleen, Lianli, Melissa, Michelle, Naveen, Olivia, Paige, Shouchang, Sydney, Tianrui, Mariama, and Xijia. I appreciate all the times we have helped each other explore new ideas, run experiments, and kept each other company late into the night. I have learned a great

deal from all of you and wish you good luck in finding free food around campus.

Thank you to the faculty and staff of the fMRI lab: Scott Peltier for helping me improve my understanding of fMRI methodology and helping me get my experiments to work, Krissanne for being the unsung hero of our computing resources, and Luis Hernandez-Garcia for helping me learn MRI physics and looking out for the safety of the lab. Thank you to Ryan Smith and Dina Salhani for supporting me in getting my fMRI experiments to work, and for letting me test things in between scheduled studies. Thank you to Barb Hibbard and Theresa Russ who helped me with the logistics of human subject testing and been patient when I forgot to include the shortcode on my paperwork. Thank you to Chuck Nicholas and Erik Keup for helping the fMRI lab keep our computing resources running, backing up our work, and generally helping us avert disaster.

Thank you to Steve and Susan McFerran, the coaches of the Michigan Ballroom Dance Team. I never thought that I would take up ballroom dance as a hobby, let alone compete in it. Dancing has been a source of happiness and refuge for all the tough times in graduate school, and has taught me that being initially bad at something is never indicative of your potential to improve. I am thankful for Steve and Susan playing an essential role in my personal and dance growth for the last five years.

I thank Cassidy Lukaart for being a great friend. From getting bitten by a squirrel to taking welding classes, I'm grateful for our many adventures and look forward to the ones to come.

And finally, thank you to my family for supporting my lifelong desire to be a scientist. Through driving me to LEGO robotics classes on weekends or helping me enroll in high school programming classes, I am thankful for having parents that have always enabled me to pursue my scientific interests. I am appreciative of my family's love and support, no matter where my studies have taken me.

This work was supported by the Rackham Merit Fellowship Program and by the National Institute of Biomedical Imaging and Bioengineering (NIBIB) and National Institute of Neurological Disorders and Stroke (NINDS) through grants R01 EB023618 and U01 EB026977.

TABLE OF CONTENTS

LIST OF FIGURES

Figure

LIST OF TABLES

Table

LIST OF APPENDICES

Appendix

ABSTRACT

Functional magnetic resonance imaging (fMRI) is a neuroimaging technique that provides an unparalleled ability to non-invasively study brain activity. Since its inception in the early 1990s, fMRI has become a dominant tool in studying neurological responses to tasks and stimuli and has been critical in our evolving understanding of brain mapping. These achievements in neuroscience would not be possible without critical breakthroughs in MRI theory and hardware advancements, which continue to increase the speed and resolution of fMRI acquisitions. This dissertation explores a highly signal efficient fMRI imaging strategy known as Oscillating Steady-State Imaging (OSSI) and presents specialized artifact compensation strategies for addressing the practical challenges of the OSSI method.

First, we develop analytical models and simulations of OSSI, which describe how the signal magnitude varies as a function of frequency. These simulations are then used to study how respiration-induced frequency changes cause artifactual signal fluctuations to a signal timecourse. Our simulations show that the severity of respiration artifacts changes with initial off-resonance. Furthermore, we show that respiration artifacts are primarily caused by transient signal effects rather than changes to steady-state magnitude. These findings inform the two correction strategies proposed in the remainder of the dissertation.

The second portion of this work describes "OSSCOR," a retrospective method to correct timecourse magnitude changes caused by temporally varying frequency. We show how the OSSI signal exhibits a frequency-time duality which can be used to reshape structured physiological noise into a low-rank matrix. We then use principal

component analysis in a data-driven correction strategy to create nuisance regressors for subsequent fMRI analysis. We show that free induction decay (FID) signals can also be used to create nuisance regressors in the same way in a variation of our method, referred to as "F-OSSCOR." Both OSSCOR and F-OSSCOR were found to significantly improve the functional sensitivity and signal stability compared to polynomial detrending alone. OSSCOR was also found to significantly outperform a standard data-driven correction method, CompCor.

Finally, we present a prospective correction method which utilizes FID measurements to estimate and correct for B0 changes in real-time. Prospective correction has the potential to outperform retrospective correction methods by directly reducing perturbations to steady-state magnetization during acquisition. We first present the results of a feasibility analysis where simulation was used to determine how scan parameters would affect correction performance. We then developed a prospective correction application using a specialized scanner control platform to perform data analysis and parameter adjustment in real-time. Our initial fMRI proof-of-concept shows that real-time correction can increase the number of activated voxels and improve overall image stability as measured by tSNR.

CHAPTER I

Introduction

1.1 Motivation

Magnetic resonance imaging (MRI) is a medical imaging technique that offers unparalleled non-invasive imaging of soft tissue in the human body. While the first MRI methods were conceived in the 1960s, it was not until the early 1990s that MRI was first used to non-invasively image brain function, which would give rise to the exciting field of functional MRI (fMRI) [1][2][3]. Since then, many improvements have been made in how fMRI images are acquired, including fast acquisition trajectories [4][5], simultaneous acquisition of multiple slices [6], and parallel reconstruction methods [7][8][9]. State-of-the-art fMRI approaches are based on combinations of these strategies [10] to achieve rapid whole-brain imaging. Despite these advances in signal detection and reconstruction, most state-of-the-art fMRI methods still use the gradient-echo contrast mechanism initially proposed by Ogawa. An alternative class of fMRI techniques, steady-state sequences, has the potential to increase the theoretical limits of how fast fMRI data can be acquired by creating more signal than traditional SPGR sequences. This dissertation presents a new steady-state imaging approach called Oscillating steady-state Imaging (OSSI) as well as corresponding signal processing techniques for practical implementation in fMRI.

1.2 Outline and Contributions

The following dissertation is organized as follows. Background Chapter 2 reviews MRI, fMRI, and the problem of physiological noise in fMRI experiments. Chapters 3-5 discuss Oscillating Steady-State Imaging, Retrospective OSSI Physiological Correction Methods, and Prospective OSSI Physiological Correction Methods. Appendix A contains a how-to guide for performing fMRI experiments with the real-time B0 correction application developed in RTHawk. Each of these three body chapters introduces novel contributions to the field. Chapter 3 provides an analysis of how scan parameter selection affects the transient behavior of OSSI. Chapter 4 describes a retrospective method for reducing the effects of physiological noise in OSSI images. Concepts in Chapters 3 and 4 were presented at the 2018 Gordon Research Conference on in vivo MRI, as well as the 2019 ISMRM meeting, and has been submitted to *Magnetic Resonance in Medicine* pending review. Chapter 5 describes the use of prospective real-time control for OSSI and has been submitted as an abstract to the 2020 ISMRM meeting, pending review.

Appendix B contains details of an optimized angiography method for collateral vessel imaging, previously presented at the BMES 2016 Annual Meeting. This method has been in pre-clinical studies of arterial and venous disease, the results of which have been published in several articles [11][12][13][14][15].

CHAPTER II

Background

2.1 MRI Physics

This section describes selected concepts of MRI imaging and is neither complete nor rigorous. Instead, it is meant to provide the reader with a general understanding of some of the principles and terms used in MRI and provide context for the contributions described in this thesis.

2.1.1 Nuclear Magnetic Resonance

Atoms that have an odd number of protons possess a small magnetic moment due to having nuclear spin angular momentum. We refer to any such atom as a "spin," which can be thought of as a single small magnetically charged nucleus. Conveniently, the human body is abundant in such nuclei in the form of hydrogen atoms within water. While these spins naturally have no arrangement in the body and produce no net magnetic moment, spins will become generally aligned in the presence of an applied magnetic field, referred to as the B0 or "main" magnetic field. This is the fundamental physical premise of MRI, where a hydrogen-rich object (typically a person) is placed inside a large magnet, thus causing a net polarization of spins. This net polarization is described by the vector M_0, which describes the net strength of all summed spins in their equilibrium state within the field.

Since the net magnetization M_0 is in the same direction as the main magnetic field at equilibrium, it merely adds to the main field and cannot be detected. This direction of the M_0 vector at rest is referred to as the *longitudinal* or z-axis. In order to detect the magnetization, spins must be first rotated off the longitudinal axis into the perpendicular x-y plane, also called the transverse plane. The action of actively rotating spins is referred to as "excitation" and is accomplished by transmitting an RF pulse (B_1^+) at a particular frequency. For an effective excitation to occur, the radio wave must be at a specific frequency dictated by the Larmor equation:

$$\omega = \gamma B \qquad [2.1]$$

which describes the resonant frequency, ω, as a function of the applied field B and the gyromagnetic ratio γ for the nucleus in question. After spins are rotated into the transverse plane, they undergo *precession*, a wobbling rotation as they equilibrate to the longitudinal axis. Spins undergoing precession induce a current in specially designed receive coils which are placed nearby. This signal is referred to as free induction decay (FID) and is ultimately used to form MRI images.

The B0 field is ideally static and uniform throughout the tissue being imaged so that precession occurs at nominal frequency. However, this is hardly the case in practice as tissue interfaces and hardware imperfections result in a non-uniform B0 field inside the body. Field inhomogeneity can be measured using a technique called *field mapping*, which is used to measure and correct for field distortions. Figure 2.1 shows an example field map within the head, displaying distortions due to the tissue-air interface in the frontal sinus. Modern MRI systems attempt to reduce magnetic field inhomogeneity by using "shim" electromagnets to apply additional magnetic fields, improving field homogeneity [16]. Within the head at 3T field strength, field inhomogeneity can be reduced to about 200 Hz.

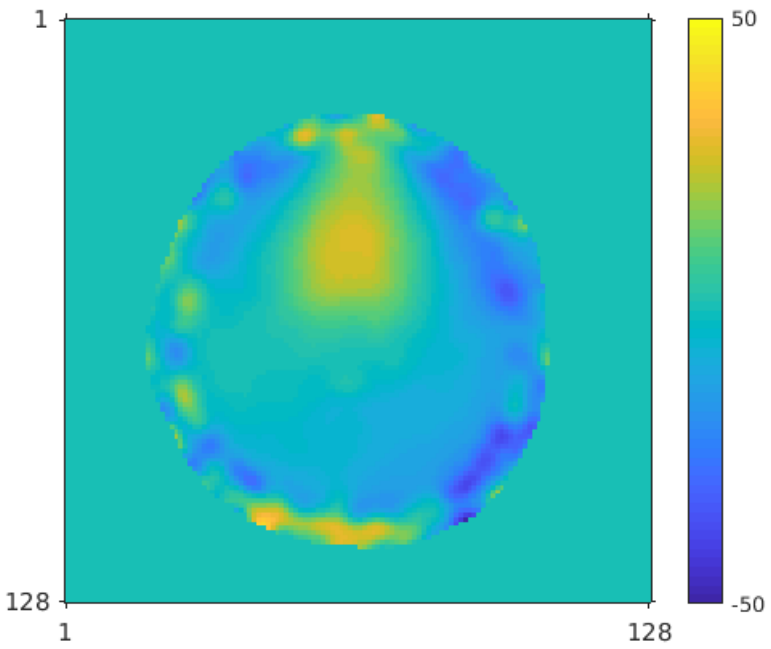

Figure 2.1: An axial field map of brain showing B0 distortion in Hz.

2.1.2 Relaxation

The signal produced by a spin undergoing free induction decay does not persist forever. Conveniently though, most excited spins within the body produce a signal for significantly measurable amounts of time, on the order of milliseconds to seconds. This decay phenomenon is referred to as "relaxation," a process that is governed by two time constants. The first is T1, which is the rate constant that describes the exponential recovery of a spin toward the longitudinal direction. The second is T2, which describes the exponential decay of the transverse signal. When considering intra-voxel field inhomogeneity, signals will decay faster with an "apparent T2," referred to as T2*. By manipulating the strength of excitation and time between excitations, tissues that have different T1 or T2 values will produce varying amounts of signal intensity, resulting in a tissue being bright or dark in an image. Such images are referred to as "T1-weighted" or "T2-weighted" since they only show relative differences in T1/T2 and not the actual quantitative values. Images with relative

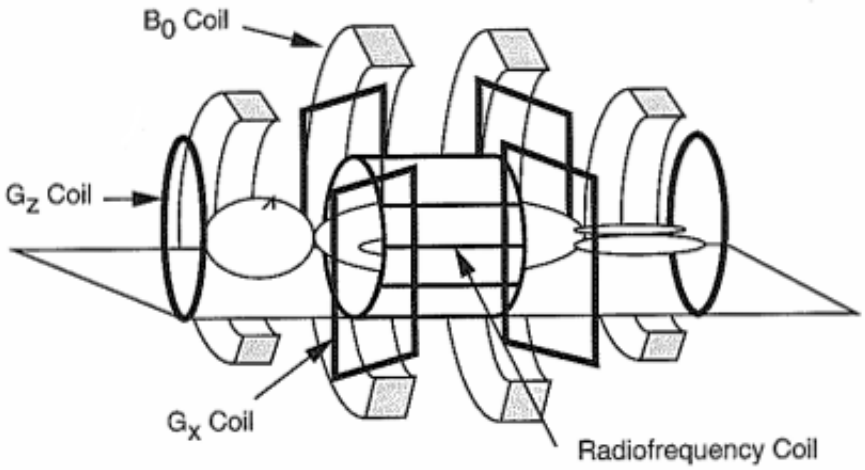

Figure 2.2: A diagram of MRI scanner components, depicting the main B0 coil, RF coil, and gradients.

weighting only take a fraction of the time to produce compared to quantitative maps and are therefore more clinically valuable as it is only necessary to visually detect tissue differences (ex. a hyper-intense lesion in the brain).

2.1.3 Spatial Localization

Signals from spins must be spatially localized in order to form an image. This is not possible by simply receiving the excited signal since the received signal is a sum of all the spins that were excited. Therefore if all spins are within the same B0 field, then they all rotate at the same frequency and cannot be differentiated. A second *spatially varying* magnetic field is applied to solve this problem. These fields are commonly linearly varying as a function of space, and induced by large electromagnets within the scanner bore. These electromagnets are referred to as "gradient coils" or simply "gradients." A simplified drawing showing the gradients, B0 magnetic, and RF can be seen in Figure 2.2[1].

With the application of a gradient field in the z-axis, G_z, the frequency of a spin

[1]Unpublished figure from Nishimura [17], used with written permission.

is determined as a function of its z-position:

$$\omega(z) = \gamma(B_0 + G_z(z)).$$

Applying a gradient allows spatially localized excitation to be performed. First, a constant gradient is applied, which results in a linear distribution of frequencies along the z-axis. Then, a designed RF wave is applied that only excites a desired range of frequencies. This process is referred to as slice selection. Here we consider a simple case where a thin slice with a desired thickness is excited in the x-y (axial) plane.

After slice selection in the z-axis, further spatial localization is needed to determine spin locations within the slice. This is done using the Gx and Gy gradients, which cause a distribution of frequencies in-plane to occur. By sampling the FID signal during an applied gradient, the Fourier transform can be used to determine the amount of energy at each frequency. Since frequencies now correspond to known spatial locations, a 2D image can be formed.

2.2 MRI Pulse Sequences

The previous description of excitation and spatial localization is an example of an MRI pulse sequence, which is a series of RF pulses and gradients arranged to accomplish a goal. In the goal of 2D imaging, a pulse sequence can simply consist of an RF pulse for excitation, followed by gradients of varying strengths to perform 2D imaging encoding. However, pulse sequences can create a variety of complex physical effects, resulting in images with different T1/T2/T2* contrasts, or encoding motion directly into the image data to measure blood velocity. The following are two of the simplest pulse sequences to perform 2D imaging and provide the basis for more complex sequences introduced in Chapter III.

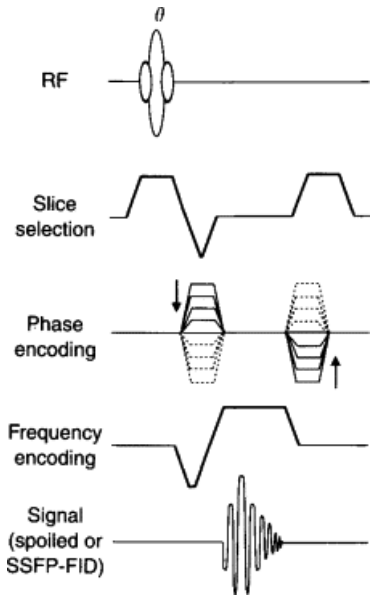

Figure 2.3: A GRE pulse sequence diagram.

2.2.1 Spoiled Gradient Echo

The gradient echo (GRE) sequence is one of the simplest pulse sequences to construct, consisting of an excitation followed by gradient readout. GRE sequences are generally used for their speed since each repetition time (TR) can be kept short, thereby reducing scan time. The GRE signal contrast is T2* weighted, and is widely used in fMRI. Since each TR can be played faster than T2 decay occurs, it is desirable to disrupt or "spoil" the transverse magnetization at the end of each TR. This is typically achieved using a combination of RF phase cycling and a spoiler gradient applied at the end of the TR to dephase any remaining magnetization. A diagram of a spoiled GRE sequence is shown in Figure 2.3, showing one repetition.

2.2.2 Balanced Steady-State Free Precession

Balanced steady-state free precession (bSSFP[2]) is a modification of the GRE sequence, where any phase accumulated by gradients is undone by the end of each TR.

[2]bSSFP is sometimes referred to as SSFP in literature. This is confusing and inconsistent in the field, since SSFP can also refer to non-balanced steady state sequences as well.

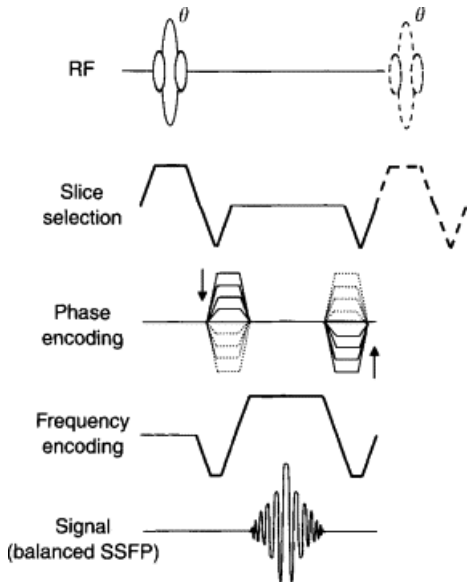

Figure 2.4: A bSSFP pulse sequence diagram.

An example bSSFP pulse sequence can be seen in Figure 2.4, where additional gradients are applied after signal detection such that the integrated gradient area is zero after a TR.

Because of balanced gradients, the dynamics of bSSFP are solely dictated by the excitation and any B0 off-resonance [18]. This leads to a unique signal behavior where both magnitude and phase are highly dependent on off-resonance. bSSFP sequences typically use fast TRs and large flip angles to create a signal contrast that is neither purely T1 or T2 dependent, but rather a unique T2/T1 ratio. Figure 2.5 shows an example bSSFP frequency response where the signal magnitude varies as a function of off-resonance. The dips in signal intensity are commonly referred to as the "transition band" regions and plateaus of high intensity as the "passband" regions. This frequency response profile results in images that have dark banding artifacts, where bands are regions of off-resonance corresponding to the transition band frequency region. An example of banding artifacts is shown in Figure 2.6, with an associated field map in Figure 2.1.

One of the simplest proposed solutions for banding artifact removal is to acquire

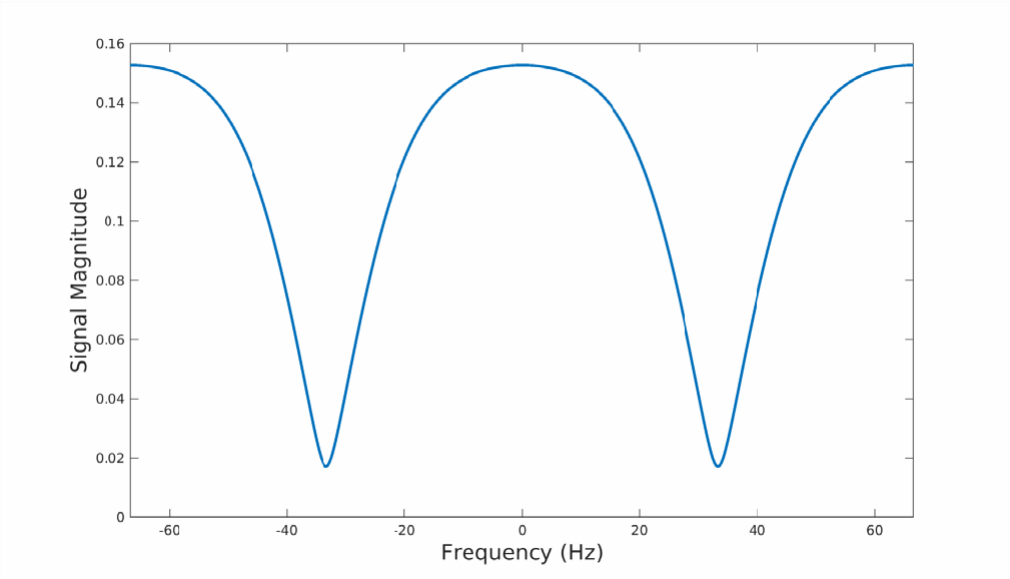

Figure 2.5: Frequency response for bSSFP with TR=15 ms, $\alpha = 40°$

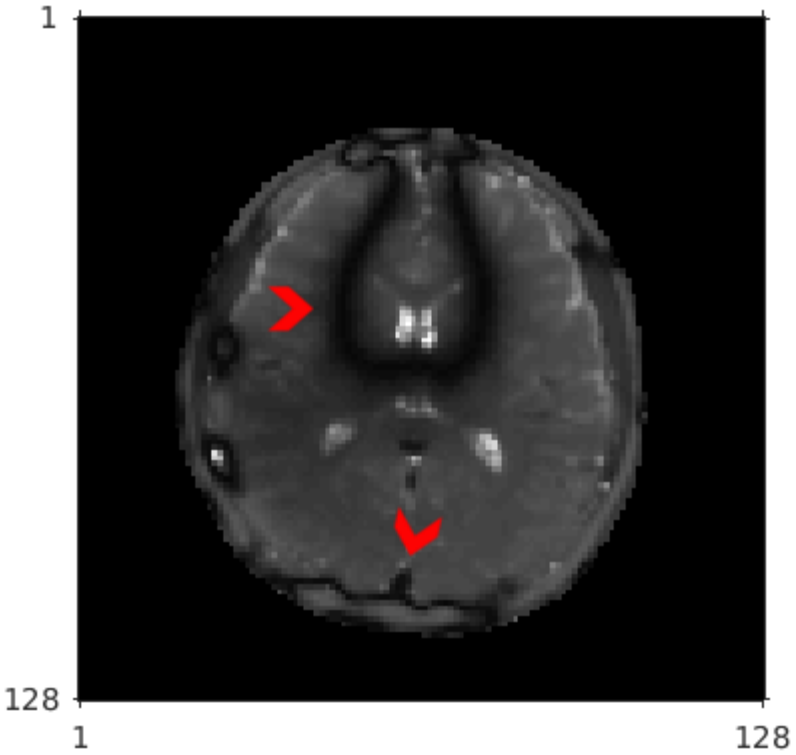

Figure 2.6: Simulated bSSFP image showing banding artifacts.

multiple images with different center frequencies, or equivalently, different RF phase increments [19]. Changing the center frequency would shift the frequency response, thus moving the bands around the image. The multiple images would then be combined into a single banding free image. The primary drawback of a phase-cycled approach is that multiple separate images need to be acquired and then combined, prolonging scan time. Multiple approaches have been proposed to improve the combination step and accelerate the phase cycled acquisition [20][21][22][23][24][25][26].

Despite having the highest SNR efficiency of any known pulse sequence [18], bSSFP is not commonly used used due to banding artifacts and atypical T2/T1 contrast. The primary clinical application is in cardiac imaging, where blood's high T2/T1 ratio results in bright signal and good contrast against myocardium [27].

2.3 Functional MRI

Functional MRI (fMRI) is an MRI technique used to detect neuronal activity in the brain. This is primarily performed using blood oxygenation level dependent (BOLD) contrast, where T2* weighted images are used to detect increases in blood oxygenation related to neuronal activity [1][28][29]. Since oxygenated hemoglobin is diamagnetic, but deoxygenated hemoglobin is paramagnetic, an increase in oxygenation leads to a small decrease in local magnetic field inhomogeneity. This decreased inhomogeneity creates slower T2* signal decay which results in an increase in signal intensity in a T2* weighted image. This increase in signal intensity is typically measured to be 2-5%. As a result of this small functional signal change, signal to noise ratio (SNR) becomes the primary limiting factor in reliably detecting BOLD signal changes.

2.4 fMRI Pulse Sequences

2.4.1 GRE

fMRI commonly employs GRE imaging as a means to acquire fast T2* weighted images. Following excitation, T2* weighting of the signal will monotonically increase with time as intravoxel dephasing occurs. However, this does not result in continuously increasing BOLD contrast, since signal decay results in a lower overall signal to detect. If the signal is sampled too early, no T2* weighting will be present. If the signal is sampled too late, then the signal will have decayed away, resulting in poor contrast to noise (CNR). Experimental data has shown that the ideal time after excitation to sample the signal (TE) is 30-40 ms for fMRI experiments performed at 3T [30].

2.4.2 Frequency Sensitive bSSFP

Using bSSFP is a solution for the low CNR in GRE-based fMRI, originally proposed by Scheffler et. al. [31]. In their seminal work, they noted that an increase in blood oxygenation causes a shift in mean frequency for intra-vascular spins on the order of 5 Hz. If these spins were in the bSSFP transition-band region, this frequency change would then directly cause a large change in signal magnitude of 9-10%, compared to the typical 2-5% in GRE. A drawback of the original method was that functional contrast only occurred in the part of the bSSFP frequency response with the lowest signal magnitude. This problem was later addressed by Miller et al. [32] in a variation of the method called "blood oxygenation sensitive steady state" or "BOSS" fMRI. By using a small flip angle, the bSSFP transition band profile could be inverted thus yielding functional sensitivity in areas of high signal strength. Furthermore, changes in intravascular frequency due to activation would result in a large change in phase, creating signal contrast through destructive signal cancellation of

individual spins. Both of these methods proposed a novel way of directly detecting the effects of blood oxygenation changes as opposed to the traditional GRE approach.

Despite the benefits to SNR and imaging speed, there are two challenges of transition band fMRI approaches that have limited their adoption. The first is that transition band fMRI approaches only have functional sensitivity within a narrow range of off-resonant frequencies, limiting detection of fMRI signals to only certain parts of the brain at a time. This was addressed by repeating the experiment with different frequency offsets, shifting the functional sensitivity to different parts of the brain each time [32]. These runs would then be combined into one activation map of the stimulus. This approach is not ideal, as the functional task would need to be repeated several times, slowing the acquisition and therefore reducing the SNR efficiency that the method aimed for in the first place. Second, the frequency-sensitivity exploited for functional sensitivity also resulted in these approaches being highly sensitive to any change to the B0 field, a common occurrence due to respiration, motion, or scanner hardware effects which are discussed below in Section 2.5. Such frequency changes result in shifts to the activation band regions and artifactual changes in signal magnitude, both deleterious to detecting functional signal changes.

2.5 Physiological Artifacts in BOLD fMRI

Artifactual signal changes make it even harder to detect the small functional signal changes in fMRI reliably. Artifacts can be caused by physiological processes such as cardiac pulsatility and respiration, as well as non-physiological sources such as scanner hardware instability [33][34][35]. Cardiac pulsatility results in fMRI artifacts due to changing pressure over the cardiac cycle, which induces pulsatile motion in blood vessels and surrounding tissue. Similarly, the motion of blood and CSF results in unwanted phase accumulation and an apparent change in M_0. These factors can cause additional artifacts in steady-state sequences like bSSFP, where signal artifacts

are caused by a disruption of the magnetic steady-state itself [36]. Respiration causes a similar disturbance, where chest wall motion results in susceptibility changes that vary the B0 field in the brain. The resulting field changes cause fluctuations in signal phase and amplitude, as well as errors in the spatial encoding process. In addition to respiration, scanner hardware instability results in temporally varying B0. This is primarily due to scanner heating, where heat from the gradients warms the passive shim elements which are close to the scanner bore and not perfectly insulated [37]. Since the magnetic properties of the shims are temperature dependent, a drift of the B0 field strength occurs.

Whole-head motion is another important confound in fMRI and corrupts images through similar physical processes. Motion corruption affects fMRI and structural MRI images alike, and research into motion correction is ongoing and extensive. In fMRI, different approaches are used to correct for whole-head motion vs. cardiac or respiratory motion, since the former permits the assumption of a rigid body whereas the latter does not. This body of work focuses on non-motion related correction methods but briefly discusses motion correction in Section 2.6.3 to provide context for the correction methods proposed in Chapter V.

2.6 Physiological Correction Methods

Numerous strategies have been proposed to "clean" artifacts from fMRI signals and can be categorized as retrospective or prospective approaches. Retrospective correction methods are applied after the data has been acquired, either as a previous or concurrent step with the functional task analysis. Retrospective methods will usually fall into one of two main strategies: model-based, which rely on external recordings of physiological states, and data-driven, which use signal processing methods to estimate physiological noise components. Prospective methods, on the other hand, are applied in real-time and reduce artifacts by physically correcting for how physiological pro-

cesses affect the spin-physics during imaging. There is no one best way of performing physiological correction, and every method has its strengths and weaknesses. The remainder of this section provides an overview of key methods in each category to provide background for the later chapters of this dissertation.

2.6.1 Model-based Methods

Model-based fMRI denoising methods are based on an understanding of how respiration and cardiac pulsatility affect the acquired signal. These methods begin with external recordings of the cardiac and respiratory cycle, typically measured by a photoplethysmography sensor (PPG) and pneumatic belt placed on the subject. These recordings are then used to calculate the cardiac and respiratory phases for input into a model of physiological noise. Two quintessential models are RETROKCOR [38] and RETROICOR [39], which model physiological noise as a Fourier expansion of the cardiac and respiratory phases. In the former approach, these Fourier terms are used to regress out suspected physiological noise in the central parts of k-space corresponding to low spatial frequencies. In the latter method, the Fourier terms are used directly on each voxel's timecourse as part of the general linear model. Both methods work well and use a simple but effective assumption of how externally recorded cardiac and respiratory phases manifest as artifacts in an fMRI time series.

2.6.2 Data-driven Methods

Data-driven methods forgo external physiological recordings and perform physiological denoising just with the data itself. These methods go beyond basic signal processing techniques such as filtering frequencies since the temporal resolution of most fMRI acquisitions does not reach the Nyquist rate required to prevent aliasing. For example, the widely used Human Connectome Project (HCP) protocol uses a TR of 720 ms [40], resulting in a Nyquist frequency of 0.69 Hz. While this is fast enough

to prevent aliasing of respiration (0.3-0.4 Hz), cardiac noise will still alias (approx 1 Hz). Instead, data-driven methods focus on using data decomposition techniques such as PCA or ICA in combination with a spatio-temporal prior.

A popular example of this is CompCor [41], which performs PCA on voxel time courses within a selected ROI. The ROI contains voxels that ideally contain physiological noise but no functional signal changes. The ROI is either defined manually by selecting white matter (WM) or cerebral spinal fluid (CSF) voxels, or by selecting voxels that have a high temporal standard deviation (tSTD) and low correlation with the task waveform.

There are many other data-driven methods that use similar principles, such as spatial ICA [42], masked ICA [43], CORSICA [44], and PHYCCA [45][46]. These are all different approaches of solving the same problem in data-driven physio correction: determining which signal components are due to an unwanted physiological change and which are due to a desirable functional change.

2.6.3 Prospective Methods

While model-based and data-driven methods are applied retrospectively after data has already been acquired, prospective correction is used in real-time during data acquisition to actively reduce physiological noise. Such approaches require specialized equipment and software to adjust scan parameters during acquisition and can require additional calibration steps. Most prospective methods have focused on reducing the effects of motion by tracking the head position and updating the scan volume to maintain a constant frame of reference. Popular approaches use image or navigator data to create motion estimates or utilize external optical tracking [47][48][49][50][51]. The end goal is to eliminate the effects of motion during acquisition, rather than retrospectively "cleaning up the damage." Motion correction is similar to denoising of cardiac and respiratory signals in fMRI in that both cause unwanted signal changes,

though the underlying mechanics and approaches of motion correction differ significantly and are beyond the scope of this work. However, we call attention to motion correction since it is currently the dominant use of prospective correction in fMRI.

A less common use of prospective correction is real-time B0 compensation, which seeks to compensate for any changes to the B0 field through time. As mentioned in Section 2.1.1, both respiration and scanner heating effects result in changes to the B0 field. Changes to the B0 field result in signal fluctuations in fMRI timecourses [33], and can also worsen image quality [52]. These changes to the B0 field can be prospectively corrected in real-time through adjustments to the RF phase or shims. While retrospective B0 estimation is a highly effective and popular approach for correcting image distortion [53][54], there has been limited investigation and use of prospective B0 correction in fMRI or MRI as a whole.

At first, it seems surprising that while "field-locking" was developed for NMR in the 1970's [55] to correct for B0 instability, only a handful of studies have demonstrated implementations of an equivalent system for MRI [56][57][58][59][60]. There are a few apparent reasons for the lack of technological development and the adoption of this technique. First, MRI hardware vendors implement rudimentary correction methods that perform frequency adjustment based on *anticipated* B0 changes from the gradient waveforms, with remaining artifacts corrected retrospectively. Second, research on real-time B0 correction methods is hindered by the fact that modern MRI systems are not designed for real-time control, and there is limited vendor support for developing such technically complex projects. Lastly, modern fMRI sequences use a spoiled signal mechanism that is only moderately sensitive to B0 changes. The resulting changes to signal magnitude can be corrected retrospectively using polynomial detrending, but this method is sub-optimal in that it does not account for the phase changes in image reconstruction or underlying changes to the magnetization.

CHAPTER III

Analysis of Oscillating Steady-State Signals

3.1 Introduction

Oscillating Steady-State Imaging (OSSI) is a sequence that combines balanced gradients with a quadratic RF phase increment to produce a large, periodically oscillating signal. This signal has been shown to have T2* weighting that is similar to GRE [61] but uses a contrast mechanism that is similar to previous balanced steady-state (transition-band) fMRI approaches, where a small change in frequency can cause large changes in signal phase or magnitude, resulting in T2* weighting [31][32]. However, OSSI departs from previous bSSFP based fMRI methods by combining the signals from an oscillating period into one signal. This combined signal exhibits T2* sensitivity across its entire frequency response, thereby enabling whole-brain coverage without the need for separate phase-cycled runs.

There are two distinct advantages of OSSI-based fMRI compared to a conventional GRE sequence. The first is that OSSI is highly SNR efficient, where SNR efficiency is defined as the SNR divided by the square root of the imaging time. This is because OSSI produces a signal that is much larger than a conventional spoiled GRE sequence OSSI. Furthermore, the OSSI sequence uses a short TR that results in acquisition duty cycles upward of 80%. The second advantage is that OSSI exhibits T2* sensitivity immediately after excitation and does not require long echo times for BOLD contrast

to form, similar to transition-band fMRI. This enables the use of much faster TRs and shorter echo times, thereby increasing the acquisition duty cycle and further boosting efficiency [62].

OSSI has the potential of exceeding the SNR efficiency limits of conventional spoiled GRE acquisitions, thereby enabling higher acceleration factors and improved spatial resolution. Higher SNR is needed to improve the spatial resolution of fMRI without introducing noise, since SNR is proportional to voxel volume [63]. High-resolution mapping of brain activity is widely considered one of the next frontiers of fMRI and may lead to an improved understanding of the intricate architecture of subcortical brain structures [64][65][66][67].

Steady-state fMRI approaches like OSSI achieve high SNR efficiency by maintaining transverse magnetization, never allowing T2 relaxation to fully occur. As a result, the signal following an excitation is dependent on the signal state from the conclusion of the previous TR. This presents a problem for fMRI since univariate fMRI analysis assumes that every voxel in every time frame is spatially and temporally independent. This assumption is violated in a steady-state sequence, where the signal at any timepoint is affected by the "spin-history" of several TRs before it. As a result, any perturbation to the steady-state magnetization will result in serially correlated signal fluctuations. Correlated signal structures result in biased test statistics if left uncorrected, ultimately undermining the inferences drawn from an fMRI experiment [68][69].

Model-based correction is a common strategy to minimize the effects of temporally correlated noise due to physiological changes or scanner drift [70]. These methods work by modeling the relationship between a latent physiological parameter and a change in signal, for example, modeling the relationship between respiratory phase and signal amplitude. The latent physiological parameters are then either fit from the data or estimated from external measurements such as a pneumatic respiration belt

or photoplethysmogram. The success of these models is ultimately dependent on the quality of the model and the ability to accurately estimate latent signal parameters.

This chapter develops signal models and analyzes the behavior of the OSSI signal in order to determine the viability of model-based correction. First, we present a discrete-time model of OSSI that describes the frequency-dependent nature of the signal under steady-state conditions. Next, we present the results of impulse response simulations that characterize how transient behavior varies as a function of frequency and OSSI cycle length. Finally, we show how the rate of frequency shift is an important factor in modeling the OSSI signal, and how transient fluctuations can create constructive or destructive interference in the combined OSSI signal magnitude.

3.2 Theory

3.2.1 Steady-States as a Discrete-Time System

The magnetization in a steady-state sequence can be described by the following discrete-time relationship [71]:

$$\mathbf{M}_{k+1} = \mathbf{A}\mathbf{M}_k + \mathbf{B} \qquad [3.1]$$

where $\mathbf{M}_k$ is a 3×1 vector representing the magnetization during the kth TR, $\mathbf{A}$ is a 3x3 matrix, and $\mathbf{B}$ is a 3x1 vector. Both $\mathbf{A}$ and $\mathbf{B}$ are functions of scan parameters (TR, TE, RF flip angle and phase) and tissue parameters (T1, T2, $\Delta\omega$). This steady-state model considers the case where no gradients are applied (or gradients are balanced). This model also assumes that RF excitation is instantaneous. Note that this model only considers a single isochromat, and does not model T2* effects which arise from a distribution of isochromats resulting from microscopic field distortions.

The steady-state solution of this system is then defined as:

$$\mathbf{M}_{k+1} = \mathbf{M}_k = \mathbf{M}_{ss} = (\mathbf{I} - \mathbf{A})^{-1}\mathbf{B} \quad [3.2]$$

where each successive excitation results in the steady-state magnetization $\mathbf{M}_{ss}$. Any initial condition $\mathbf{M}_0$ will eventually converge to its steady-state value $\mathbf{M}_{ss}$. The transient response of this system is then defined as the sequence of residuals between an intermediate state and the steady-state:

$$\mathbf{Q}_k = \mathbf{M}_k - \mathbf{M}_{ss} \quad [3.3]$$

where $\mathbf{Q}_k$ is the transient component of the magnetization for the kth TR.

An ideal steady-state signal is temporally stable, such that $\mathbf{M}_{ss}$ is constant and $\mathbf{Q}_k = 0$. This is not the case in practice because the target steady-state vector $\mathbf{M}_{ss}$ is a function of $\Delta\omega$ which can be affected by respiration or scanner field drift. When $\Delta\omega$ varies slowly compared to the TR and tissue relaxation rates, the magnetization can be considered quasi-static where $\mathbf{M}_{ss}$ varies through time but $\mathbf{Q}_k \approx 0$. Conversely, rapid changes to $\Delta\omega$ changes violate the quasi-static assumption and result in a transient signal component as the magnetization evolves to the new value of $\mathbf{M}_{ss}$.

Equation 3.2 describes how a single repeated excitation results in a steady-state magnetization; however, steady-states sequences are not limited to just a single excitation. For example, a sequence with three different RF pulses could be represented by:

$$\mathbf{M}_{k+1} = \mathbf{A}_1\mathbf{M}_k + \mathbf{B}_1$$

$$\mathbf{M}_{k+2} = \mathbf{A}_2\mathbf{M}_{k+1} + \mathbf{B}_2$$

$$\mathbf{M}_{k+3} = \mathbf{A}_3\mathbf{M}_{k+2} + \mathbf{B}_3$$

containing 3 different RF pulses which may have different phases or flip angles. This sequence will create a steady-state that cycles through three different temporal phases:

$$\mathbf{M}_{ss,1} = \mathbf{A}_1\mathbf{M}_{ss,3} + \mathbf{B}_1$$
$$\mathbf{M}_{ss,2} = \mathbf{A}_2\mathbf{M}_{ss,1} + \mathbf{B}_2$$
$$\mathbf{M}_{ss,3} = \mathbf{A}_3\mathbf{M}_{ss,2} + \mathbf{B}_3$$

or written as a single equation[1]:

$$\begin{bmatrix} \mathbf{M}_{ss,1} \\ \mathbf{M}_{ss,2} \\ \mathbf{M}_{ss,3} \end{bmatrix} = \begin{bmatrix} \mathbf{A}_1 & 0 & 0 \\ 0 & \mathbf{A}_2 & 0 \\ 0 & 0 & \mathbf{A}_3 \end{bmatrix} \begin{bmatrix} \mathbf{M}_{ss,3} \\ \mathbf{M}_{ss,1} \\ \mathbf{M}_{ss,2} \end{bmatrix} + \begin{bmatrix} \mathbf{B}_1 \\ \mathbf{B}_2 \\ \mathbf{B}_3 \end{bmatrix}$$

We can generalize this expression to any n number of excitations:

$$\begin{bmatrix} \mathbf{M}_{ss,1} \\ \vdots \\ \mathbf{M}_{ss,n-1} \\ \mathbf{M}_{ss,n} \end{bmatrix} = \begin{bmatrix} \mathbf{A}_1 & 0 & \dots & 0 \\ 0 & \ddots & 0 & \vdots \\ \vdots & 0 & \mathbf{A}_{n-1} & 0 \\ 0 & \dots & 0 & \mathbf{A}_n \end{bmatrix} \begin{bmatrix} \mathbf{M}_{ss,n} \\ \mathbf{M}_{ss,1} \\ \vdots \\ \mathbf{M}_{ss,n-1} \end{bmatrix} + \begin{bmatrix} \mathbf{B}_1 \\ \vdots \\ \mathbf{B}_{n-1} \\ \mathbf{B}_n \end{bmatrix} \quad [3.4]$$

where the value for all n steady-states can be solved for using Equation 3.2.

3.2.2 Quadratic Phase Cycling

Steady-state pulse sequence design is a fascinating problem because even the simplest sequences can have incredibly complex behavior. This is the case with quadratic phase cycling, where only varying the RF phase can create useful steady-state behavior. The idea of using a quadratic phase was introduced by Zur et al. [72] as a

[1]Credit to Tianrui Luo for this insight

way to perform spoiling of transverse magnetization. Their work described a steady-state sequence where RF phase was incremented after each TR using the following recurrence equation:

$$\phi(n) - \phi(n-1) = \psi_A n + \psi_B \quad [3.5]$$

where ψ_A and ψ_B are arbitrary constants, ϕ is the RF phase in radians, and n is the TR number. The solution to this equation is:

$$\phi(n) = \frac{1}{2}\psi_A(n+1)n + \psi_B n + \phi(0) \quad [3.6]$$

where $\phi(0)$ is an arbitrary initial phase. Since the linear and constant terms shift the frequency response, this expression can be simplified to:

$$\phi(n) = \frac{1}{2}\psi_A n^2 \quad [3.7]$$

This equation produces periodic phase sequences with the following relationship:

$$\psi_A = \frac{2\pi}{n_c} \quad [3.8]$$

When n_c is integer-valued, the sequence of phase increments produced by Equation 3.5 is periodic every n_c TRs. Furthermore, the sequence of phases from Equation 3.7 is periodic over n_c TRs when n_c is even, or periodic over $2n_c$ TRs when n_c is odd.

bSSFP sequences that implement a quadratic phase sequence can intuitively be thought of as a sequence that is continuously and linearly increasing its center frequency. When this center frequency increase is small, the frequency response of the sequence will slowly shift during the scan. If the quadratic sequence was periodic over $n_c = 200$ TRs, then the frequency response will cyclically shift by 1/200th of the width of the frequency response every TR, which after the 200th TR the frequency

response would have returned to the same position as the first TR. This is also explained by Equation 3.4, where 200 different RF phases result in 200 steady-state values.

Continuously varying the RF phase is useful as an alternative solution for bSSFP banding problem, rather than acquiring multiple discretely phase-cycled images. It was proposed by Foxall [73] that continuous RF phase modulation could be performed using a quadratic phase increment, where a small linear phase increment ($2 - 4^\circ$ per TR) would continuously shift the frequency response. By dynamically increasing the RF phase increment, the need to re-establish the steady-state after each frequency shift could be eliminated. Additional variations of this dynamic phase cycling concept have been proposed [74][75][76][77][78][79].

3.2.3 Oscillating Steady-State Imaging

Foxall proposed that a small phase increment (effectively $n_c \geq 120$) is needed to prevent severe distortions to the frequency response and to maintain a steady-state condition. The following work establishes that this is only partially true. While decreasing the period of a quadratic sequence does lead to severe distortion of the frequency response, a new type of steady-state emerges with useful signal properties like T2* weighting. We refer to this new type of steady-state as Oscillating Steady-State Imaging, or OSSI for short. The OSSI signal is periodic over n_c TRs, with a different magnetization state for each TR. We refer to each magnetization state as a *phase*, such that there are n_c different phases per OSSI cycle. Each phase is then sampled to form n_c separate images with different banding artifacts. Each of the n_c images is then used to form one artifact-free image, an approach commonly used in frequency cycled bSSFP imaging [19][80][81][74][25][82]. In OSSI, we propose a simple voxel-wise combination strategy of taking the 2-norm of each of the n_c images to form one real-valued image, similar to previous phase-cycled bSSFP image combination

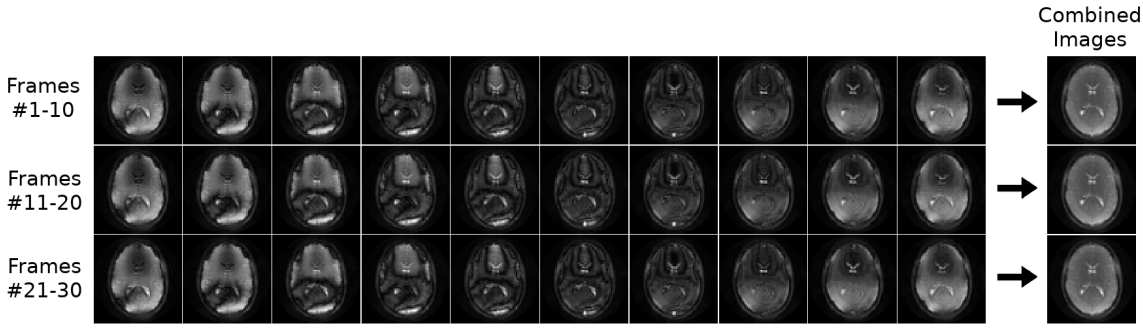

Figure 3.1: Single slice images of the OSSI steady-state, with period $n_c = 10$. Three sets of 10 timepoints are shown to demonstrate reproducibility. Each set of 10 images is then combined into one image with uniform contrast.

methods. An example showing OSSI images and resulting 2-norm combined images is shown in Figure 3.1.

3.2.4 Modeling the OSSI Frequency Response

An OSSI sequence contains n_c different excitation phases, resulting in a signal evolution with n_c different frequency responses as given by Eq. 3.4. Here we present a framework to represent these multiple frequency responses, which is later used to analyze the behavior of combined images. This framework is also used in Chapters IV and V for retrospective and prospective correction of physiological artifacts.

First, consider a bSSFP sequence with a linear phase progression such as a $0° - 0°$ or $0° - 180°$ phase pattern. This can be thought of as a trivial quadratic phase progression with a period of $n_c = 1$. The magnitude-frequency response can then be written as $h\colon \mathbb{R} \to \mathbb{R}_+$, defined by the function $h(f) = s$ which maps the off-resonance frequency f to a single positive signal magnitude s. The shape of the frequency response function, h, also depends greatly on scan parameters such as the TR, TE, and flip angle. Note that h is a periodic function, defined by:

$$h(f + f_s) = h(f), \qquad [3.9]$$

where $f_s = \mathrm{TR}^{-1}$, the signal sampling frequency. Since a linear phase progression results in a single steady-state response, h is a single-valued function for a given off-resonance frequency, f, and set of sequence parameters.

We then expand this definition to OSSI sequences where $n_c > 1$. Let $\mathcal{H} : \mathbb{R} \to \mathbb{R}_+^{n_c}$ defined by $\mathcal{H}(f) = v$ be the OSSI frequency response, which maps f to a vector v of n_c signal magnitudes which comprise a full period. Since a quadratic phase progression is equivalent to incrementing the center frequency by a constant amount, the OSSI frequency response can be described by a series of shifted frequency responses:

$$\mathcal{H}(f) = v = \begin{bmatrix} h(f) \\ h(f + f_s/n_c) \\ h(f + 2f_s/n_c) \\ \vdots \\ h(f + (n_c - 1)f_s/n_c) \end{bmatrix} \qquad [3.10]$$

An example of the first two frequency responses for $n_c = 6$ is shown in Figure 3.3a. Intuitively, Equation 3.10 describes how an off-resonance f maps to n_c copies of the same frequency response function, with each successive copy shifted by f_s/n_c Hz. An increase in off-resonance by Δf then results in a shift in all n_c frequency response curves by the same amount. This leads to an interesting property: a frequency shift of f by $\Delta f = f_s/n_c$ Hz results in a circular shift of the elements in the signal vector v by one position. Additionally, a frequency shift of $\Delta f = f_s$ would cause a circular shift of n_c positions, which results in no effect since v is of length n_c. Since an acquired timecourse m is a repeating sequence of the n_c elements of v, a frequency shift of $\Delta f = f_s/n_c$ results in an apparent temporal shift of m by 1 TR. Similarly, a shift of $\Delta f = f_s$ would result in a temporal shift of n_c TRs, resulting in no effect since the timecourse is periodic every n_c TRs.

This temporal shift property can be exploited to produce a more uniform fre-

quency response by taking the vector norm of v to produce a single "combined" signal value. We define the combined signal response as $\mathcal{G}(f) = \|\mathcal{H}(f)\|_2$, the 2-norm of the frequency response signals vector v.

For fMRI, the 2-norm combination of every n_c temporal frames creates one combined image, resulting in an effective TR defined by:

$$\mathrm{TR}_{\mathrm{eff}} = n_c \mathrm{TR} \tag{3.11}$$

Selecting smaller values for n_c lowers the effective TR, but increases the variation of the combined frequency response. Conversely, larger n_c values create a "flatter" combined frequency response which is more desirable, but at the cost of a longer $\mathrm{TR}_{\mathrm{eff}}$. Furthermore, flip angle and T2 interact with frequency sensitivity and SNR efficiency, making scan parameter selection non-trivial.

3.2.5 Effects of Temporally Varying Frequency on OSSI

The frequency response analysis presented in Section 3.2.4 assumes a steady-state condition where the B0 field is stable, unchanging through time. A steady-state assumption is useful for modeling basic signal characteristics, but does not consider temporally varying B0 changes due to respiration and scanner drift. Such changes to the B0 field results in transient signal behavior [71], which can be written as:

$$\mathbf{Q}_k = \mathbf{M}_k - \mathbf{M}_{ss} \tag{3.12}$$

where $\mathbf{Q}_k$ is the deviation from the steady-state for the kth excitation.

Though Foxall noted that bSSFP sequences with small phase increments were relatively robust to transient behavior [73], preliminary experiments have shown that temporally varying frequency can cause unwanted fluctuations in the OSSI signal evolution. This chapter presents our investigation on how OSSI parameter selection

affects the combined frequency response during transient and steady-state conditions, with the ultimate goal of minimizing the impact of frequency changes in OSSI fMRI.

3.3 Methods

The following experiments used a custom OSSI Bloch simulation based on Hao Sun's general Bloch simulator, which is freely available as part of the Michigan Image Reconstruction Toolbox [83]. Scan parameters were kept constant at TR=15ms, TE=2ms, and FA=10° based on prior optimizations for T2* sensitivity. Tissue parameters were kept fixed for all simulations at literature values for gray matter at 3T: T1=1331 ms and T2=80 ms [84]. Simulation was used to study how n_c affects the amount of "ripple" in the combined frequency response profile at steady-state, as measured by the average absolute percent signal change from the profile mean. Note that this simulation is of the combined frequency response where frequency does not change through time (i.e., no drift or respiration).

The effects of time-varying frequency were analyzed using simulations of a step response and of respiration. A step of 1 Hz was simulated for n_c values ranging from 2 to 16. Next, respiration and drift were simulated over a 30 second period for the same n_c values, shown in Figure 3.2. Respiration frequency changes were scaled to a 2 Hz peak-to-peak magnitude, based on literature reported and in-house experimental values. Perlin noise (mean = 0 Hz, P-P amplitude = 1 Hz) was added to increase variability and more accurately mimic the inconsistencies in actual human respiration patterns. An additional drift term was added of 1 Hz/min. Note that a 2 Hz change due to respiration is fairly large and usually only observed in lower slices.

Performance was measured by integrating the absolute value of the transient signal component for each timecourse, as defined by Eq. 3.12.

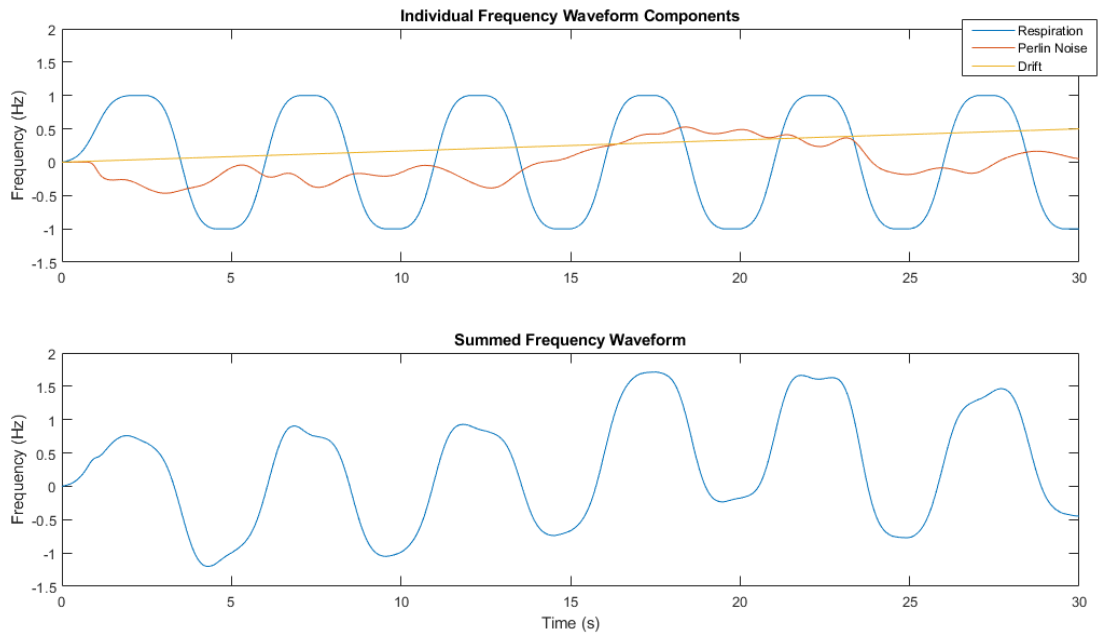

Figure 3.2: Time-varying frequency used for OSSI Bloch simulations of respiration and drift, showing individual and summed timecourses.

3.4 Results

3.4.1 Static Frequency Response Simulations

Figure 3.3 shows examples of the individual and combined frequency responses for $n_c = 6$. The combined frequency response shows a maximum peak to peak variation of 17% from its mean, compared to the uncombined response, which varies 127%. Figure 3.4 shows the combined frequency response variation, showing how profile uniformity and inter-band spacing increases with n_c. A summary of combined profile variation vs n_c is shown in Figure 3.5, illustrating how higher n_c values improve the mean uniformity of the combined frequency response.

3.4.2 Step Response Simulations

Figure 3.6 shows the 1 Hz step response behavior of $n_c = 10$, simulated for initial off-resonance values of 0 and 3 Hz. The amplitude and duration of the transient re-

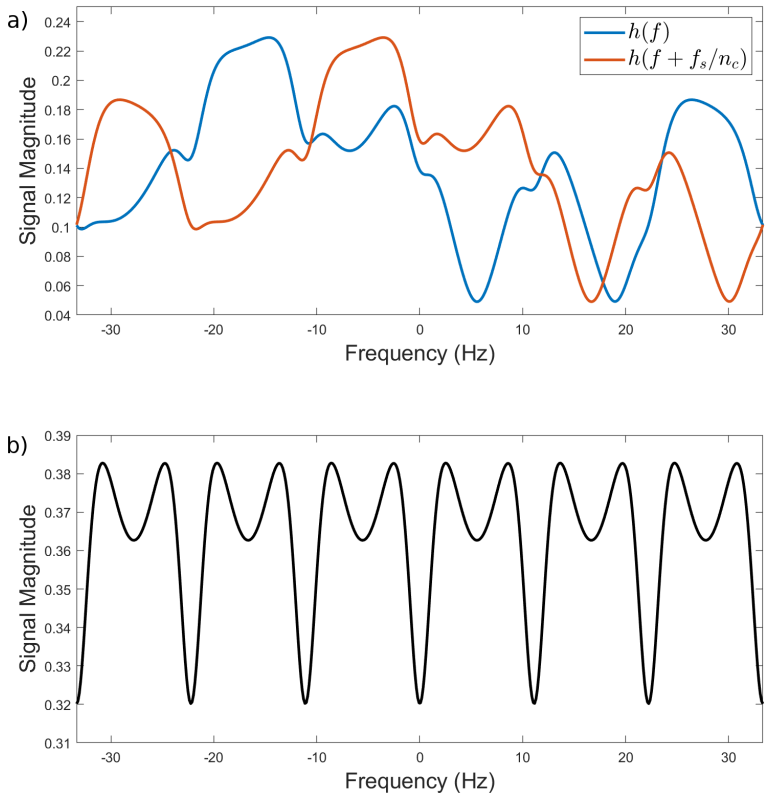

Figure 3.3: Simulated OSSI frequency responses (a) for $n_c = 6, \text{TR} = 15$ ms, and FA $= 10°$. The frequency responses for the first 2 of 6 phases in the cycle are plotted, and are identical except for a $f_s/n_c = 11.1$ Hz shift. The corresponding combined frequency response (b) shows a bSSFP-like profile that is periodic over f_s/n_c Hz. Note differing scales.

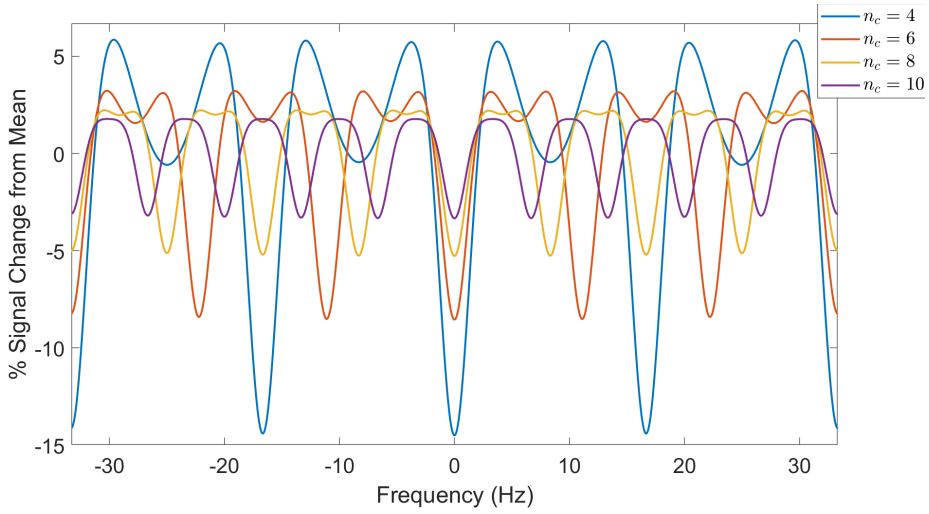

Figure 3.4: Example combined frequency response variation for selected values of n_c. Variation was calculated as percent change from the profile mean.

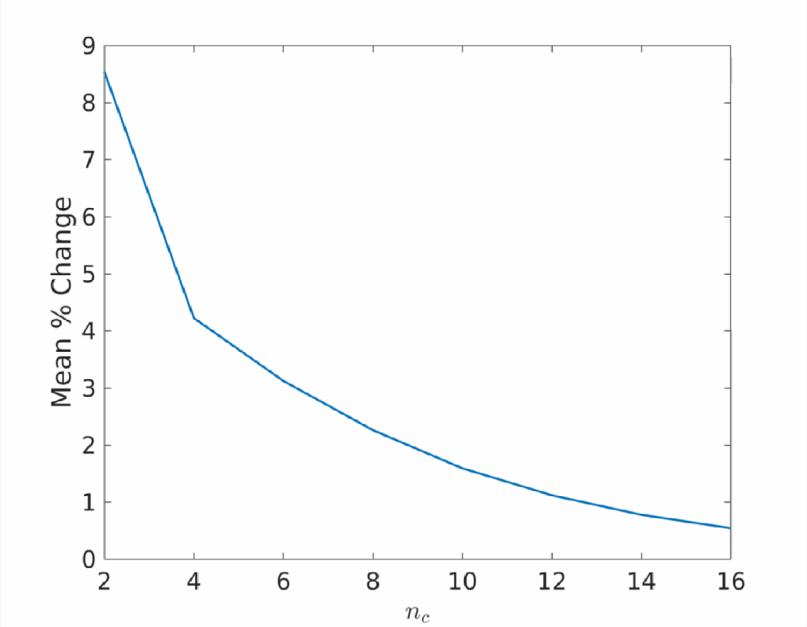

Figure 3.5: Mean absolute percent change for combined frequency responses, calculated for even n_c values from 2 to 16. Increasing n_c improved the uniformity of the steady-state combined frequency response.

sponse strongly vary as a function of off-resonance. The integrated transient response as a function of off-resonance is shown in Figure 3.7 for selected n_c values of 6, 10, and 14. The mean severity of transient effects was found to decrease as n_c increased. The response was found to repeat periodically as a function of frequency over a period of $(n_c \cdot \mathrm{TR})^{-1}$ Hz.

3.4.3 Respiration Simulations

Figure 3.8 shows the simulated effects of respiration for a single combined timecourse initialized at 0 Hz. The continuous timecourse simulates each TR using the magnetization from the previous TR, thereby maintaining spin history and accurately accounting for transient behavior. The quasi-static timecourse simulates each TR independently to steady-state, only showing changes due to variation of the combined frequency-response profile. The average percent signal change from the timecourse mean was 0.91% for the quasi-static simulation and 2.64% for the continuous simu-

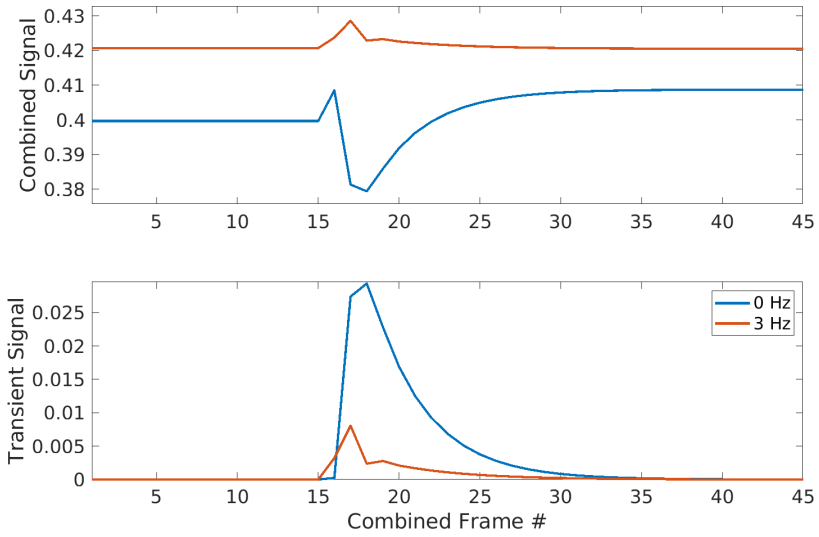

Figure 3.6: Combined signal step response and transient signal component for simulated isochromats at 0 and 3 Hz.

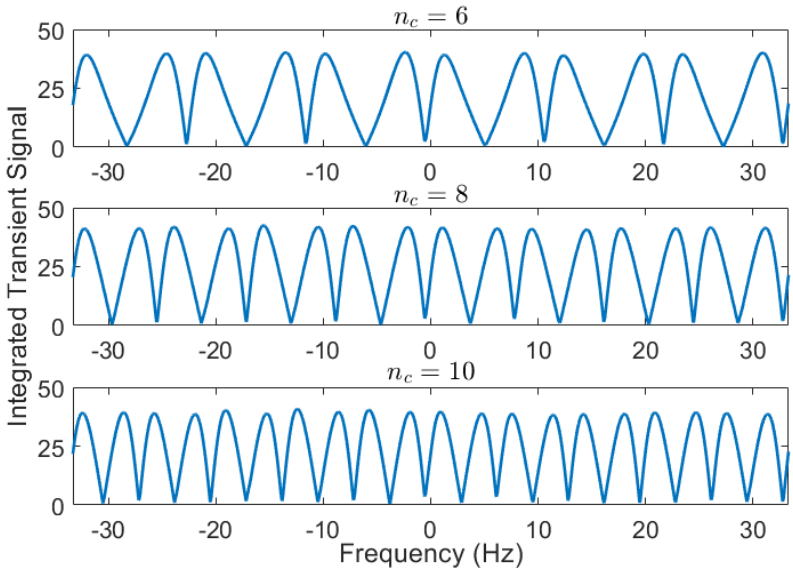

Figure 3.7: Integrated transient response vs. off-resonance for $n_c = 6$, 8, and 10. Integration was calculated as the sum of the transient response multiplied by the TR_{eff} for normalization.

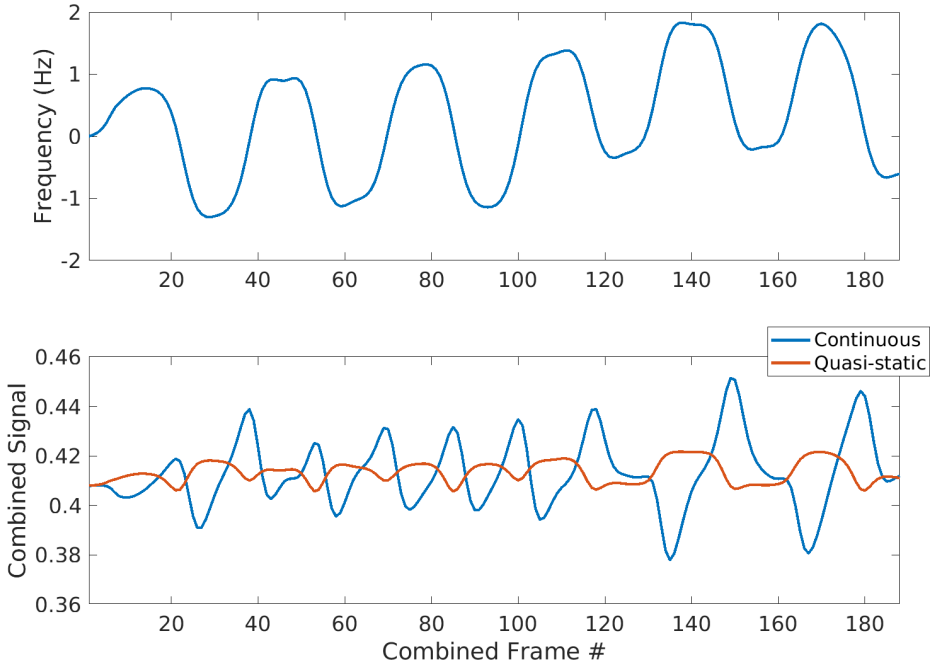

Figure 3.8: Simulated OSS timecourse with respiration effects for $n_c = 10$. The continuous simulation maintains spin-history and shows transient behavior, while the quasi-static case plots the steady-state signal value independently for each TR.

lation.

The simulation in Figure 3.8 was then repeated for a range of initial off-resonance values to visualize how transient effects distort the individual and combined frequency responses through time. Figure 3.9a shows the simulated respiration waveform initialized at 0 Hz, with two time points of interest marked in blue and orange, representing minimum and maximum respiratory phase. The corresponding individual frequency responses for these two timepoints are shown in Figure 3.9b, with the steady-state frequency response plotted in black for reference. The transient effects caused by respiration are shown to introduce small sinusoidal distortions to the frequency responses.

The corresponding combined frequency response for the blue and orange timepoints are shown in Figure 3.9c, showing large sinusoidal distortions. These distortions are caused by the smaller distortions in Fig 3.9b which then constructively or

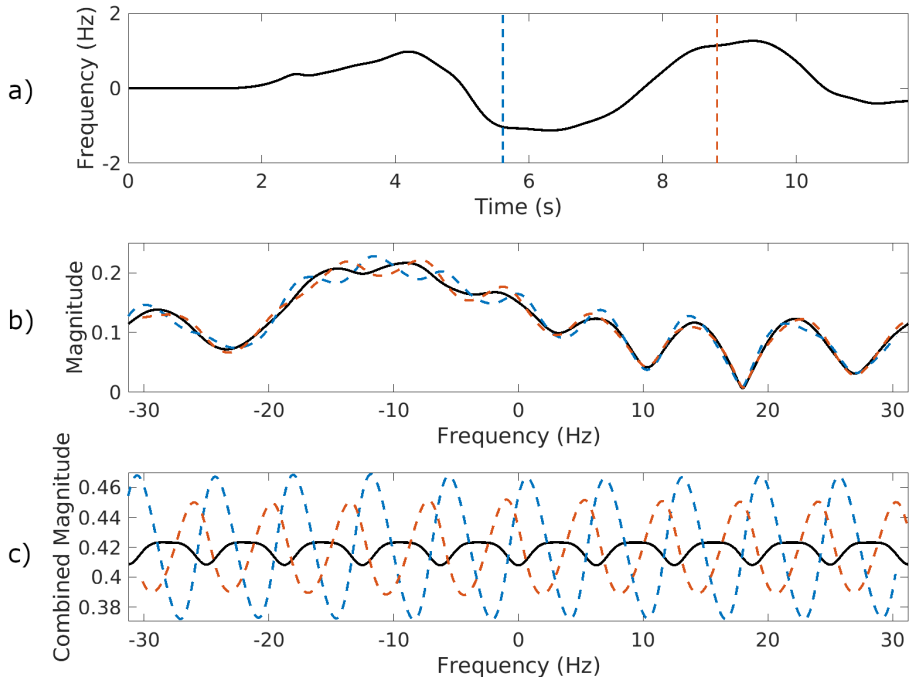

Figure 3.9: Effect of respiration on the frequency response for $n_c = 10$. Plot a) shows the simulated frequency timecourse with two time points of interest marked in blue and orange. Plots b) and c) show the individual and combined frequency responses for steady-state (black), with the respiration-distorted frequency responses superimposed.

destructively interfere during the 2-norm combination step. Note that the units in Fig 3.9c can be directly compared to the combined timecourse in Fig. 3.8.

3.5 Discussion

The OSSI signal combination approach is similar to phase-cycled bSSFP imaging, where multiple images are acquired with a range of constant RF phase increments, then combined to form a single image with smooth contrast. Since constant frequency increments only shift the frequency response, the number of phase cycles in traditional bSSFP imaging can be chosen independently of the frequency response profile. This is not the case in OSSI, where reducing the cycle parameter n_c was found to increase the variation of signal amplitude in the individual and combined steady-state frequency responses (Fig. 3.5). However, increasing n_c comes at the cost of a proportional

increase in time to acquire each cycle of images.

The shifted frequency response model in Eq. 3.10 describes how the combined frequency response is formed from n_c shifted copies of a single frequency response. An example of the individual and combined frequency responses can be seen in Fig. 3.3, showing how the combined response is periodic over $1/(n_c \cdot \mathrm{TR})$ Hz. Increasing n_c therefore increases the number of bands in the combined frequency response, however the signal drop within each band becomes less severe (Fig. 3.4).

The severity of the transient response of the combined signal was also found to vary as a function of frequency. Figure 3.7 shows the integrated transient response for selected values of n_c, accounting for differences in $\mathrm{TR}_{\mathrm{eff}}$. The maximum values of the integrated transient responses were comparable across tested n_c values. However, the inter-band spacing of each profile decreased as n_c was increased, similar to the steady-state signal variation seen in Figure 3.4. The minimum value in each band can be seen to be approximately zero, indicating that voxels at these frequencies would have very low sensitivity to physiological artifacts. However, scanner drift may shift the voxel mean frequency through regions of high and low frequency sensitivity over time, resulting in physiological artifacts that change in shape and amplitude over an fMRI timecourse. An example of this effect is shown in Figure 3.8 for $n_c = 10$.

While the severity of scanner drift is dependent on the system and gradient waveforms, drift-induced frequency changes are likely to be slow enough to be modeled as quasi-static in a correction strategy. However, our simulations indicate that respiration artifacts are primarily composed of transient effects rather than changes to steady-state magnitude under a quasi-static condition (Fig. 3.8). Transient signal behavior can be shown as frequency response distortions, as seen in Fig. 3.9. While the distortions to the individual OSSI frequency responses were found to be small, the signal combination step can result in constructive or destructive interference. This suggests that while the 2-norm combination strategy is an effective method for

steady-state OSSI signals, an improved method is needed to account for transient effects due to temporally varying frequency. This may include model-based strategies where frequency is a latent parameter, or data-decomposition methods that can separate transient signal artifacts from functional changes.

A limitation of these simulations is that magnetization is modeled as a single isochromat, ignoring the effects of intra-voxel field inhomogeneity. These effects are important for cases of small inter-band spacing, such as shown in Fig. 3.7 for $n_c = 14$. If an intra-voxel distribution of frequencies exceeded the width of a repeated unit of the frequency response, then the observed transient behavior would be invariant to the distribution mean frequency.

3.6 Conclusion

This work develops relevant models and improves understanding of the OSSI frequency response under static and dynamic conditions. An analysis of simulated OSSI combined signals shows that respiration artifacts are largely due to distortions to the frequency response which compound during 2-norm combination. These results suggest that future model-based correction strategies must account for transient signal behavior caused by respiration and cannot rely on a quasi-static approximation to produce accurate results.

CHAPTER IV

Retrospective Correction of Physiological Noise in OSSI

4.1 Introduction

OSSI exhibits a complicated response to respiration and drift induced frequency changes, where signal confounds appear non-linear and time-variant. Since behavior is more complex than physiological artifacts seen in GRE-based fMRI, previously proposed model-based correction methods such as RETROICOR [39] have not been found to be reliable. Instead, physiological noise in OSSI can be addressed using previous data-driven approaches that differentiate physiological noise from functional changes through a spatial or temporal model [42][41][44][46]. These methods do not rely on modeling the relationship between respiratory/cardiac phase and signal changes, and have found to be effective even when physiological noise is aliased.

To this end, we present a novel data-driven method for retrospective correction titled Oscillating Steady-State CORrection (OSSCOR). OSSCOR uses principal components as nuisance regressors, an approach similar to CompCor [41]. However, OSSCOR does not rely on specifying a noise ROI, and instead utilizes the unique signal properties of OSSI as a combined spatiotemporal model to differentiate functional activation from physiological noise. We also present a variation of our approach

deemed F-OSSCOR, where FID timecourses are used to generate nuisance regressors instead of image data. By using FID data, physiological noise is sampled every TR, independent of the slice or volume acquisition rate.

This paper first presents a signal model that describes the OSSI frequency-time signal relationship that is central to the OSSCOR method. Next, we show the effects of respiration and scanner drift on the OSSI signal using simulations, and then use these simulated effects to estimate the optimal number of principal components for an OSSCOR correction. Finally, we show that the use of OSSCOR-derived nuisance regressors in a task-based fMRI experiment can significantly reduce physiological noise compared to standard methods, as measured by activated voxels, mean t-score, and tSNR.

4.2 Methods

4.2.1 Image-Based Physiological Noise Estimation

Respiration and scanner drift both cause temporally varying frequency changes, but we will refer to the effects of both sources of undesired signal changes as "physiological noise" for simplicity. In this method, the concept of multiple frequency responses is generalized to a voxel timecourse. Since each of the signals for a given voxel in a period are acquired sequentially, the magnitude voxel timecourse $m \in \mathbb{R}_+^{n_t}$ for n_t timepoints can be reshaped into n_c columns:

$$\mathbf{M} = \begin{bmatrix} m(1) & m(2) & \dots & m(n_c) \\ m(n_c+1) & m(n_c+2) & \dots & m(2n_c) \\ \vdots & \vdots & \ddots & \vdots \\ m(n_t-n_c+1) & m(n_t-n_c+2) & \dots & m(n_t) \end{bmatrix}, \qquad [4.1]$$

where each row of $\mathbf{M} \in \mathbb{R}_+^{n_t/n_c \times n_c}$ contains one OSSI period of length n_c, and each

column is treated as a separate timecourse of length n_t/n_c. We refer to the columns of $\mathbf{M}$ herein as "phase timecourses," corresponding to the n_c phases of an OSSI period. Using this notation, we assume that the n_c phases in each row of $\mathbf{M}$ are acquired simultaneously, since the time to acquire each period (∼100ms) is considerably faster than respiration induced signal changes. Each row then forms one time point in the combined timecourse $c \in \mathbb{R}_+^{n_t/n_c}$:

$$c(i) = \sqrt{\sum_{j=1}^{n_c} \mathbf{M}_{ij}{}^2}. \qquad [4.2]$$

Each phase timecourse will have a different non-linear response to frequency changes as previously described by our multiple frequency response model (Eq. 3.10). This can be seen in Figure 4.1a, where simulated respiration and drift results in different physiological artifacts for each phase timecourse. Figure 4.1b shows how combining phase timecourses can cause constructive or destructive interference of physiological artifacts, an effect that can also change through time.

We can use the signal matrix representation in Eq. 4.1 to correct each phase timecourse prior to combination using our proposed method, OSSCOR. Since shifts of f_s/n_c Hz cyclically permute the columns of $\mathbf{M}$, the phase timecourses of voxels that differ by multiples of f_s/n_c Hz will have correlated physiological noise components. For typical values of f_s/n_c = 6-10 Hz, any voxel will have local and spatially disparate correlations across a single slice. By forming a block matrix $\mathbf{S}$ for all r voxels

$$\mathbf{S} = \begin{bmatrix} \mathbf{M}_1 & \mathbf{M}_2 & \dots & \mathbf{M}_r \end{bmatrix}, \qquad [4.3]$$

the low-rank physiological noise components of $\mathbf{S}$ can be estimated by principal component analysis (PCA). This is the central concept of OSSCOR, where the signal properties of OSSI allow for a small number of principal components to sufficiently describe the physiological noise in any phase timecourse at any spatial location. This

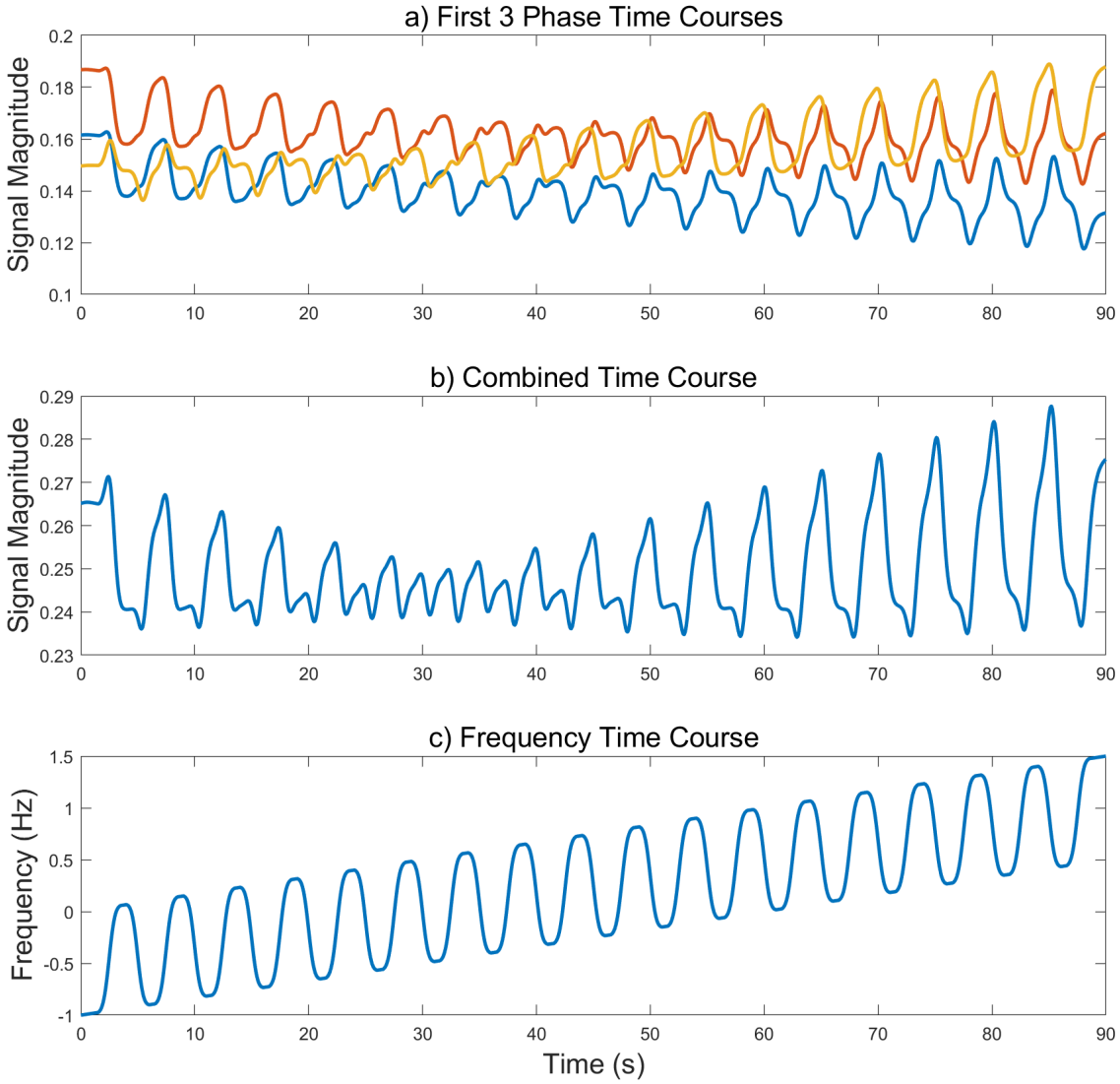

Figure 4.1: Simulated gray matter signals with respiration and scanner drift effects. Plot a) shows phase timecourses (3 of 6 plotted for clarity). Plot b) shows the associated combined timecourse. c) shows simulated B0 changes, modeled using two terms: a respiration waveform at 12 breaths/min and pk-pk amplitude of 1 Hz, and a linear scanner drift term of 1 Hz/min.

is similar to CompCor correction strategy, but differs in that principal components are estimated from all voxels and phase timecourses using the time-frequency relationship of OSSI instead of a specified noise ROI.

Once the principal components of $\mathbf{S}$ are determined, we can remove physiological noise components using the following signal model commonly used for BOLD fMRI:

$$\mathbf{S} = \mathbf{X}\beta_1 + \mathbf{T}\beta_2 + \mathbf{P}\beta_3 + \epsilon, \quad [4.4]$$

where $\mathbf{X}$ is a matrix of experimental design variables, $\mathbf{T}$ is a matrix of polynomial detrending terms, and $\mathbf{P}$ is a matrix containing principal components of $\mathbf{S}$ which act as nuisance regressors for physiological noise. $\beta_{1,2,3}$ contain weights for each respective matrix, and ϵ is random error. The use of polynomial terms $\mathbf{T}$ was not found to improve the performance of OSSCOR, but are included to maintain consistent degrees of freedom with CompCor in the later comparison.

The number of principal components was determined by simulating OSSI timecourses (TR = 15 ms, FA = 10°, n_c = 6) with temporally varying B0. We first simulated the physiological noise as a single temporally varying respiration component with waveform amplitudes of 0-2 Hz at steps of 0.1 Hz. The respiration rate was kept constant at 12 breaths/minute. Next, a linear drift component of 1 Hz/min was added to the respiration component for all frequency amplitude values. A center frequency offset was then added, specified as a range of ± 50 Hz at steps of 0.1 Hz. Variations in T1 and T2 were not found to affect the results of the simulation and were held constant at 1286 ms and 110 ms, respectively. Each of the 21,021 parameter combinations was initialized at steady-state and simulated for 90 seconds, then reshaped into a matrix of 126,126 phase timecourses per Eq. 4.1 and 4.3. PCA was then applied to the simulated timecourses. Based on the scree plot shown in Figure 4.2 from the simulated data, the top 6 principal components were qualitatively chosen to estimate physiological noise.

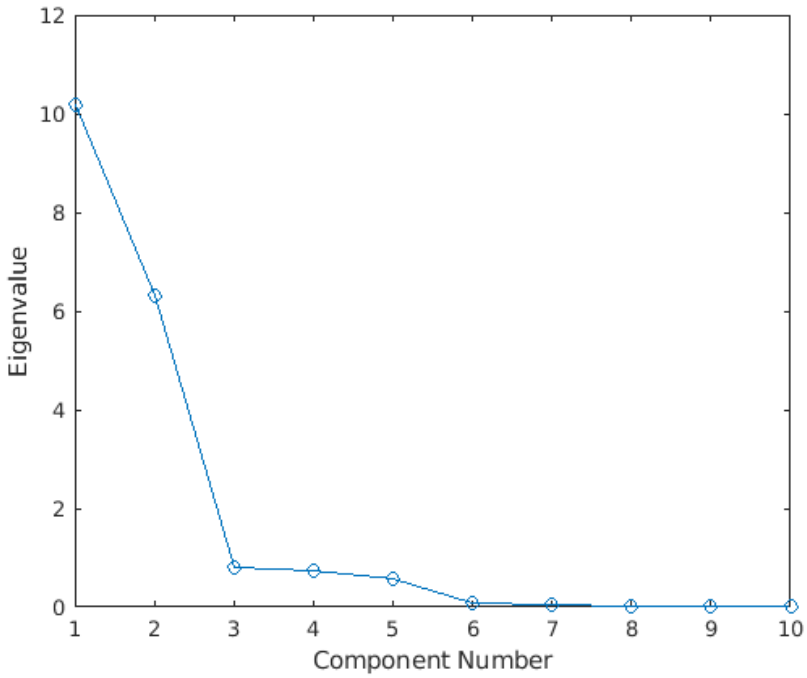

Figure 4.2: Scree plot of simulated phase timecourses with respiration and drift. Six principal components were chosen to sufficiently capture variation induced by respiration and drift.

4.2.2 FID Based Physiological Noise Estimation

In addition to image data, principal components can be determined from acquiring extra samples of the signal FID prior to readout. We refer to this as "F-OSSCOR", an FID-based variation of the previously described method. While this signal source is not spatially encoded using gradients, the individual coils in a receive-array provide spatially varying sensitivity to different regions of the brain, which in turn have varying distributions of off-resonant spins. Similar to a blind source separation problem, PCA can then be used to recover the independent signals that comprise the low-rank physiological noise subspace.

We implement this method by acquiring multiple samples at $k_{xy} = 0$ before readout, which are then averaged into a single magnitude value. This is performed coil-wise, resulting in n_{coil} measurements per TR. Considering these to be n_{coil} separate timecourses, the same OSSCOR methods previously described for image data are then applied. The number of FID samples was varied to determine its effect on the quality of estimates produced, which showed negligible improvement past 16 samples.

4.2.3 Experimental Setup

All studies (n=6 subjects) were performed on a 3T GE MR750 scanner (GE Healthcare, Waukesha, WI) with a 32-channel head coil (Nova Medical, Wilmington, MA). We implemented the OSSI pulse sequence using the vendor's pulse programming language, EPIC, as well as our own in-house pulse sequence development framework, TOPPE [85]. Single slice imaging was performed using a single shot constant-density spiral-out trajectory (TR = 17.5 ms, FA = 10°, FOV=19 × 19 cm^2, matrix = 45 × 45 reconstructed at 64 × 64, slice thickness = 2.5 mm, sampling BW = 250 kHz), with 16 extra k-space center samples prior to readout. Spatial distortions due to B0 field inhomogeneity were corrected using a separately acquired field map.

Subjects were presented with a visual stimulus composed of right- and left-hemifield

counter-phased 10-Hz flickering checkerboards in 40-second blocks, repeated 6 times (240 seconds). The subject was instructed to gaze at a fixation cross in the center of their visual field during the experiment.

4.2.4 Data Analysis

Analysis of functional data was performed using MATLAB (The Mathworks, Inc., Natick, MA). A block diagram illustrating the following analysis workflow is shown in Figure 4.3. The OSSCOR and F-OSSCOR analysis methods were applied by removing physiological noise components to phase timecourses $\mathbf{S}$ using least-squares fitting of the signal model (Eq. 4.4), which included the task waveform and linear/quadratic detrending terms. The denoised phase timecourses were then combined using Eq. 4.2, resulting in one denoised combined timecourse per voxel. For comparison, CompCor was implemented on combined timecourses with linear/quadratic detrending. Temporal standard deviation (tSTD) was used to select the top 2% of noisy voxels, discarding any timecourse with task correlation higher than 0.2 (tCompCor variation). In all methods, the resulting denoised combined timecourses were then evaluated for activation using a simple correlation threshold of $r > 0.5$. No high-pass filtering or spatial smoothing was performed.

Method performance was evaluated using average t-score, number of activated voxels, and average tSNR. Average t-score was calculated within a per-subject-ROI defined by the union of the activated voxels found in all correction methods. In counting the total number of activations, only voxels from the bottom-third of the brain could be considered true active, approximately corresponding to the visual cortex. Additionally, because the visual stimulus was counter-phased, only negative correlations were considered from the left hemisphere and positive correlations from the right hemisphere.

OSSCOR performs nuisance regression on each phase timecourse before combina-

tion using a least squares fit, which includes the task waveform. To test for multi-collinearity, the correlation between the task and each nuisance regressor (principal component) was inspected. Orthogonalization of the nuisance regressors to the task vector was also tested for its effects on denoising performance, calculated by:

$$\mathbf{P}_{\text{orth}} = (\mathbf{I} - \mathbf{X}\mathbf{X}^{\text{T}})\mathbf{P} \qquad [4.5]$$

where $\mathbf{P}$ is the orthonormal matrix of nuisance regressors, $\mathbf{X}$ is the task vector with unit norm, and $\mathbf{I}$ is the identity matrix with n_t/n_c columns and rows. Note that $\mathbf{X}^T$ is written instead of $\mathbf{X}^H$ since the task and nuisance regressors are all real-valued.

4.3 Results

The technique with detailed results from one subject (#4) is described here, with results for other subjects summarized in Table 4.1. Figure 4.4 shows activation and tSNR maps for the proposed methods, with CompCor for comparison. Across all six subjects, OSSCOR, F-OSSCOR, and CompCor all significantly improved the number of activated voxels (all $P < .03$), average t-score (all $P < .001$), and tSNR (all $P < .001$) compared to only polynomial detrending (Table 1). OSSCOR performed significantly better than CompCor in all three metrics ($P = .025, P = .042, P =$ 0.0025, respectively). F-OSSCOR results were not found to be significantly different compared to CompCor. An example of uncorrected and OSSCOR corrected phase timecourse is shown in Figure 4.5, illustrating successful reduction of high-frequency respiratory noise as well as drift induced low-frequency components.

Increasing the number of principal components used in OSSCOR resulted in decreased activation area and mean t-score, and an increase in false positives as defined by activations outside of the visual task ROI. This reduction of performance was observed across all subjects. However, increasing the rank of the F-OSSCOR im-

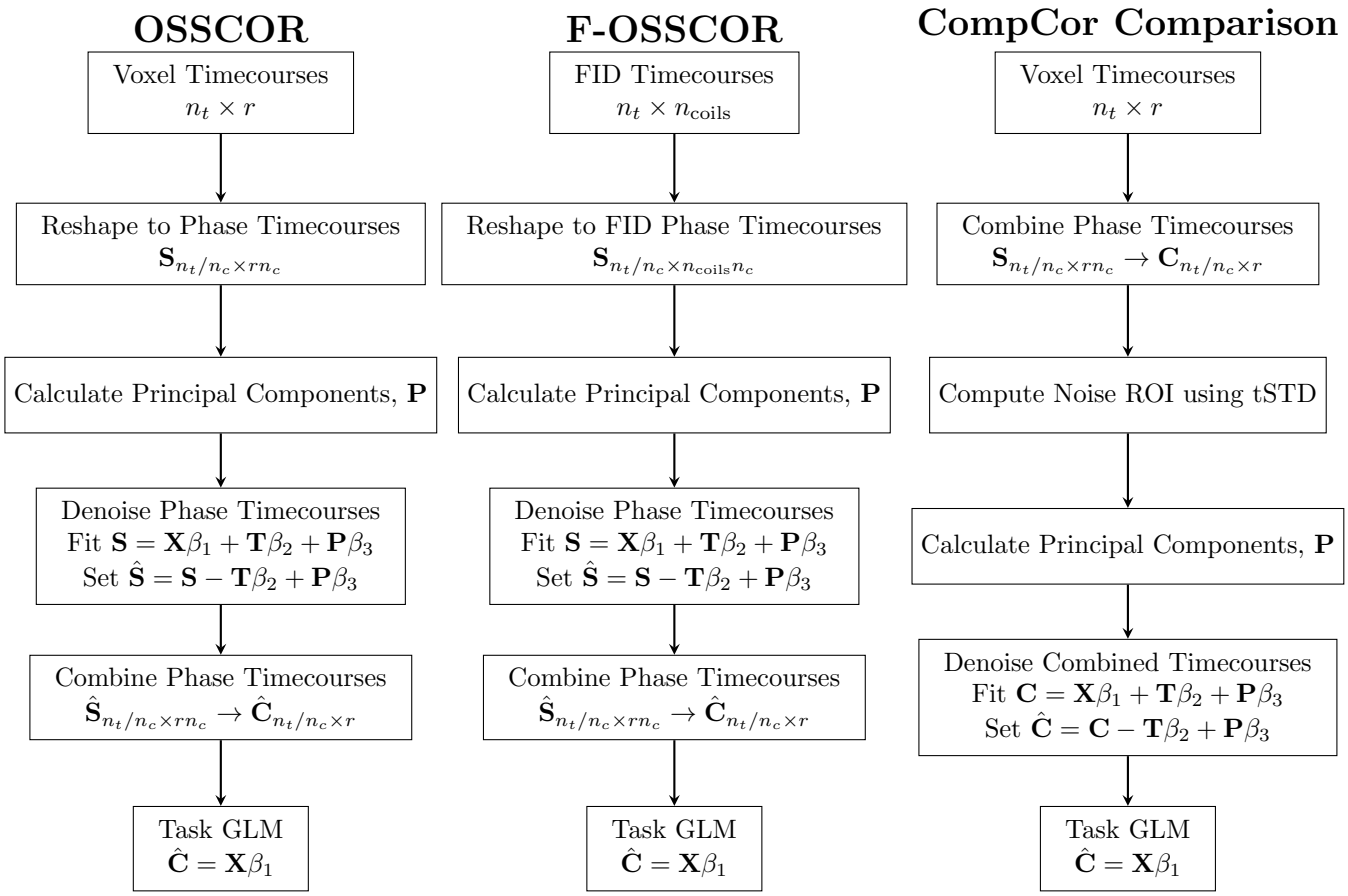

Figure 4.3: A diagram outlining the steps implemented for each analysis method. OSSCOR and F-OSSCOR both calculate principal components and perform denoising before phase timecourse combination, while CompCor was applied on the final combined timecourse.

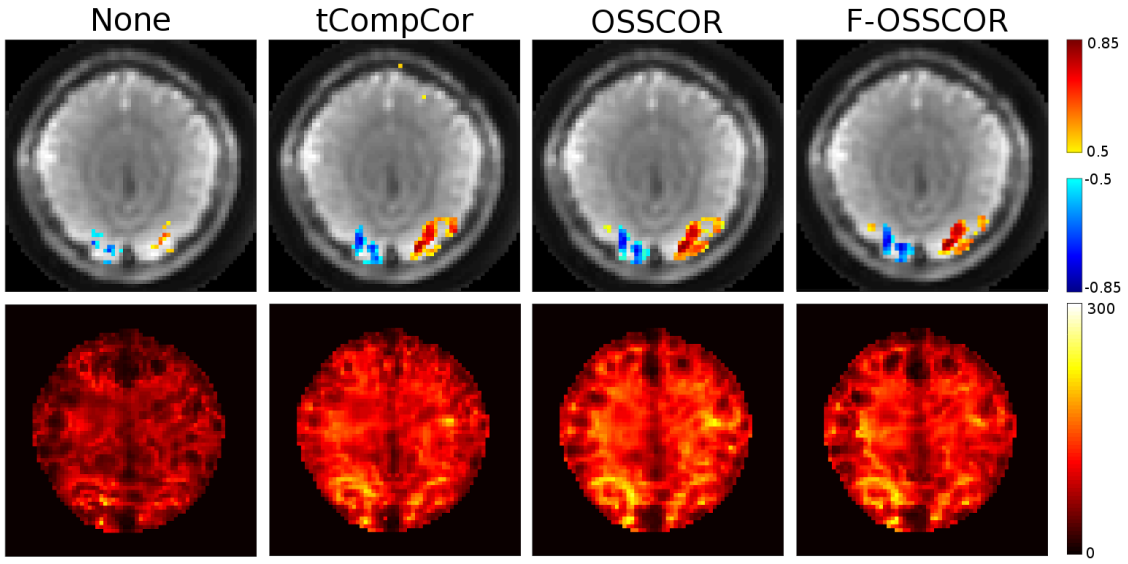

Figure 4.4: Activation and tSNR map for each respective correction methods: polynomial detrending only, CompCor, OSSCOR, and F-OSSCOR. OSSCOR outperformed both CompCor and F-OSSCOR, but all three correction methods significantly increased the number of activated voxels and mean tSNR. Voxels with a significant vascular component were observed to have lower tSNR than their surroundings, which is thought to be the effect of through-plane flow unable to reach steady-state due to the single-slice acquisition.

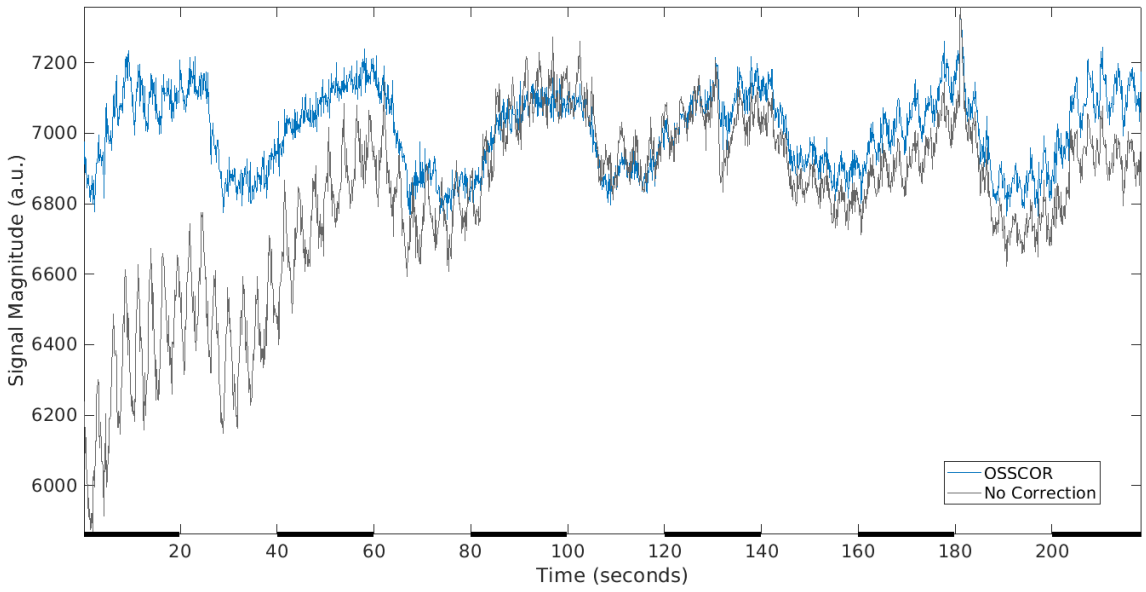

Figure 4.5: An example of uncorrected and OSSCOR corrected phase timecourses, with the visual task indicated by black bars on the x-axis. The uncorrected timecourse shows high sensitivity to respiration changes in the first minute of the scan which are greatly reduced by OSSCOR.

proved the number of activations and mean t-score across all subjects with little to no false activation. Activation maps for representative principal component numbers are shown in Figure 4.6.

Correlation between the task waveform and principal components for $k = 6$ was generally found to be low, and is summarized in Table 4.2. The absolute mean and standard deviation of correlation values was 0.064, and 0.048, respectively. An alternative analysis method where OSSCOR nuisance regressors were orthogonalized to the task was tested. Visual inspection of the resulting activation maps was found to reduce activation strength and increase the number of false positives, as shown in Figure 4.7.

Table 4.1: Summary of results from functional experiments

	Subject 1	**Subject 2**	**Subject 3**	**Subject 4**	**Subject 5**	**Subject 6**
Average t-score with detrending	15.1	26.4	38.3	19.0	19.2	27.5
Average t-score with CompCor	31.6	43.4	47.0	33.5	31.1	41.7
Average t-score with OSSCOR	34.5	44.3	49.4	38.6	41.5	43.2
Average t-score with F-OSSCOR	32.8	43.9	48.1	35.7	36.6	41.4
# activated voxels with detrending	0	16	53	27	10	39
# activated voxels with CompCor	22	32	66	91	19	67
# activated voxels with OSSCOR	30	31	71	109	34	75
# activated voxels with F-OSSCOR	28	28	70	87	27	63
Average tSNR with detrending	47.9	41.4	83.9	60.2	46.1	67.2
Average tSNR with CompCor	88.1	72.0	125.6	94.0	74.1	106.4
Average tSNR with OSSCOR	94.9	94.3	135.9	106.1	83.5	119.2
Average tSNR with F-OSSCOR	87.3	75.9	132.6	95.1	80.4	106.7

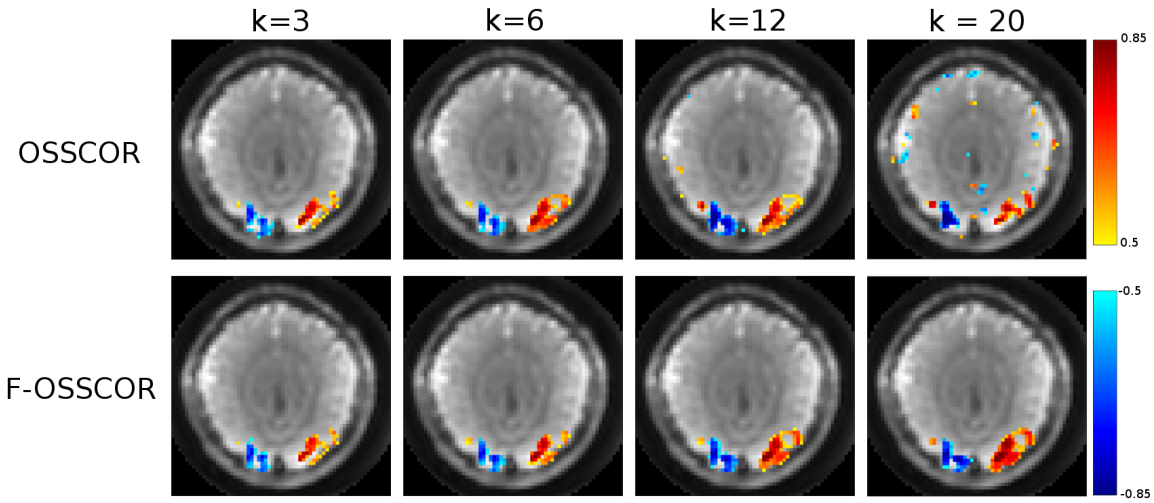

Figure 4.6: Activation maps for OSSCOR and F-OSSCOR produced with varying number of principal components (k). Increasing the number of OSSCOR PCs reduced activation sensitivity and increased the number of false positives, while increasing the number of F-OSSCOR PCs increased sensitivity without increasing false positives.

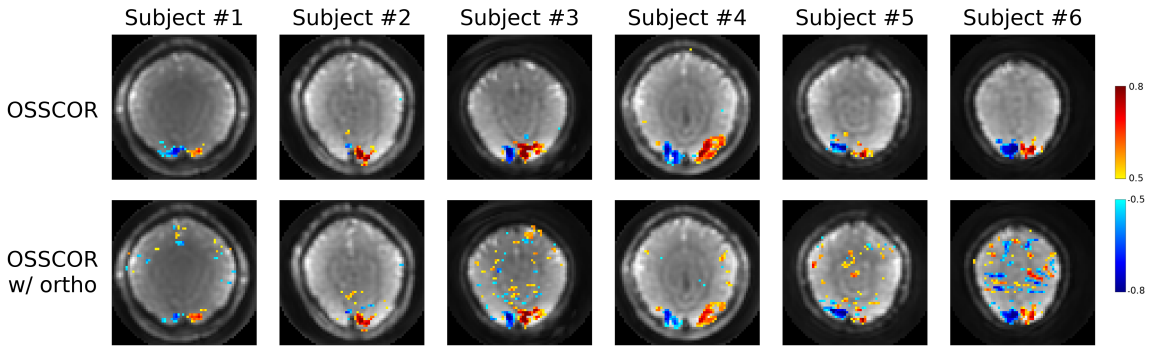

Figure 4.7: Activation maps for OSSCOR with and without nuisance regressors orthogonalized to the task vector (top and bottom rows, respectively). Orthogonalizing OSSCOR nuisance regressors to the task waveform prior to regression was found to decrease activation strength and increase false positives.

Table 4.2: Correlation of OSSCOR Principal Components with Task

	Subject 1	**Subject 2**	**Subject 3**	**Subject 4**	**Subject 5**	**Subject 6**
PC 1	0.023	0.004	-0.004	0.006	-0.022	0.015
PC 2	-0.101	-0.091	0.123	-0.106	-0.090	-0.160
PC 3	-0.014	0.024	0.113	0.023	-0.126	0.053
PC 4	0.097	0.047	0.100	-0.094	-0.034	0.175
PC 5	-0.039	0.007	0.057	-0.127	0.087	-0.054
PC 6	0.059	0.120	-0.009	-0.050	-0.027	-0.009

4.4 Discussion

The "phase timecourse" analysis of OSSCOR is based on the assumption that the time to acquire each period of n_c TRs is much shorter than the time-scales at which respiration and drift occur. Therefore, temporally varying frequency and resulting transient effects can be treated as quasi-static over the duration of a full n_c OSSI period. This assumption does not imply that transient effects are negligible, but rather are slowly varying compared to the speed to acquire a period, $\mathrm{TR}_{\mathrm{eff}}$. This assumption performs well at the chosen parameters ($n_c = 6$, $\mathrm{TR}_{\mathrm{eff}} = 105$ ms), though we found in initial tests that longer readouts or higher n_c values reduced the effectiveness of OSSCOR. Furthermore, higher values of n_c result in reduced amplitude of respiration and drift artifacts due to a more stable combined frequency response, reducing the need for retrospective correction. For example, a period of $n_c = 10$ was shown to have a combined frequency response variation of less than 5% compared to the 17% variation of $n_c = 6$, though at the cost of a 66% longer $\mathrm{TR}_{\mathrm{eff}}$.

F-OSSCOR extends the OSSCOR method by using FID timecourses instead of voxel timecourses. Though not spatially encoded, the FID time series data can be used to estimate spatially varying physiological noise due to two sources of signal diversity: coil sensitivity and B0 inhomogeneity. Since the FID signal is detected independently per coil, each FID timecourse is spatially localized by each coil's sensitivity. Therefore, each coil will only be sensitive to a local distribution of off-resonant spins, and by extension, sensitive to a local portion of the OSSI frequency response. Furthermore, OSSI effectively acquires a sequence of n_c different images with different center frequencies, resulting in each coil receiving FID signals from n_c different regions of the frequency response. In our experimental setup using a 32-channel head array and $n_c = 6$, the 192 separate FID timecourses produced for the F-OSSCOR analysis were sufficient for correcting the data. An additional benefit of the F-OSSCOR approach is that the requisite FID signals are measured every TR regardless of the

encoding strategy, and is therefore compatible with any multi-shot, 3D, or undersampling scheme.

The concept of using FID-based nuisance regressors assumes that FID signal variance due to functional signal changes will be small compared to respiration or drift artifacts. This is supported by the comparison shown in Figure 4.6, which shows OSSCOR and F-OSSCOR activation maps using a varying number of principal components. As principal components were increased passed the theorized rank of the physiological noise, OSSCOR functional sensitivity and specificity decreased in all subjects. This can be seen as a decreased activation area and strength, as well as an increased amount of suspected false activations. In contrast, increasing the number of principal components in F-OSSCOR increased activation strength with minimal reduction in specificity across subjects, though maintained similar activation areas. This experimental result suggests that F-OSSCOR could be used in rs-fMRI denoising like CompCor with the advantage of having less sensitivity to the number of principal components chosen.

Both OSSCOR and F-OSSCOR use PCA to produce nuisance regressors for subsequent functional analysis, similar to the CompCor denoising approach. However, a fundamental difference is that CompCor seeks to target noisy voxels and exclude activated voxels from the PCA by specifying a noise ROI, while OSSCOR and F-OSSCOR include all data. Despite including activated voxels in the PCA analysis, OSSCOR performed significantly better than CompCor in all three test metrics, and F-OSSCOR performed comparably to CompCor. This is attributed to the second difference in methods: OSSCOR and F-OSSCOR both perform corrections using phase-time data before combination, and therefore gain the ability to make comparisons across both space and time using the OSSI frequency-time shift property. In the case of OSSCOR, including all voxels as inputs was found to be critical, as excluding voxels via a tSTD threshold resulted in a loss of denoising performance.

This implies that a sufficient range of off-resonant signals needs to be included in the analysis and that only selecting timecourses with high tSTD results in a limited range of off-resonant behaviors represented in the nuisance regressors. Including all timecourses in OSSCOR does creates the possibility of the nuisance regressors representing functional signal instead of noise, which would result in decreased functional sensitivity. However, this was not observed in the data, as supported by the increases in functional sensitivity of OSSCOR compared to CompCor, which excluded functional voxels via a noise ROI. Since the majority of voxels included in the analysis contain physiological noise but no functional signal, noise is expected to dominate the first principal components.

Our implementation of CompCor excluded timecourses that were correlated with the task above a threshold, though this pre-processing step was found to be unimportant for analyzing OSSI data. This result was confirmed by manually inspecting the unmodified tSTD-derived ROI, which did not include voxels near the activated regions of the visual cortex. This pre-processing step was tested with OSSCOR to exclude phase timecourses potentially containing functional signal, but was also found to have a negligible impact. Pre-processing the data using second-order polynomial detrending was effective at removing slowly varying noise components attributed to drift. This detrending step was found to be essential for defining the CompCor noise ROI based on tSTD, since respiration-induced noise magnitude is small compared to drift. However, the detrending step had a negligible effect on OSSCOR since no ROI is used and low-frequency components are captured in the principal components. Though not necessary, polynomial detrending terms were included in OSSCOR and F-OSSCOR in order to match the degrees of freedom in method comparisons.

While OSSCOR and F-OSSCOR demonstrate the ability to mitigate the effects of respiratory and scanner drift induced frequency changes in OSSI, both methods inherit limitations of data-driven correction approaches. The first is the selection of

how many principal components should be included in the analysis. Here we have shown a rank can be selected through simulation, however, this does not account for subject-specific B0 distributions or temporally varying respiration rates. This can lead to a deterioration of performance for some frequencies, as shown in the last two stimulus blocks in Figure 4.5 where no respiration artifacts are removed. Furthermore, flow-related artifacts in OSSI result in complex frequency-dependent signal evolutions, which were not well corrected by either proposed methods or CompCor. This effect can be seen in Fig. 4.4, where tSNR did not improve in areas with significant vascular components. Further work is needed to determine how to improve the dimensionality of the physiological noise representation to improve denoising while excluding functional signal components. This could potentially be performed using alternative unsupervised methods based on ICA or dictionary learning.

4.5 Conclusion

We have shown that the application of OSSCOR and F-OSSCOR can significantly reduce physiological noise due to temporally varying off-resonance during an OSSI-based fMRI acquisition. Unlike the previous PCA based methods such as CompCor, OSSCOR does not require the selection of a designated noise ROI and instead uses OSSI-specific signal properties to determine correlated physiological noise components. Similarly, we show through F-OSSCOR that FID samples can be used to produce nuisance regressors independent of the image encoding strategy.

CHAPTER V

Prospective Correction of B0 Changes in OSSI

5.1 Introduction

Retrospective correction is an effective way to remove respiration artifacts from fMRI data, though all retrospective strategies are ultimately "undoing damage" done to the underlying signal during acquisition. This is regarded as acceptable for SPGR based fMRI for two reasons. The first reason is that the effects of respiration and drift are approximately uniform at the scale of a voxel and therefore does not alter the intravoxel frequency distribution or subsequent T2* weighting. The second is that SPGR signal spoiling intentionally disrupts transverse signal formation at the end of each TR with large gradient-induced phase changes, preventing any off-resonance induced phase accumulation from affecting the next TR. These two factors are not valid for OSSI based fMRI, where the T2* sensitivity and signal magnitude for individual images can be altered by frequency fluctuations. OSSI attempts to solve both problems through the image combination step, where n_c images from a cycle are combined into a single image using the 2-norm. In this way, a frequency change that reduces the T2* weighting in one image is made up for by an increase in T2* weighting of others in the cycle.

Prospective correction methods are a different approach for cleaning physiological noise from fMRI signals, where corrections are applied in real-time to reduce

perturbations to the acquired MRI signal. Previous work has shown that real-time approaches are effective at compensating for respiration and drift artifacts, where the center frequency or shims are dynamically adjusted to negate changes to the B0 field [57][58][60]. Since compensation is performed concurrently with image acquisition, prospective correction prevents changes to signal characteristics before they occur, preventing fluctuations to signal magnitude or T2* weighting. Unlike retrospective approaches, prospective correction eliminates the need to account for physiological noise in a signal model and can potentially be used in combination with any image reconstruction strategy.

Though real-time prospective correction has previously been used for B0 compensation in SPGR and transition-band fMRI approaches, we are not aware of any research to date that has attempted real-time tracking in combination with a phase-cycled steady-state imaging sequence such as OSSI. Furthermore, implementing an OSSI-compatible real-time system is not straightforward due to a complex steady-state and atypical frequency response. This chapter explores the technical feasibility of using a real-time B0 compensation method in combination with OSSI, documenting a proof of concept implementation and application in task-based fMRI.

5.2 Theory and Methods

5.2.1 Real-time B0 Compensation

Uniform changes to the B0 field can be compensated for in real-time by changing the center frequency of the hardware oscillator, or by changing the phase of the transmitted/received RF. The former changes the rotating reference frame for transmitted and received signals, while the latter adds a constant phase offset to RF pulse and subtracts a phase offset from the received data. This is a subtle yet important difference for implementing a real-time compensation strategy: changing the center

frequency through the oscillator will change observed phase accumulation over a TR while changing the RF phase does not.

The following describes the latter approach for B0 compensation because it was found to be easier to implement RF phase changes due to scanner idiosyncrasies. B0 changes can be compensated for by adjusting a constant increment to the RF phase (ψ_B in Equation 3.5), resulting in a frequency response shift. Then, a uniform change in off-resonance can be negated by shifting the frequency response the same amount:

$$\psi_B = 2\pi \cdot \Delta\omega \cdot \mathrm{TR}^{-1} \qquad [5.1]$$

For example, a sequence with a TR of 16 ms would yield a frequency-response which is periodic over $1/(16\text{ ms}) = 62.5$ Hz. A whole-image off-resonance increase of 2 Hz could then be compensated for by increasing ψ_B by $2\pi \cdot (2\text{ Hz})/(62.5\text{ Hz}) \approx 0.2$ radians.

5.2.2 Correcting Changes in Off-Resonance using FID Signals

Previous work has utilized FID phase at the beginning of readout to measure relative changes in off-resonance in transition-band fMRI [57]. This approach uses the fact that changes in frequency are proportional to FID phase changes within the central transition band-region of the frequency response, and that all signals can be shimmed to this narrow spectral region. This region of linearity in the transition-band frequency response is shown in Figure 5.1. This approach does not work for an entire slice or volume since the strict shimming requirements cannot be met for larger spatial extents. Furthermore, the assumption of linearity does not hold true for OSSI, where signal phase varies non-linearly with off-resonance, as shown in Figure 5.2.

We propose a variation of this method that overcomes both of these challenges, where the FID phase is sampled before and after the readout. Since the readout is balanced, the relative phase change between these two measurements will be propor-

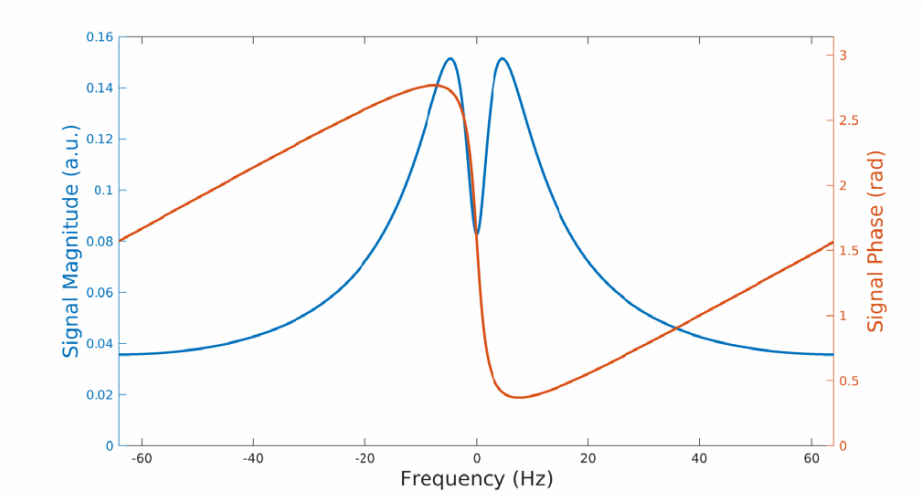

Figure 5.1: Magnitude and Phase Frequency Response for transition-band fMRI, showing how signal phase varies linearly with frequency near the center of the spectrum.

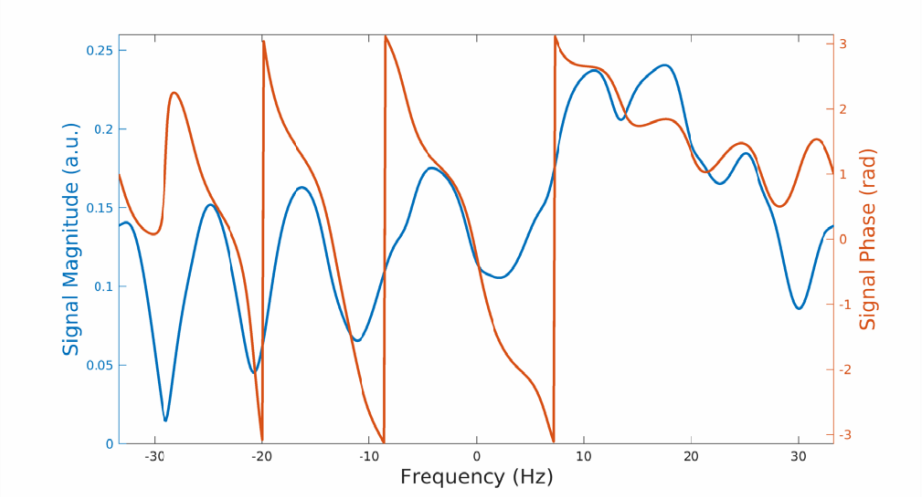

Figure 5.2: Magnitude and Phase Frequency Response for OSSI ($n_c = 10$)

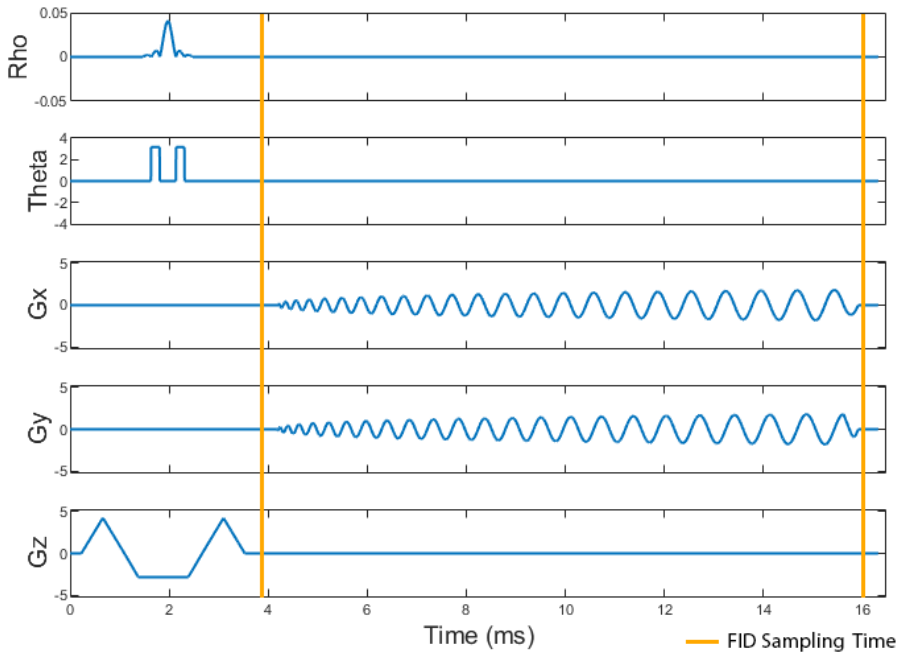

Figure 5.3: OSSI Pulse Sequence showing approximate FID sampling locations

tional to the amount of bulk off-resonance. A pulse sequence diagram illustrating the FID sampling method can be seen in Figure 5.3.

The relative FID phase is evaluated separately for each of the 32 coils used in the experimental setup. Since the effects of respiration do not uniformly affect the brain, each coil will be sensitive to different amounts of respiration-induced phase changes. We choose to combine all of these phase measurements into one combined by using an SVD-based coil compression [86], resulting in one FID phase value per TR, $\hat{\phi}$. Our approach only uses the phase from one user-selected TR per OSSI cycle. This is because we observed that OSSI images with low uniformity or SNR result in unreliable phase measurements, reducing the prospective correction effectiveness.

One advantage of using our relative FID phase approach is that the FID signal can be sampled every OSSI cycle and is therefore compatible with any k-space trajectory, similar to F-OSSCOR. This is a critical requirement of OSSI since high resolution or volume imaging requires the use of a multishot acquisition. However, each shot trajectory will have a different phase offset due to shot dependent eddy currents. We

correct for initial phase offsets by measuring the mean phase for each shot at the beginning of the scan, then subtracting the mean phase offset from each subsequent shot. This effectively aligns the phase of all shots by shifting the initial phase of each per-shot FID timecourse to 0.

The corrected phase measurement, $\hat{\phi}$, is then used to update the constant RF phase increment using the following relationship:

$$\psi_B = c \cdot \hat{\phi} \cdot \frac{\mathrm{TR}}{\Delta\mathrm{TE}} \qquad [5.2]$$

where ΔTE is the time between the two FID measurements, and c is the scaling parameter that maximizes signal stability in a region of interest. If the effects of respiration are uniform across the entire slice, then c will equal 1. However, if respiration effects are stronger or weaker in the ROI to stabilize compared to the rest of the slice, c will be greater or less than 1, respectively. In this way, real-time tracking can be tuned to maximize signal stability in a specific region of the slice, even when the effects of respiration are not uniform.

In practice, the scaling parameter, c, can be set manually or automatically. Our online automatic tuning method utilized a hill climbing algorithm to maximize the tSNR for each OSSI phase image in a user-specified region, defined by:

$$\mathrm{tSNR} = \frac{\bar{s}_{\mathrm{ROI}}}{\sigma_{\mathrm{ROI}}} \qquad [5.3]$$

where $\bar{s}_{\mathrm{ROI}}$ and σ_{ROI} are the mean and standard deviation of the ROI timecourses for a 10 second period.

5.2.3 Simulations

Bloch simulation was used to investigate the feasibility of using real-time tracking with the OSSI method. First, B0, T2, proton density, and coil sensitivity maps of a

human volunteer was acquired, with the quantitative maps shown in Figure 5.4.

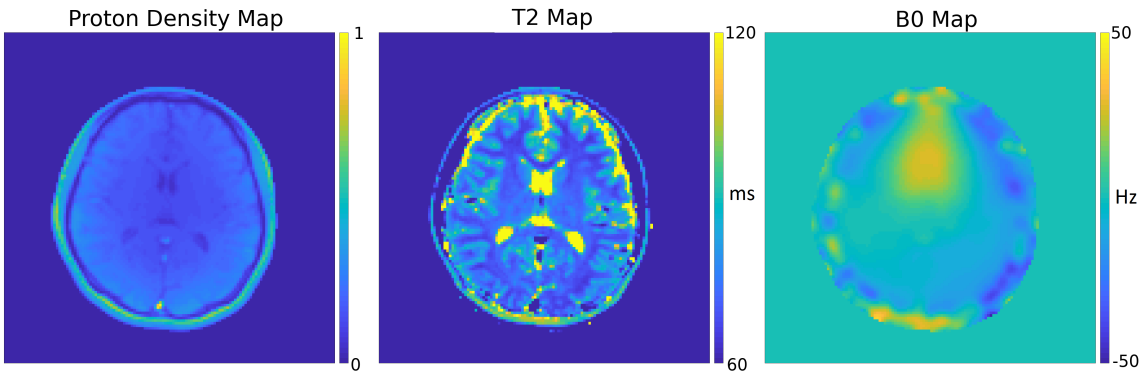

Figure 5.4: Acquired proton density, T2, and B0 maps used for simulation.

An OSSI timecourse simulation was performed using physical properties from the acquired maps and an additional time-varying frequency component, using our method previously developed for 1D simulation (Fig. 3.2). Real-time tracking was then simulated on a per-TR basis for 30 seconds. A FID phase calculation was performed for the last TR in each simulated OSSI cycle, where the complex simulated image was multiplied by the 32 acquired sensitivity maps and summed to produce 32 simulated FID phase measurements. The phase measurements were then coil combined to produce a single phase measurement, which was multiplied by a scaling parameter c to adjust the RF phase for the next simulated OSSI cycle. Although the combined OSSI signal frequency sensitivity decreases as n_c increases (Ch. III), increasing n_c reduces the update frequency of the real-time tracking system since only one out of n_c cycles is used for the phase estimate. Simulations were run for a range of values for n_c and c to investigate the interaction between these two parameters.

5.2.4 Phantom and In Vivo Experimental Protocols

The OSSI sequence and prospective correction method were implemented using the RTHawk real-time scanner control software (HeartVista, Los Altos, CA). More details about the technical implementation of the system can be found in Appendix A.

A 2D single slice readout was implemented using a 2-shot balanced spiral trajectory (TR=16ms, FA=10°, n_c=10), resulting in a combined image effective TR of 320 ms. An additional FID sampling readout section was placed before and after the spiral readout (approx 100 µs each). FID phase measurements were calculated on a per-coil basis, then coil compressed. The coil compression matrix was calculated from the first image of the time series. The FID phase measurement was then used to immediately update the constant RF phase increment, approximately 10-20 ms after the server received the data. Only one measurement out of each OSSI cycle was used to update the RF phase (every 160 ms).

Phantom experiments were used to assess the performance of online parameter tuning and real-time tracking. Frequency changes were expected to be approximately uniform across an axial slice due to scanner drift. Tracking stability as a function of scan duration was measured by acquiring a 10-minute run, then calculating tSNR maps from the first 0.5, 2, 3, 5, and 10 minutes of the data.

In vivo performance was tested using task-based fMRI experiments, consisting of a counter-phased flashing checkerboard (20 seconds per block, 4 minutes total). Tracking was enabled in the first trial, then disabled for the second. The pulse sequence was continuously run for the entire experiment, ensuring that the tracking on and tracking off trials used the same spatial location, shim values, and center frequency. The OSSI fast-time point to track was qualitatively determined by visualizing the OSSI images in real-time and selecting the fast-time image with good signal intensity in the posterior portion of the slice, corresponding to the ROI where visual activation was expected to occur. Linear and quadratic detrending were included in the functional analysis. No other spatial smoothing or post-processing steps were applied.

Table 5.1: Peak and FWHM tSNR values for selected n_c values

n_c	Peak tSNR	FWHM
2	410.4	0.163
4	371.9	0.390
6	232.8	0.634
8	150.1	0.960
10	172.6	1.15
12	157.1	1.55
14	155.3	2.00

5.3 Results

5.3.1 Simulation Results

Figure 5.5 shows example simulated OSSI images created from the quantitative maps from Figure 5.4, showing one OSSI cycle of $n_c = 10$.

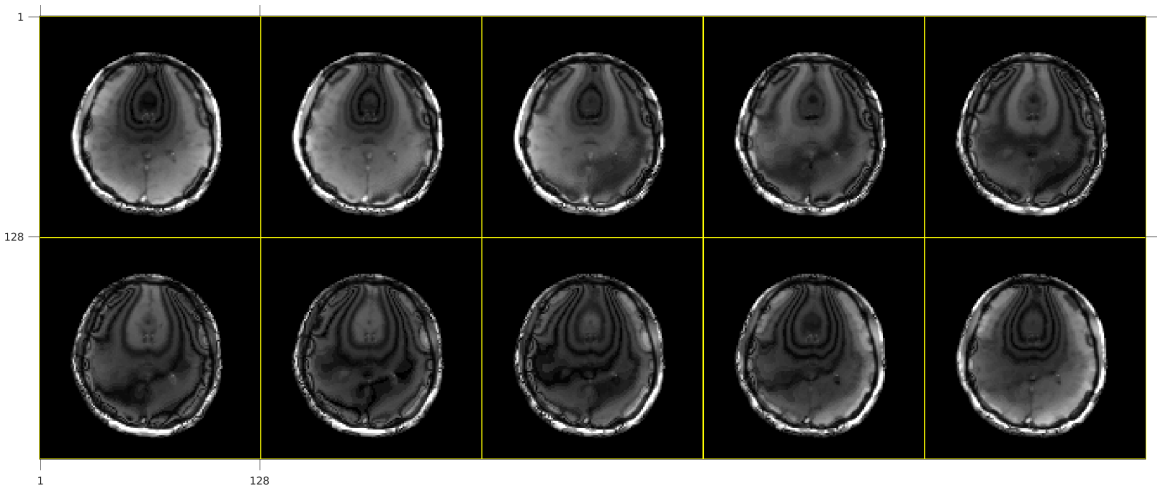

Figure 5.5: Simulated OSS images with $n_c = 10$

Figure 5.6 shows mean tSNR for a range of simulated c values, plotted for selected n_c values of 6, 10, and 14. The peak tSNR of each curve increased with lower n_c values. Sensitivity to c increased with lower values of n_c as well, as measured by the full width at half maximum (FWHM). A summary of peak tSNR and FWHM for n_c values from 2 to 14 is shown in Table 5.1.

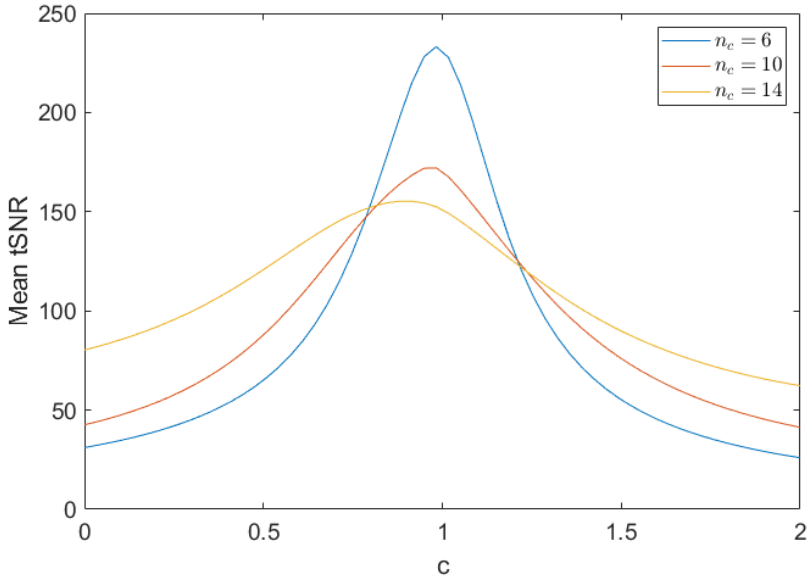

Figure 5.6: tSNR vs c for $n_c = 6$, 10, and 14.

Table 5.2: Mean tSNR of tracking on and tracking off phantom trials

	30 seconds	2 minutes	3 minutes	5 minutes	10 minutes
Tracking On	448.6	418.7	407.9	384.2	322.1
Tracking Off	471.6	336.5	285.0	217.7	141.5

5.3.2 Phantom Results

Based on the simulation results, phantom imaging was conducted with $n_c = 10$, which was qualitatively selected for the best combination of peak tSNR, sensitivity to c, and effective TR. Figure 5.7 shows tSNR maps calculated from the first 0.5, 2, 3, 5, and 10 minutes of images for both tracking on and tracking off trials. Mean tSNR for each map is summarized in Table 5.2. Both trials exhibit very high tSNR for the first 30 seconds of data since minimal changes to the B0 field have occurred, with tSNR decreasing through time. However, real-time tracking substantially improved the quality of subsequent tSNR maps compared to the no tracking trial, both in qualitative homogeneity and mean tSNR.

The source of the banding in the tSNR maps is due to B0 inhomogeneity resulting

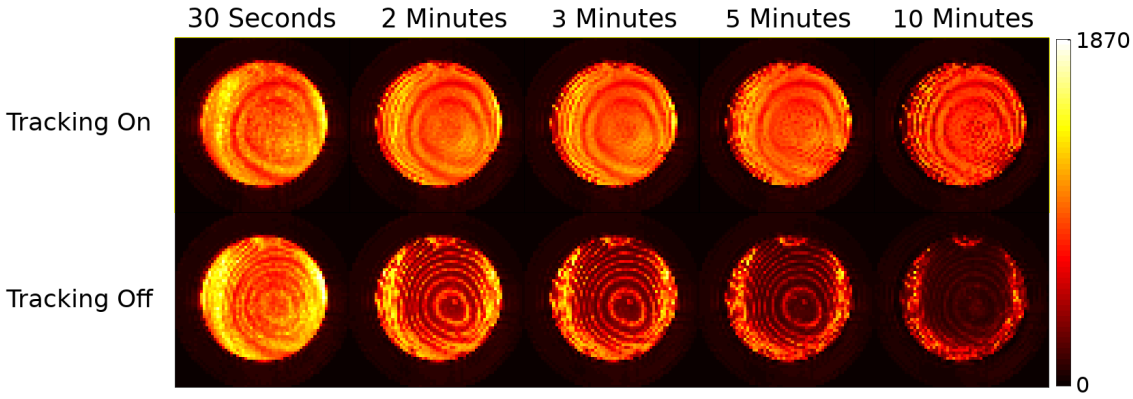

Figure 5.7: Phantom tSNR maps of tracking on and tracking off trials. tSNR maps were computed for the first 0.5, 2, 3, 5, and 10 minutes of OSSI combined frames. Tracking reduces the shifting of OSSI signal bands, reducing the variability of the combined images over time. Tracking resulted in a 134% improvement in mean tSNR vs no tracking at the 10 minute interval.

in a banding pattern across each OSSI image. While the image combination step results in a "combined frequency response" with less variance, the response is still not completely uniform. Scanner drift then results in apparent movement of the signal bands, changing the signal amplitude in a voxel and reducing the tSNR. The effects of drift can be seen in Figure 5.8, showing OSSI images from a selected phase in the cycle at the 0.5, 2, 3, 5, and 10 minute mark. Real-time tracking negates the effects of scanner drift, virtually eliminating any movement of the banding artifacts in the top row of mages. However, the bottom row of images shows how the banding artifacts will gradually shift when tracking is disabled.

5.3.3 In Vivo Results

Activation and tSNR maps shown for an in vivo trial in Figure 5.9 using $n_c = 10$. Tracking dramatically improved the number of activated voxels (72 vs. 13, 454% increase). Tracking also improved mean tSNR compared to no tracking (176.9 vs. 97.7, 81% increase). tSNR in voxels containing significant CSF or vascular components did

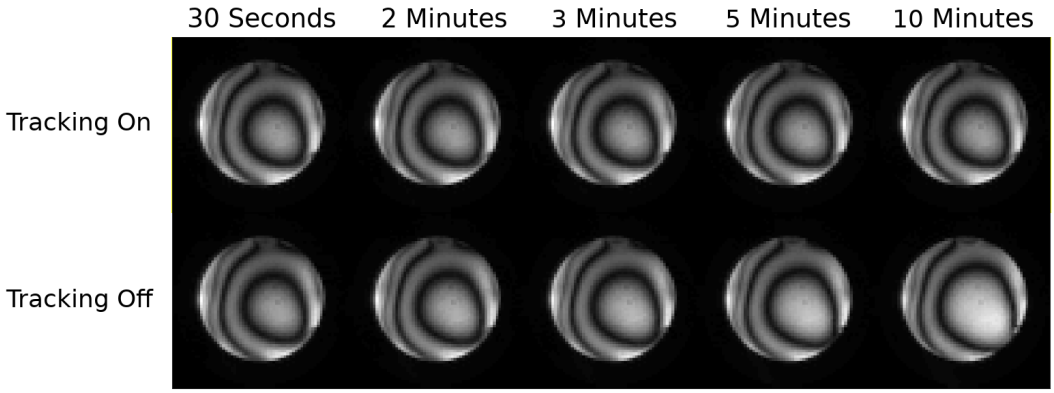

Figure 5.8: Example OSSI images at selected timepoints from a minute run, showing phase 7 of 10. The OSSI banding pattern remains stable over the 10 minute run when tracking is enabled, while disabling tracking shows a gradual change in band position.

not noticeably improve since flow-related artifacts cannot be compensated for using B0 tracking.

Example timecourses with tracking on and off are shown in Figure 5.10. Real-time tracking is shown to strongly reduce the effects of respiration, improving functional task correlation. The amplitude of respiration artifacts can be seen to temporally vary in the tracking-off timecourse as the underlying frequency sensitivity changes over time due to drift. Tracking-on and tracking-off correlation values for the plotted timecourses were r=0.86 and r=0.59, respectively.

5.4 Discussion

Our real-time prospective correction approach has demonstrated the ability to mitigate the effects of respiration and drift artifacts in OSSI by compensating for bulk B0 changes. While the control system implemented requires online tuning of a scaling parameter, c, simulation results from Figure 5.6 shows that modest deviations from the optimal parameter value still reduce the effects of B0 changes and improve

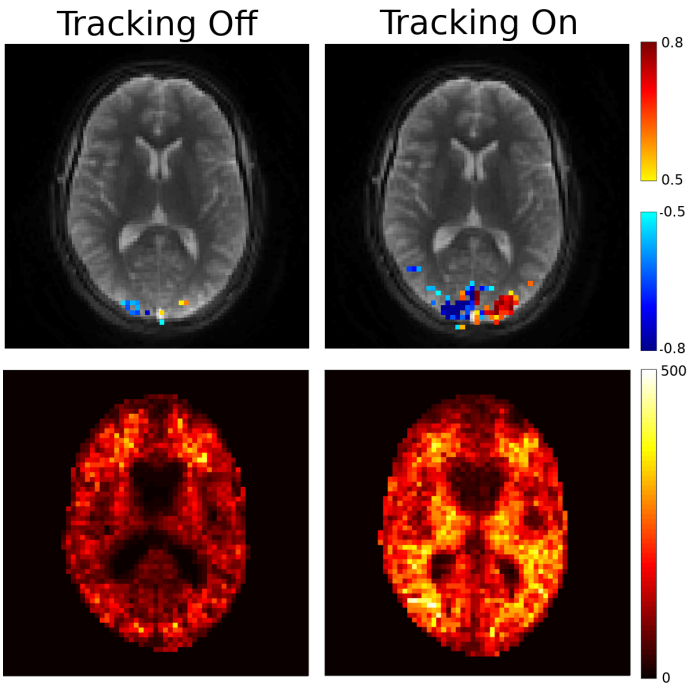

Figure 5.9: Activation and tSNR maps comparing tracking-off and tracking-on trials

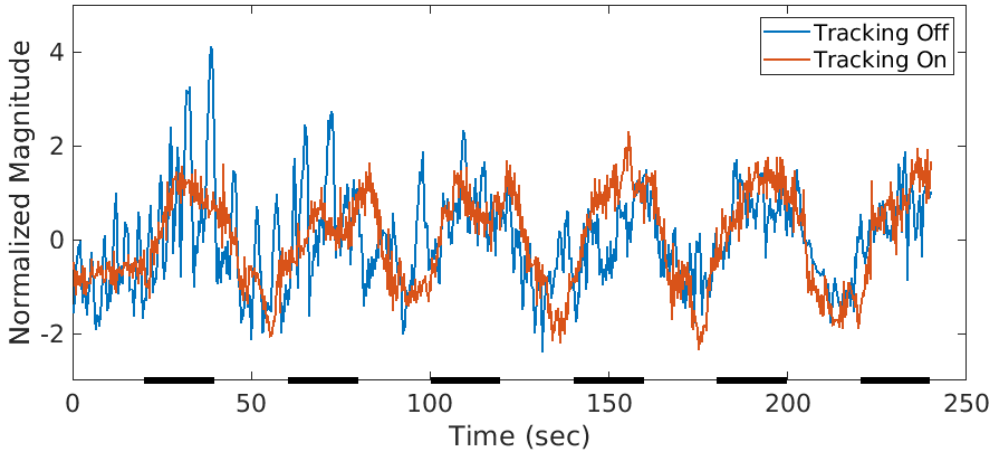

Figure 5.10: Example voxel time courses showing activation from a tracking-off and tracking-on trial. Black bars on the x-axis indicate stimulus blocks. Linear and quadratic detrending was applied to each timecourse before normalization.

tSNR. Equivalently, a c value optimized for a specific region of the brain can also improve stability in other regions, even if the other regions have stronger or weaker respiration effects. Increasing n_c is shown to improve tracking robustness as a function of c, suggesting that larger n_c values could improve signal stability even with spatially varying respiration effects. Evidence of this is shown in Figure 5.9, where tracking improved tSNR across the entire slice even though the effects of respiration are measured to be higher in the visual cortex due to the oblique slice planning.

The relative FID phase measurement approach only relies on using a balanced readout trajectory, where the center of k-space can be sampled before and after the readout. While this strategy allows the FID signal sampled every TR regardless of the slice or volume acquisition rate, the FID phase will contain inaccuracies dependent on eddy currents and gradient inaccuracies specific to a k-space trajectory. Our simple approach of subtracting the initial mean phase works well, effectively setting the initial phase of all timepoints to 0. This phase centering step was found to work well even with subject respiration since the mean phase values were computed from an average of several TRs.

Our real-time control system sets the constant RF phase increment proportionally to the FID phase measurement, which can be described as an open-loop control system. The system is open since changing the RF phase does not alter the rotating reference frame, resulting in no feedback to the relative FID phase measurement. This can result in poor tracking performance if c is set inaccurately, with tracking errors that scale with the magnitude of field deviations. This can be seen in the phantom data (Fig. 5.7), where tSNR was observed to decrease over time as drift continues to increase. Furthermore, changing the RF phase does not compensate for the effects of changing off-resonance in the image encoding, which would result in increased ghosting in EPI or blurring of a spiral image. A closed-loop approach that modifies the center frequency could address both of these issues by not requiring the tuning

of a scaling parameter. Rather, a closed-loop system would continuously monitor and minimize a phase error metric, potentially resulting in better stability over long periods of time. However, common closed-loop strategies such as PID controllers [87] still require a complex tuning process of control gains that can drastically affect the stability and performance of real-time compensation.

5.5 Conclusion

This proof of concept shows that FID signals can be used to estimate bulk B0 changes in real-time. The system also for per-shot eddy current effects, updating the RF transmit and receive phases to mitigate perturbations to the oscillating steady-state. Ultimately, this results in an increase of activated voxels, increased activation strength, and increased overall tSNR.

CHAPTER VI

Future Work

6.1 Catalyzation of the OSSI Steady-State

Like many other steady-state sequences, the OSSI sequence takes time to reach steady-state before imaging can be performed. The OSSI sequence can take several hundred TRs to reach steady-state, which is on the order of seconds. While this delay is not prohibitive if the sequence is only started once, it prevents a naive use of preparation pulses which would regularly interrupt the steady-state (ex. fat suppression). "Catalyzation sequences" are a common approach to minimizing the amount of time to establish steady-state, consisting of specific excitations and gradients played before the regular sequence [18].

Previous work showed that catalyzing a bSSFP sequence can be divided into "scaling" and "directing" steps, which separately address the longitudinal and transverse magnetization components of the steady-state [71]. We observe that the OSSI steady-state formation is limited by T1 effects and hypothesize that a similar catalyzation approach may be effective. Figure 6.1 shows the OSSI signal approaching steady-state from full relaxation ($M_0 = [0, 0, 1]$), displaying how an oscillation structure is quickly formed then slowly scaled to the steady-state. Simulation parameters were set as $n_c = 10$, TR=15ms, TE=2ms, T1=1331 ms, T2=80 ms.

We can define how fast an isochromat reaches steady-state by $\mathrm{TR}_{\mathrm{SS}}$, the number

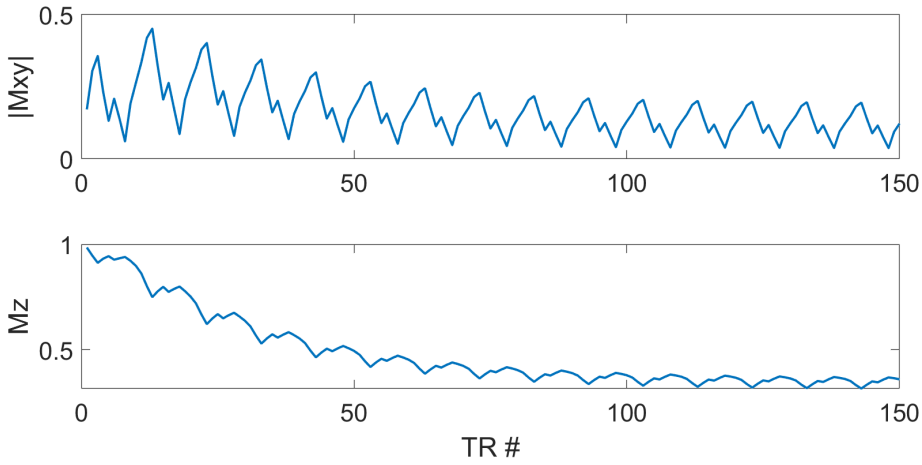

Figure 6.1: Simulated OSSI steady-state formation for B0=0 Hz with transverse magnitude and longitudinal signals plotted. $M_0 = [0, 0, 1]$.

of TRs required for the magnitude and phase of the signal to be within 1% of the steady-state value. For example, the signal in Fig. 6.1 is considered at steady-state after 159 TRs.

Our preliminary work shows that off-resonance affects steady-state formation time. An example of this is shown in Figure 6.2, plotting TR_{SS} as a function of off-resonance. All signals must reach steady-state before imaging can occur, so the effective steady-state formation time is dictated by the maximum of all off-resonant cases (ex. 217 TRs in Fig. 6.2).

A simple "scaling" catalyzation method is to scale the initial Mz component, such that spins are initialized at $M_0 = [0, 0, Mz]$ with $Mz \in [-1, 1]$. Scaling Mz can be accomplished using inversions or through an excitation followed by a crusher gradient. The results of a proof-of-concept simulation is shown in Figure 6.3, where the maximum time to steady-state was calculated for a range of initial Mz values.

We found that an initial value of $Mz = 0.45$ was optimal for the sequence parameters tested, reaching steady-state in 138 TRs, 36.4% faster than $Mz = 1$. The time required to reach steady-state was reduced from 3.25 seconds to 2.07 seconds.

This proof-of-concept simulation shows that even a simple catalyzation scheme

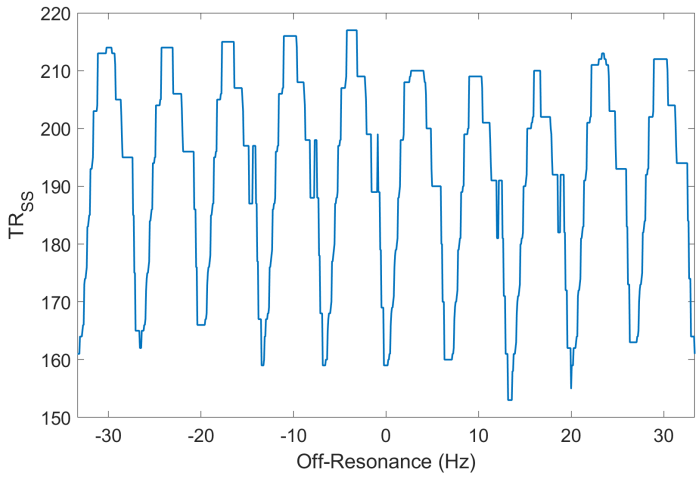

Figure 6.2: Number of TRs to establish steady-state as a function of off-resonance from $M_0 = [0, 0, 1]$. Signals were considered steady state when within 1% of steady-steady state magnitude and phase.

can accelerate OSSI steady-state formation. *Further investigation is needed to determine an optimal OSSI catalyzation sequence and if catalyzation will enable the use of preparation pulses.*

6.2 Alternative OSSI Signal Combination Approaches

Chapter III describes how each of the phases in the OSSI cycle can be considered to be separate acquisitions, each with their own frequency response. This concept is later explored in Chapter IV in the OSSCOR strategy, where each phase time course is modeled as a linear combination of functional signal change and physiological artifacts (Eq. 4.4). This model implicitly describes that phase timecourses for a voxel can have a varying amount of functional sensitivity. The physical reason for this arises from the fact that the frequency response for each OSSI phase is only T2* sensitive in regions of steep phase change. An example frequency response is shown in Figure 5.2, with the phase plotted in orange. Steep regions of the response will exhibit higher T2* sensitivity (ex. 0 Hz), whereas flat regions will exhibit little to no T2* sensitivity (ex. 11 Hz).

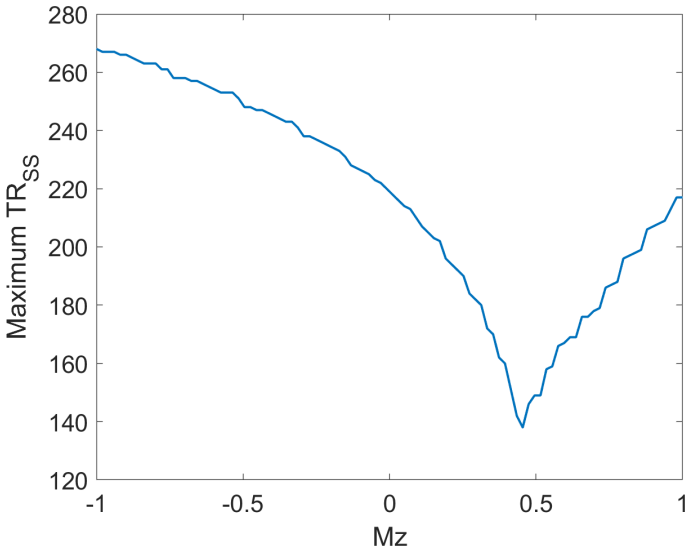

Figure 6.3: Maximum number of TRs to steady-state vs initial Mz. An initial value of Mz=0.45 was found to reach steady-state in 138 TRs, compared to Mz=1 which took 217.

An example of the varying T2* sensitivity is shown in Figure 6.4, which plots all phase timecourses ($n_c = 6$) for a single activated voxel. Varying amounts of activation changes can be seen in each phase timecourses. For example, the dark blue phase timecourse shows activation over the entire run, while the green timecourse shows practically no activation. Additionally, scanner drift results in slow changes to off-resonance over the duration of the run, changing the frequency sensitivity and amplitude of respiration artifacts. This is most notable in the orange timecourse, which shows respiration artifacts that increase in amplitude over time.

The OSSCOR method attempts to remove the physiological artifacts from each of the n_c phase timecourses, such that only functional changes and thermal noise remain. The cleaned phase timecourses are then combined using the 2-norm into a single timecourse which is used in a functional analysis. While the 2-norm is a simple and effective combination strategy that is robust to frequency offsets, it does not account for the differing functional sensitivity between phase timecourses or that the functional sensitivity may change over time.

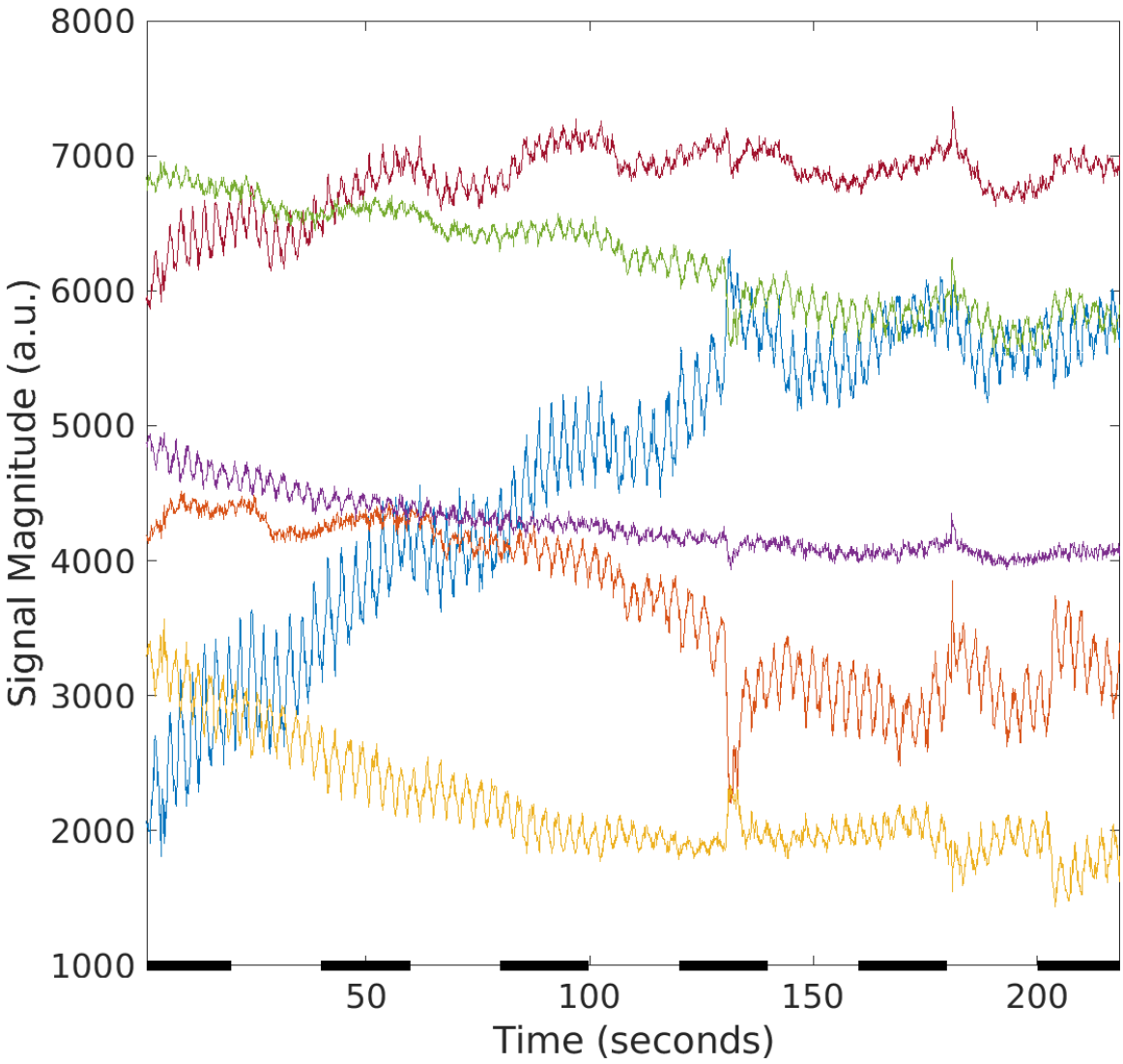

Figure 6.4: All 6 phase timecourses plotted for an activated voxel, showing differing amounts of functional activation and respiration/drift artifacts. Black bars indicate task periods.

Lastly, the 2-norm combination strategy adds an additional layer of complexity for fMRI statistical analysis. fMRI analysis commonly expresses a signal timecourse as a linear combination of activation-related change (task) and artifactual changes (nuisance), where degrees of freedom can be calculated. However, OSSCOR performs denoising on each phase timecourse separately prior to the 2-norm combination. Since this combination step is non-linear, it is not immediately obvious how to calculate degrees of freedom for an analysis of the combined OSSI signal if the data is denoised/detrended prior to combination.

In summary, future improvements to the OSSI signal combination strategy are needed that account for changing phase timecourse T2 sensitivity. An improved understanding of how OSSI signal combination affects statistical degrees of freedom is also needed for any future application in fMRI.*

6.3 Further Work on F-OSSCOR Correction Methods

Chapter III presented F-OSSCOR, a variation of the OSSCOR strategy that derives nuisance regressors from FID signals. Our analysis showed that increasing the number of principal components in F-OSSCOR did not increase the number of suspected false activations, whereas increasing the number of principal components in OSSCOR did (Figure 4.6). This is likely because magnitude changes in the FID signal are dominated by bulk respiration changes, "washing out" small functional changes in the principal component analysis.

An additional advantage of the F-OSSCOR method is that FID signals can be sampled every TR, resulting in "fully sampled" nuisance regressors regardless of the subsequent k-space trajectory. This may be useful for high-resolution 3D acquisitions where the volume TR may exceed 1 second or more. However, it is not immediately clear how to reconcile the FID and volume sampling rates into a single correction method. Furthermore, current OSSCOR and F-OSSCOR methods only use signal

magnitude, while per-shot correction methods would need to be performed on complex k-space data. *Further work is needed to determine how FID signals can be used to perform physiological correction in 3D multishot acquisitions.*

6.4 Further Work on Prospective Correction of Physiological Noise

Chapter V presents a real-time method that corrects for respiration induced B0 changes. The described method uses an open-loop control system to proportionally adjust a constant RF phase increment using FID phase measurements. Simulation and experimental results showed that this approach could improve signal stability even when the effects of respiration spatially vary.

The OSSI steady-state is not compatible with a 2D multi-slice approach since excitation must be performed every TR for all imaged areas. Therefore, a 3D acquisition strategy must eventually be used for any practical fMRI experiment. A 3D acquisition would present additional challenges for our real-time prospective correction method. First, our method calculates relative phase changes per coil, then performs coil combination to obtain one phase estimate. A 3D acquisition would result in each coil detecting a larger volume of signals with varying amounts of respiration-induced frequency changes. *Further investigation is needed to determine if FID-based frequency tracking is compatible with 3D volume acquisitions.*

Another challenge is that our system is only able to compensate for uniform frequency changes, whereas the effects of respiration are known to spatially vary throughout the brain, albeit smoothly. While our system demonstrated robust tracking for partially oblique slices, we observed that tracking did not work well for slices planned greater than approximately 30 degrees off of the axial plane. It is likely that a 3D acquisition would exacerbate this issue where an even greater amount of variation in

respiration effects would occur.

Previous work showed that linear spatial corrections are an effective method to correct whole-brain respiration effects [58], however, a significant hurdle in performing spatially varying B0 correction would be the 3D estimation of B0 changes in the first place. The FID-based method proposed proposed in V compresses all coils into a single estimate of uniform B0 changes across the slice. However, an FID-based method could potentially be used to estimate spatial B0 changes by utilizing a 3D coil sensitivity map. In this way, the FID signal measured from each coil could be used to create coarse 3D measurements of relative field changes, which would then be used to update 1st order shims or gradient blips in real-time. *Further investigation is needed to assess the use of a spatially varying B0 measurement and compensation strategy for OSSI.*

APPENDICES

APPENDIX A

Implementation of Real-time OSSI using RTHawk

Experimental Guide for the RTHawk Real-Time Correction Application

This appendix provides a brief guide for conducting an fMRI experiment with prospective B0 correction using RTHawk at the University of Michigan fMRI Lab. Additional technical details are also included on how this method was implemented, though the direct source code cannot be made public since RTHawk is proprietary technology of HeartVista, inc. and is being used under a research agreement.

Overview of the RTHawk System

RTHawk is a software system that allows sophisticated real-time control of the GE MR750 system. The primary RTHawk application runs on an external server which is directly connected to the GE scanner network. The RTHawk server then receives raw data from the scanner host and can change parameters in real-time. Parameters can be updated as rapidly as every TR.

Figure A.1 shows a process diagram of the prospective B0 correction application. Raw k-space data is first sent from the scanner to the RTHawk server as soon as it

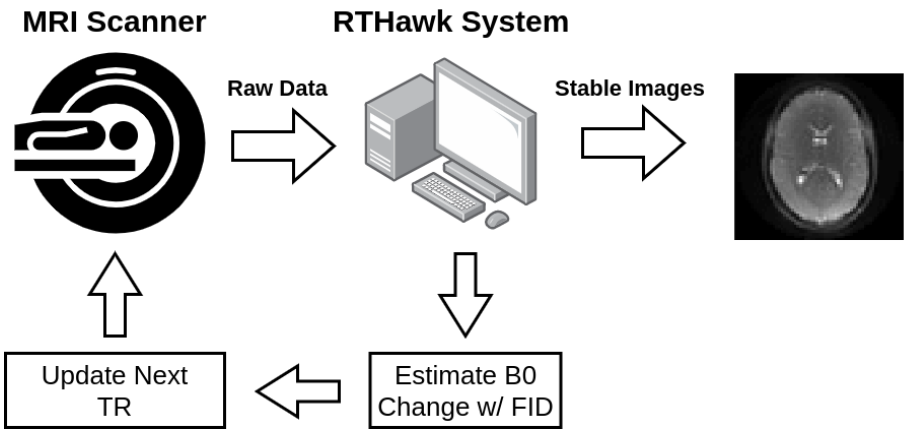

Figure A.1: Process diagram for the real-time control system.

is available after each TR. The RTHawk system then passes the raw data through the reconstruction pipeline. The reconstruction pipeline can then choose to update sequence parameters which are made effective in the next TR. In this case, relative phase information is calculated from FID data for one TR in every OSSI cycle. The FID data is then used to adjust the constant phase increment variable used in the RF phase calculation. The RTHawk system specifies the RF phase to the scanner every TR, though the phase increment variable is updated as soon as the FID calculation is finished (once per OSSI cycle).

Running an OSSI fMRI Experiment with Prospective B0 Tracking

Starting the session

The first step is to load a protocol and start an exam on the GE scanner interface. Any protocol can be selected with any coil as the RTHawk software will automatically add its own sequence to the protocol. If performing a human subject scan, enter the subject ID and weight here.

All subsequent user interaction takes place on the RTHawk server after the exam is started. The RTHawk application does not work over X11 forwarding, requiring the use of another remote desktop solution. We use the NoMachine remote desktop

service which was found to stream high quality 60 FPS desktop capture over a local network.

After connecting to the RTHawk server via NoMachine, the server must be connected to the scanner network. The RTHawk server has two network interfaces: one connected to the scanner network (`eno1`), and the other to the university network (`eno2`). Turn on the `eno1` interface, which is usually disabled for security purposes.

Now launch the RTHawk application either through the launcher icon or through the terminal command `RTHawk`. If the application does not start, ensure that the network interface has been enabled. The protocol selection screen will appear, as shown in Figure A.2. Select the OSS protocol. The connected coil should automatically be selected. If it isn't, select the desired coil from the coil selection dropdown menu.

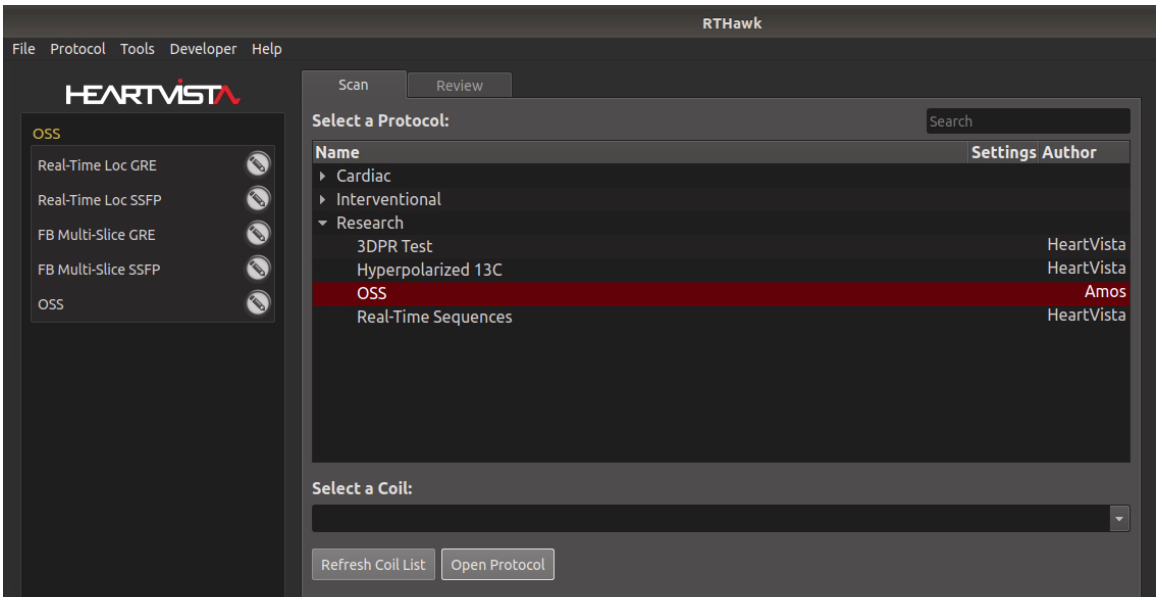

Figure A.2: The RTHawk protocol selection screen.

Select "Open Protocol." The patient dialog box will appear, confirming the patient ID, DOB, and weight, that was read from the exam information (Figure A.3). If this step fails, check that an exam was loaded on the scanner host computer. Confirm that this information is correct, then select the "Confirm" button to proceed. The

system is now ready to scan.

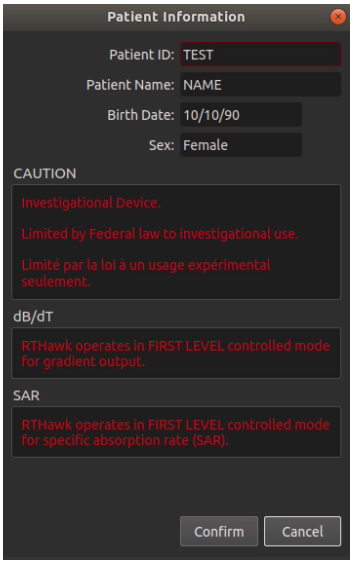

Figure A.3: The RTHawk patient information dialog box.

Running the OSSI Application

The scan location must first be localized. Several localization applications have been included in the "OSS" protocol:

- **Real-Time Loc GRE:** a real-time spoiled GRE sequence.
- **Real-Time Loc SSFP:** a real-time bSSFP sequence.
- **FB Multi-Slice GRE:** a free breathing multi-slice spoiled GRE sequence.
- **FB Multi-Slice SSFP:** a free breathing multi-slice bSSFP sequence.

Each application can be run by pressing the "play" button next to its entry in the Application list, as shown in Figure A.4.

The GRE and SSFP applications can be used to visualize T1 and T2 contrast, respectively. Because all of these sequences use fast spiral trajectories, take care not to plan slices that are tilted significantly away from the axial plane as PNS is likely

Figure A.4: The OSS protocol application list

to result. Select the OSS application and place the slice over the desired anatomy. Double-click the slice to start the OSS application in real-time mode. For more information on slice planning, please see the RTHawk information guide.

The OSSI scan control UI will appear at the bottom of the RTHawk interface, shown in Figure A.5. All parameters can be changed dynamically and will immediately updated in the next TR.

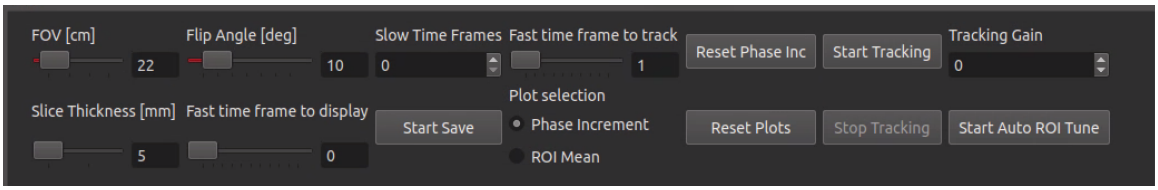

Figure A.5: The OSS application parameter selection UI.

Enabling Real-Time B0 Tracking

The OSS application shows the 2-norm combined image in the display window by default, selected as position 0 in the "Fast time frame to display." Other images in the OSSI cycle can be displayed by adjusting this slider.

Select the "ROI mean" radio selection button to display the mean ROI timecourse in the left plot window. Then, select the bottom ROI tool and position the ROI over the anatomy of interest in order to visualize the tracking effectiveness. As the scan runs, the left window will show the mean ROI magnitude, and the right window

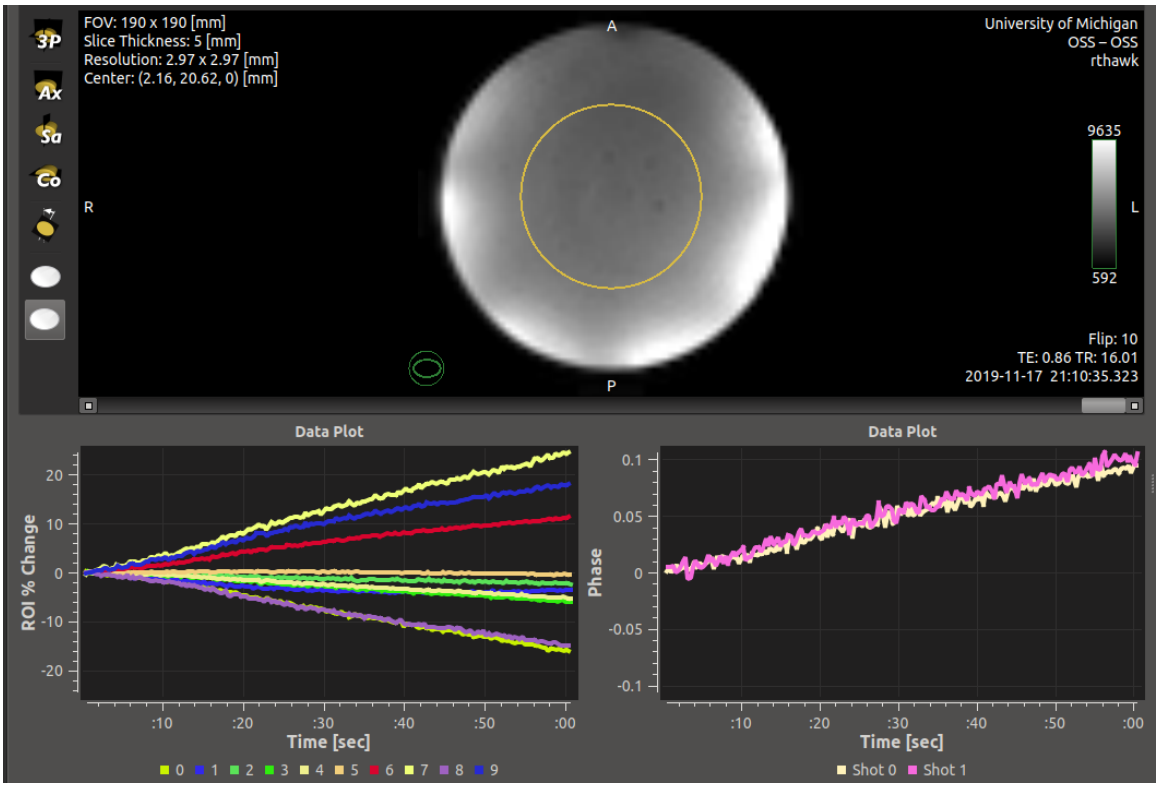

Figure A.6: Screenshot of the OSSI application built in RTHawk. The top pane shows the combined OSSI image in real-time, as well as the user specified ROI in yellow. The bottom left pane shows the mean signal percent change within the ROI for each of the OSSI phases, with tracking off. The bottom right pane shows the FID phase measurement timecourse for each shot.

will show the FID phase measurements. An example of a selected ROI and the plot windows is shown in Figure A.6, showing data after 60 seconds of scan time.

Tracking can now be enabled by clicking on the "Start Tracking" button on the right side of the parameter panel. The "Tracking Gain" value (referred to as c in Chapter V) can be manually set, or automatically calibrated using the "Start Auto ROI Tune" button. Automatic calibration can take up to 2 minutes to complete. As tracking improves, signal variance in the "ROI % Change plot" will decrease. When tracking is working well, the signal will vary less than 2%. If automatic calibration fails, try manual adjustments until satisfactory ROI signal variance is achieved.

Saving Data

Images can be saved directly to a MATLAB `*.mat` file using the "Slow Time Frames" parameter box, which will save the specified number of OSSI cycles (n_c frames). Image saving can be performed with or without tracking enabled. Increasing the number of slow time frames will update the estimated scan time in the bottom left notification box. Press the "Start Save" when you are ready to start recording data. Triggering is not implemented in the OSS application, so any fMRI stimulus must be manually synchronized with the "Start Save" button press. After saving is started, the estimated number of time left is shown in the notification area. The scan will not stop after saving is complete, and must be stopped manually in the application list (Fig. A.4).

Ending the Session

After the scan is complete, close the RTHawk exam by clicking the red "Close Protocol" button on top of the application list. Disable the `eno1` network interface. End the exam on the scanner host computer. No RTHawk data is saved to the scanner host, so it is not necessary to clear off any files after scanning.

APPENDIX B

Contributions to Pre-Clinical Imaging Methodology

Introduction

Though cardiovascular disease remains the leading cause of death globally, the pathogenesis of some of the most common vascular diseases can be described by a single method of action: the stenosis or occlusion of blood vessels [88]. Regardless of occlusion in the heart, brain, or peripheral vasculature, the fundamental problem involves a reduction of blood conductance which impedes the normal healthy function of arterial supply or venous return. Because of this, the mechanism by which the body responds in order to compensate is also the same, de novo vessel growth and the enlargement of small pre-existing vessels [89][90][91][92]. The former, termed angiogenesis, is critical for acute tissue survival and involves formation or splitting of capillaries. The latter, termed arteriogenesis, involves the adaptive growth of a collateral blood vessel and is mandatory for long term functional restoration. While the term arteriogenesis describes the formation of a collateral artery due to blockage, veins are equally capable of collateralizing. Although the substances constituting

these blockages may differ—ex. arterial plaques vs. venous thrombi—the process of vessel collateralization allow for increased conductance and restoration of flow in both arteries and veins.

Peripheral artery disease, or PAD, is one of such conditions which results in arteriogenesis [93]. Similar to coronary artery disease, PAD involves a narrowing of peripheral arteries, typically in the legs, resulting in tissue ischemia and intermittent claudication. The femoral artery ligation model in mice has been extensively used as a model of peripheral artery disease in order to study the fundamental physiological response to an arterial ischemic event, as well as study potential therapeutic targets [94][95][96][97][98]. This model is significant due to its ability to produce both the growth factors involved in angio-/arterio-genesis, as well as reproducibly cause structural changes to the arterial network through the formation of collateral vessels. The collateral vessels in this model, however, have been visualized with limited success in-vivo, as the collateral vessels that form are both small during formation and within deep tissue, making imaging difficult.

Despite most literature focusing on the formation of collateral arteries through arteriogenesis, veins are equally capable of collateralization in response to stenosis or occlusion, which we refer to as venogenesis herein [99]. In humans, the most common cause of such venous blockages is in the form of deep vein thrombosis, or DVT. This condition affects approximately 300,000-600,000 people in the United States each year and presents a 33% mortality rate [100]. DVT is difficult to study due to an inability to safely obtain human biopsy samples at the thrombus-vein wall interface, which has resulted in the development of a variety of venous thrombosis animal models [101].

Imaging is an essential tool to visualize and explore blood vessels in mice, however, imaging of collateral arteries in-vivo has been limited. High-resolution x-ray computed tomography approaches rely on perfusion of a sacrificed animal with contrast agent, and is unable to capture in-vivo changes over time of an intact disease model. MRI, a

choice modality to study physiological systems in-vivo, has been limited to only partial visualization of arteries due to both small vessel size, as well as lower volumetric flow rate in collateral vessels, at least initially, compared to larger healthy arteries. MRI contrast enhancement techniques utilizing a bolus of gadolinium chelates combined with first pass imaging are commonly used for small vessel enhancement in humans, however, such strategies are not achievable in mice as administered contrast agents rapidly perfuse through tissue, resulting in an inability to temporally separate the arterial pass from the venous pass of the contrast agent. While partial visualization of collateral arteries has been accomplished using MRI time-of-flight imaging, previous work has not demonstrated in-vivo visualization of collateral veins in mice, despite knowledge of their existence. Subsequently, this inability to visualize the complete extent of collateral vasculature in-vivo presents an unknown in the use of pre-clinical animal models of vascular insufficiency, as the exact nature of how obstructions are naturally resolved cannot be non-invasively monitored in its entirety. Therefore, a technical need exists to better non-invasively monitor the structural progression of arterio-/veno-genesis in mouse models of vascular occlusion. Addressing this need will result in better understanding of fundamental structural changes in murine models of vascular obstruction, and to be able to derive metrics and monitor outcomes for testing vascular therapies.

In this appendix, we present an optimization of the multiple overlapping thin slab angiography (MOTSA) method [102] to visualize small arteries and veins, beyond what is achievable using single-acqusition time-of-flight MRI angiography methods. Using this method, we also present visualizations of collateral vessels within murine models of peripheral artery disease and venous thrombosis, demonstrating an ability to non-invasively monitor endpoints in mouse models of both arterial and venous occlusion.

Methods

All experiments were performed with local Institutional Animal Care and Use Committee approval. 10-14 weeks old male C57BL/6 mice were used. Imaging was performed at 7 Tesla (Agilent; Palo Alto, CA) using a 40 mm inner diameter transmit-receive radio frequency (RF) volume coil (Morris Instruments; Ontario, Canada), with mice placed in a supine position. Animals were anesthetized and maintained on 1.5–2% isoflurane in 1 L/min of oxygen. Respiration was monitored while body temperature was maintained at 37 ± 0.3°C using warmed air and a closed loop proportional-integral-derivative controller integrated with a commercially available monitoring system (SA Instruments Inc., Stony Brook, NY).

Imaging Parameter Optimization

Collateral vessels can exhibit both curvature and tortuosity. Therefore, isometric resolution was set a priori as a primary goal for the basis of each "thin slab" of the MOTSA implementation to improve the chances of resolving an arterial or venous collateral vessel in any anatomical plane in which it developed. Secondarily, we sought to reduce saturation effects and minimize cranial-caudal wrap around while optimizing for small vessel conspicuity along the cranial-caudal direction of flow (the direction of flow anticipated for newly formed collaterals). Therefore, the field of view (FOV) or thin slab, matrix size, and RF excitation thickness were qualitatively optimized first, using 3D time-of-flight gradient echo acquisitions (3D-TOF) centered on the iliac vessels which were visualized initially using a 2D gradient echo coronal acquisition. Starting values for the 3D-TOF datasets were chosen based on previous work performed at 4.7 T (TR=15 ms, TE=2.6 ms, FA=20°, FOV=$(30x30x15\text{mm})^3$, matrix $128x128x64$ zero-filled to 256x256x128, NEX=1) [96]. The RF excitation thickness (RF_{thk}) was varied from 20-100% of the total slab FOV, with the goal of optimizing small vessel conspicuity while minimizing total imaging time for a complete

volume.

Quantitative optimizations of TR and FA, two of the most influential parameters in determining the contrast-to-noise ratio (CNR) of blood vessels in TOF MRA, were performed using the optimized resolution and RF excitation thickness. The tail artery was chosen for this work because its diameter ($\sim$350 µm) is comparable to previously reported peripheral arterial collateral vessel measurements (318 $\pm$ 30 µm) [103]. Additionally, the tail artery can be easily aligned and secured relative to the imaging volume to provide uniaxial flow in the same primary anatomical direction as expected in newly formed collaterals (i.e. cranial-caudal). 3D-TOF datasets of the tail artery were acquired while varying TR from 10 to 50 ms in 5-10 ms increments, while holding FA constant at 20°. Flip angle was then optimized in a similar manner. Holding TR constant at 30 ms, FA was varied from 10° to 90° in 5° increments. Tail artery voxels were manually segmented from 2D axial slices derived from the 3D-TOF datasets acquired to optimize TR and FA. Because a region of interest (ROI) based CNR calculation, i.e., taking the average CNR over an ROI, is sensitive to under/over segmentation when there are a small number of voxels across the object of interest (10-14 voxels for the tail artery), the maximum contrast-to-noise ratio (CNR_{max}) was determined for each slice. The average CNR_{max} and 95% confidence interval (CI) was calculated from 55 axial slices (covering 7 mm of resolvable vessel) for each dataset acquired for TR or FA and compared across TR or FA values. An ANOVA test was first used to test differences among CNR_{max} means. Then, the mean CNR_{max} values for successive TRs (10 ms vs 15 ms, 15 ms vs 20 ms, etc.) were tested for differences using a pairwise t-test with pooled standard deviation and Bonferroni correction ($\alpha = 0.05$). A pairwise test was chosen as it allowed pairwise comparison of CNR_{max} values from the same slice location. Results from varying FAs were evaluated by measuring the number of CNR_{max} values which were above the selected critical CNR value of 10 for visualization.

Reconstruction and Visualization of Composite MOTSA Volumes

Reconstruction of the final MOTSA volumes was performed using a MATLAB script developed in-house (Mathworks; Natick, MA). The full-width-half-maximum of the signal profile across the RF excitation thickness was evaluated to determine how much a thin slab could be advanced in the z-direction (cranial-caudal relative to the mouse), while also considering imaging time. Thin slabs were overlapped and aligned using the spatial coordinates of each dataset and merged into a single continuous 3D volume. In areas of overlap between two adjacent thin slabs, voxel pairs were evaluated individually and the highest intensity voxel was assigned to the final volume. Preliminary demonstration of the success of the thin slab merging algorithm was performed on central vasculature spanning the renal arteries. This region was selected for its complex vascular orientation and because the renal vessels have flow perpendicular to the RF excitation direction, which incurs the most TOF saturation effect. Reconstructed MOTSA volumes were visualized by partial and full maximum intensity projections (MIPs). Finally, MOTSA was performed using Gaussian and 3-, 5-, 7-, and 9-lobe sinc RF excitation pulse shapes to qualitatively evaluate their effects on image quality after volume merger.

Comparison of MOTSA to Single Thick-Slab 3D-TOF

The optimized MOTSA acquisition was compared to single thick-slab 3D-TOF acquisition with a gaussian slab excitation profile. A healthy mouse was used to acquire data from just proximal to the aortic bifurcation to distal of the saphenous-popliteal bifurcation. Using 46 axial slices from the 3D-TOF or MOTSA datasets, the right iliac artery was manually segmented from surrounding tissue. Additionally, the right iliac vein was segmented from the MOTSA dataset, but not from the 3D-TOF data because veins are not visible. Using 46 axial slices from the 3D-TOF or MOTSA datasets, the right iliac artery was manually segmented from surrounding

tissue. Additionally, the right iliac vein was segmented from the MOTSA dataset, but not from the comparison 3D-TOF data because veins were not visible. Average vessel CNR was calculated for each segmentation. The mean CNR along the ROI (averaging across all segmentations of a vessel) was then used to compare results between 3D-TOF and MOTSA.

Implementation of MOTSA in Surgical Models of Arterio-/Veno-genesis

Mice underwent femoral artery ligation (FAL) on the left side (n = 5) with a single 5/0 prolene ligature at the level of the inguinal ligament under general anesthesia (inhaled isoflurane 2–2.5% in 1 L/min air). The optimized MOTSA strategy was used to image peripheral hindlimb vasculature and visualize the development of collateral arteries (arteriogenesis) on days 3, 7, 14, 21, and 28 post-ligation. In a second model, venous thrombosis was induced in the infrarenal inferior vena cava (IVC) (n = 5) via the well-established ligation model [104]. Briefly, mice were anesthetized using 2% isoflurane in 1 L/min oxygen, a midline laparotomy was performed, the gastrointestinal tract was exteriorized and kept moist, a 5-0 prolene ligature was placed around the IVC immediately distal to the left renal vein, and any lateral or lumbar venous branches draining into the IVC between the left renal vein and iliac bifurcation were also ligated. The gastrointestinal tract was returned to the abdominal cavity, and the abdomen was closed in two layers (muscle with 7-0 vicryl, skin with veterinary glue). The described MOTSA strategy was used to image peripheral vasculature from just distal of the kidneys to distal of the saphenous-popliteal bifurcation and visualize the development of collateral veins on days 2, 6, 14, 21, and 28 post-ligation. Day 2 and 6 are considered acute and chronic timepoints in this model. A total of 13 thin-slabs were acquired per timepoint, starting centered on the left renal artery. The total acquisition volume was 30x30x54 mm, matrix of 256x256x461, isotropic resolution = 117 μm^3 and a total acquisition time of 53 minutes.

Data from the arterial and venous ligation models were assessed for evolution and variability of collateralization. The number of collateral arteries or veins visible on each dataset were counted by a single observer (A.C.), blinded to animal ID and timepoint, using coronal MIPs. To mitigate intra-user variability, counting was repeated a minimum of three times per dataset until the standard deviation of the measurements was less than one, with up to five attempts. The median value of each counting set was used as the final value for the number of collateral vessels visible within a given dataset. These metrics of collateralization were compared across timepoints within the same animal to observe temporal changes, as well as at each timepoint between animals to assess model variability.

Results

Thin slab, matrix size, and RF excitation thickness

Field of view in the S-I direction was set to 15 mm to promote small vessel visibility, with a FOV of 30x30 mm in the A-P and L-R directions. Both arteries and veins are visible at lower excitation thicknesses, though tracking distance is reduced. A slab thickness of 40% FOV (6 mm) was chosen because it qualitatively provided the best balance of: arterial and venous signal, a slab thickness that would minimize the total number of slabs needed to acquire anatomical data of interest (i.e. peripheral collateral vessels), and minimizing venetian blind artifacts due to signal saturation at the edge of the slabs. The tail artery was used for subsequent quantitative optimization of repetition time and flip angle.

Final FOV and matrix size were 30x30x15 mm and 128x128x64 zero-filled to 256x256x128, producing an isometric resolution of ($117\,\mu m^3$). RF excitation thickness for each thin slab was varied from 100% (15 mm) to 20% (3 mm) of the thin slab to assess visualization of small vessels. As expected, signals from both arterial and

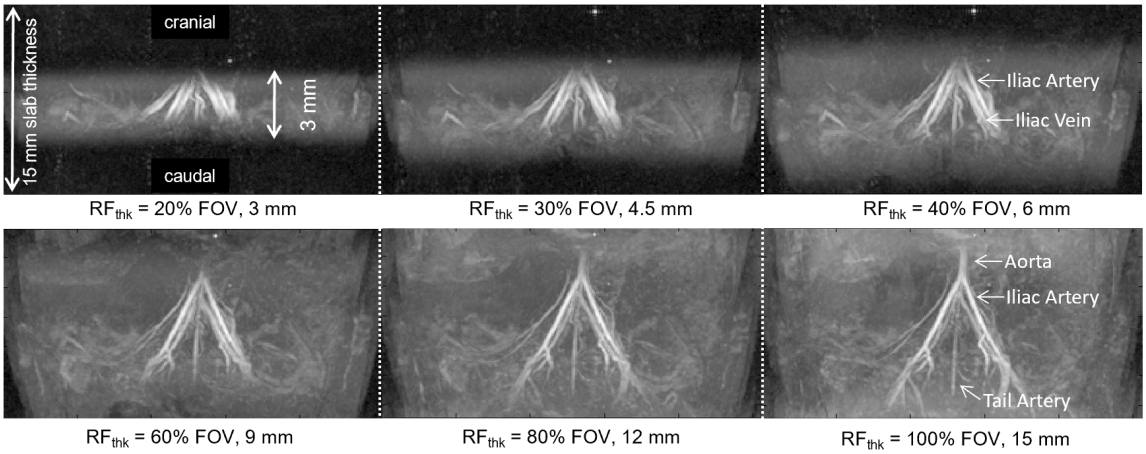

Figure B.1: Coronal maximum intensity projections (MIPs) from single slab 3D time-of-flight (TOF) acquisitions of murine iliac vessels. RF slab excitation thickness was varied from 20-100% FOV (3-15 mm) while slab thickness was held fixed. Both arteries and veins are visible at lower excitation thicknesses, though tracking distance is reduced.

venous flow were increased as RF excitation thickness was decreased (Figure B.1).

Reducing excitation thickness results in increased small-vessel sensitivity comes but also increased acquisition time, as thinner RF excitation thicknesses results in additional acquisitions needed to cover a given volume. Conversely, increasing RF excitation thickness reduces imaging time, but increases saturation effects at either end of the thin slab, resulting in negation of smaller artery and vein signal, and causing more apparent venetian blind artifacts after volume merger. A thickness of 6 mm (40% FOV) was selected as it was the maximum thickness in which the veins and arteries of similar size to peripheral arterial collateral vessels were still visible, while maintaining an acceptable number of total thin slabs needed to cover the anatomical region of interest.

Repetition Time and Flip Angle

Figure B.2a shows the resulting $\mathrm{CNR}_{\mathrm{max}}$ vs TR summary for acquired tail artery angiograms. A TR of 30 ms was chosen as it was the only parameter value that

provided statistically significant improvement as compared to 20, the previous value tested (95% mean confidence intervals of 23.3 ± 3.9 vs 19.5 ± 3.4, p = 0.003). As shown in the plot, a TR of 30 ms has nearly the same CNR_{max} inner quartile range as TR = 50 ms (26.4 ± 2.9), but can be acquired 40% faster.

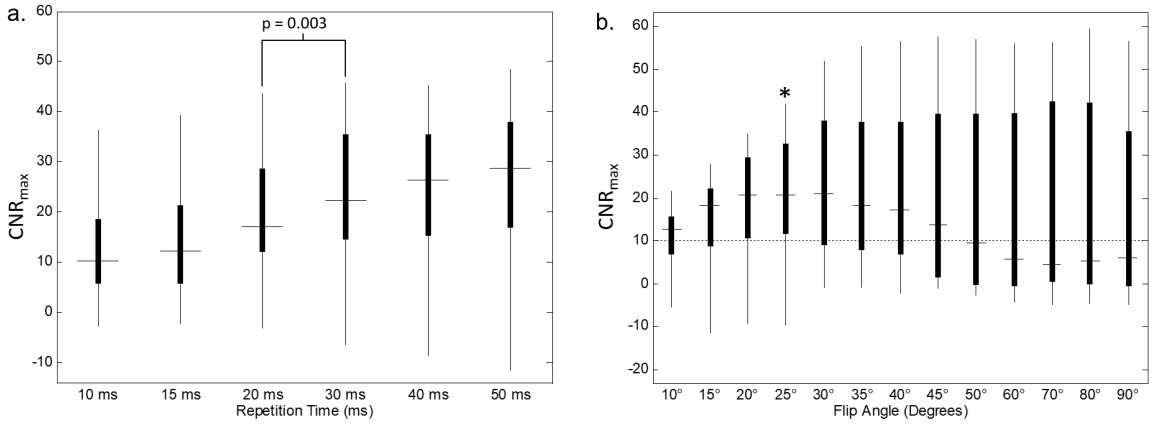

Figure B.2: Optimization results for TR and FA. Subplot a) shows CNR_{max} vs. TR for FA=20°. A TR of 30 ms was chosen as it was the only parameter value that provided statistically significant improvement as compared to the previous value tested (20 ms vs 30 ms, p = 0.003). Subplot b) shows box and whisker plots of the CNR_{max} vs FA. A flip angle of 25° was qualitatively chosen for the best CNR performance.

Flip angle was quantitatively optimized over the same anatomical region as TR, holding TR constant at 30 ms. As shown in Figure B.2b, higher flip angles result in a higher maximum CNR but a lower median CNR (horizontal marks) along the length of the vessel due to TOF saturation effects as blood passes through the volume. A final flip angle of 25° was qualitatively chosen because it had the greatest number of CNR_{max} measurements (78.2%) above a selected CNR value of 10, and nearly the highest median CNR.

Reconstruction of MOTSA Volumes and Comparison to Single Thick Slab 3D-TOF

Figure B.3 shows two adjacent thin slabs, with overlapping geometry marked with a dotted line. Because the full-width-half-maximum of the signal profile across the 6 mm RF excitation thickness was approximately 3 mm (40% FOV MIP in Fig B.1), thin slabs were advanced 3 mm at a time in the z-direction (cranial-caudal relative to the mouse), resulting in an approximately 50% overlap of the RF excitation thicknesses.

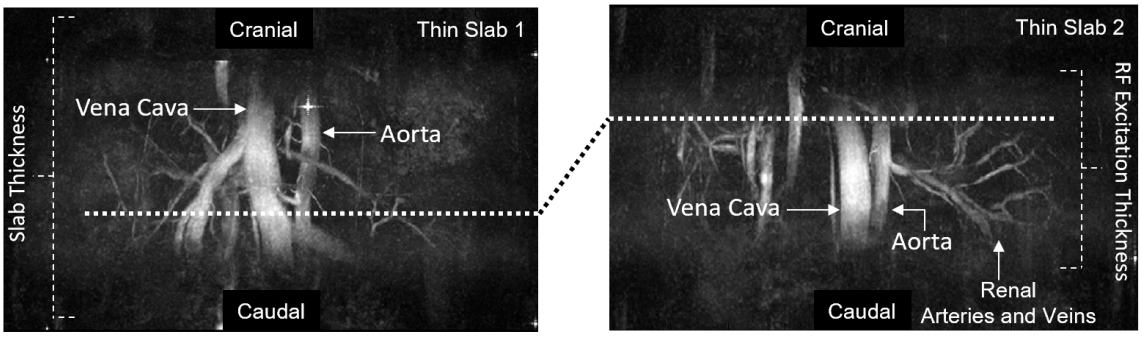

Figure B.3: Two successive multiple overlapping thin slab acquisition (MOTSA) slabs, with overlapping geometry denoted by the dotted line. Slab 1 and 2 are acquired with identical parameters, with the second positioned 3 mm distal to the first. Adjacent slabs are merged into a final volume using a voxel-by-voxel maximum signal selection strategy. In both acquisitions, small arteries and veins, such as the renal arterial and venous branches, are readily visualized.

Using the spatial coordinates of each slab resulted in accurate combination of thin slabs since the mouse was held secure in a holder, and adjacent volumes were acquired within 4 minutes of one another. Gaussian RF shapes provided the best merged volume quality based on smooth transitions of intensity between slabs. All sinc waveforms tested produced Gibbs artifacts which were visible in the final merged volume, significantly reducing conspicuity of small vasculature (data not shown).

MOTSA and 3D-TOF acquisitions of healthy peripheral mouse vasculature were

compared to quantify in vivo CNR improvements using the newly optimized parameter set. Figure B.4 shows coronal MIPs of MOTSA (a) compared to a single thick-slab 3D-TOF (b) of the murine peripheral vasculature starting at the iliac bifurcation. The calculated maximum vessel CNR values from each successive axial slice are shown in (c).

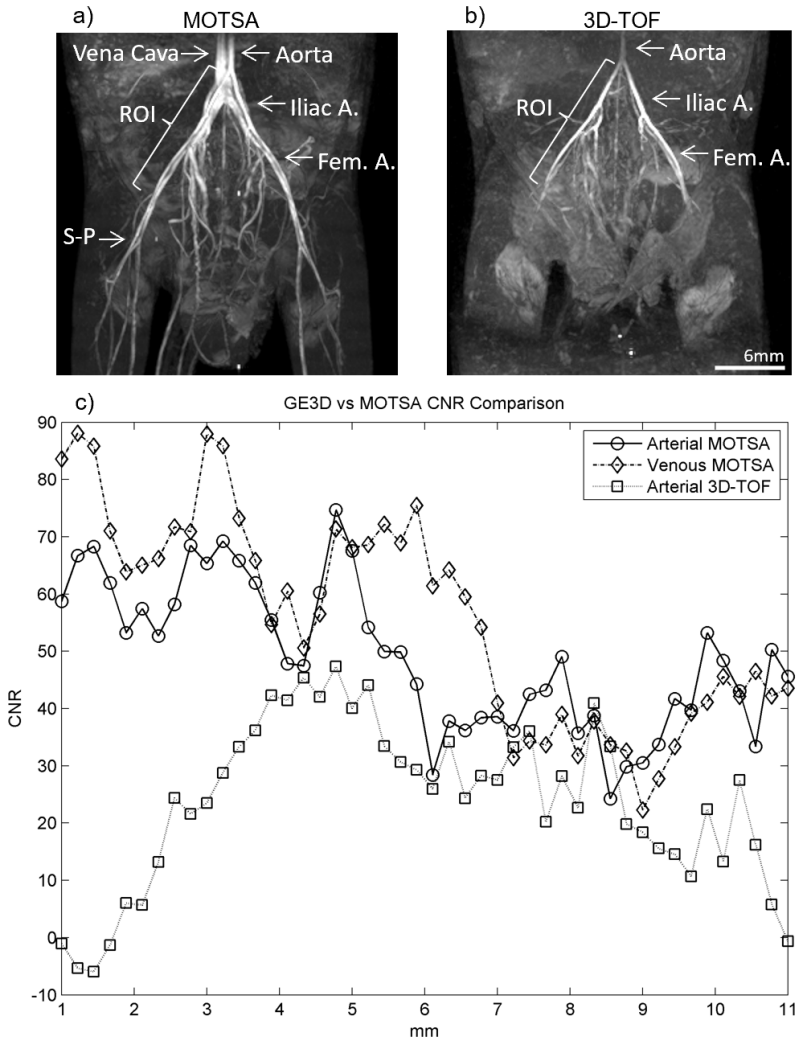

Figure B.4: Comparison of a) MOTSA and b) single thick slab 3D-TOF acquisition, with mean slice CNR shown in subplot c).

As expected, the 3D-TOF maximum CNR profile has an approximately Gaussian shape corresponding to its RF excitation profile. The mean CNR of the 3D-TOF profile was 23.8 ± 4.2 (95% CI). The MOTSA acquisition of the same vessel anatomy

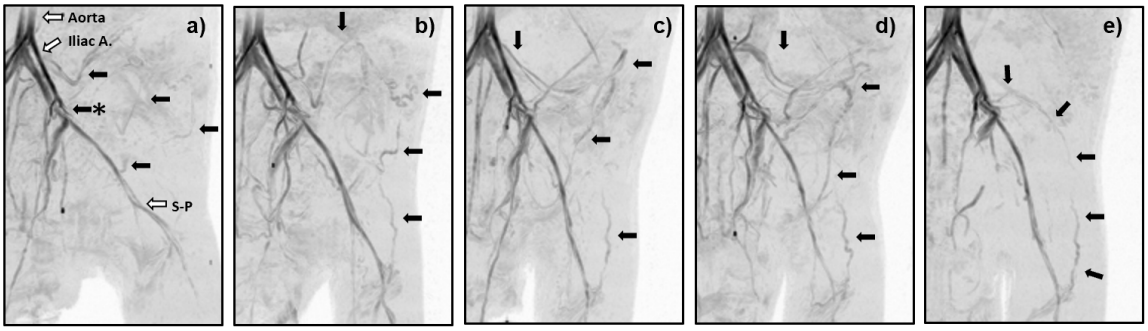

Figure B.5: Coronal partial MIPs from MOTSA acquisitions of mouse hindlimb vasculature after left femoral artery ligation on days (a) 3, (b) 7, (c) 14, (d) 21, and (e) 28. Ligation site is marked in (a) using an arrow with an asterisk. All images were acquired from the same mouse. Initial collateral formation (black arrows) is visible on day 3, with maximum number of collateral vessels visualized on days 14 and 21. Pruning of vessels occurs through day 28, when, typically, a single resolvable collateral artery extends from the ligation site to the popliteal artery. This collateral exhibits the characteristic corkscrew shape at the distal end of the vessel. MIPs have been inverted to improve vessel conspicuity.

demonstrates greater CNR at nearly all locations, with a mean CNR of 49 ± 3.8 (95% CI). Additionally, mean CNR of the iliac vein was quantifiable from the MOTSA and exhibited a similar CNR profile to the iliac artery (mean 55.3 ± 5.4 (95% CI)). The CNR of the iliac vein could not be measured from the 3D-TOF as veins were not visible.

Final parameters for MOTSA were empirically defined as: TR/TE 30/2.84 ms, flip angle 25°, FOV (slab thickness) 30x30x15 mm, matrix 128x128x64 zero-filled to 256x256x128, isotropic resolution = 117 μm^3, RF excitation thickness 6 mm (40% of FOV), slab spacing 3 mm, with a Gaussian RF-excitation profile (width = 1 ms), BW = 100 kHz, and NEX = 1.

Visualizing and Quantifying Arterial Collateralization Using MOTSA

An illustrative MOTSA time series visualizing development and adaptation of collateral arteries in a single mouse over a 28 day period is displayed in Figure B.5.

Ten thin slab 3D volumes were acquired, starting 2 mm proximal to the aortic bifurcation, with a total acquisition volume of 30x30x42 mm, matrix of 256x256x358, isotropic resolution = 117 μm^3, and a total acquisition time of 41 minutes. This time series from the same mouse depicts a successful left iliac artery ligation, followed by arterial collateralization (arteriogenesis), with collateral vessels forming and then pruning through day 21. On day 28, a single collateral vessel exists which exhibits a typical corkscrew shape on the distal end, extending from the femoral ligation site to the popliteal artery. In all animals, arterial collateralization is visible on day 3. The number of collateral vessels observed in each animal increased to a maximum on day 14 or 21. On day 28, the number of collateral vessels visible is typically reduced to 1-2 primary pathways, consistently demonstrating a corkscrew shape at their distal ends.

Visualizing and Quantifying Venous Collateralization Using MOTSA

An example MOTSA time series visualizing the development and adaptation of collateral veins in two mice over a 28 day period is displayed in Figure B.6. These time series depict successful IVC ligations, followed by different venous collateralization patterns visible as early as day 3.

Compared to the femoral artery ligation model, the maximum number of collateral veins was achieved on day 6, with pruning occurring through 28. As noted during surgery, mouse 1 had no side branches and on day 28 exhibits two collateral veins bilaterally. Lack of side branches, one of four anatomical patterns documented in C57BL/6 mice [101], was found in three other mice, along with a similar day 28 collateral pattern. Conversely, mouse 2 had a single right side branch (ligated during surgery), the most common phenotype, and on day 28 exhibits two veins that occur unilaterally on the left side.

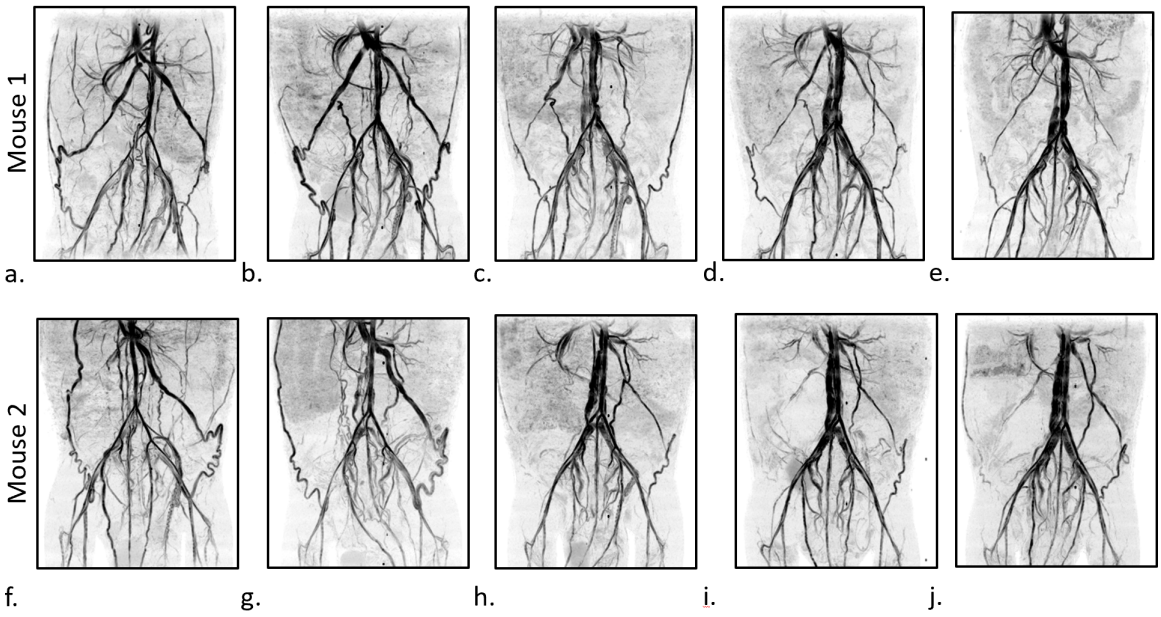

Figure B.6: Coronal MIPs from MOTSA acquisitions of mouse vasculature from just distal of the kidneys to distal of the saphenous-popliteal bifurcation after inferior vena cava (IVC) ligation on days (a,f) 2, (b,g) 6, (c,h) 14, (d,i) 21, and (e,j) 28.

Discussion

This study shows that a quantitative parameter optimization combined with a reduction in slab thickness results in a robust ability to visualize collateral vessels in both an arterial and venous model of occlusion. The sensitivity of this method is reflected by being able to visualize networks of small tortuous collateral arteries and veins, vessels which are small in diameter and have low blood velocity, respectively. While small and low flow vessels typically do not produce enough signal to be visualized in a thick slab 3D-TOF, the optimized parameter set tested was able to track the changes in both arterial and venous networks over time within the same animals.

MOTSA can be used to visualize the variability of collateral vessels. The data acquired in the present study as well as past research suggests that while many collateral arteries initially adapt to increased flow in the hindlimb ischemia model, blood

flow eventually converges to a single dominant vessel. This vessel has reliably morphology which can be visualized with MOTSA: the collateral begins just above the ligation site at the iliac artery and progresses distally, reconnecting at the popliteal artery. Corroborated by other observations, this final collateral artery also typically assumes a corkscrew shape towards its distal end. This is in contrast to the IVC ligation model, which has very high variation in initial and final collateral states between animals. In our preliminary results, this difference in venous collateral development is dependent on initial vessel phenotype. As characterized by Diaz et al, C57BL/6 mice IVC branches exhibit one of four different anatomical patterns. Four mice out of five in the group had no side branches, and developed bilateral venous collaterals. The last mouse had one side branch which was interrupted, which resulted in unilateral development of a collateral vessel. Given the unique ability to visualize collateral veins using our MOTSA protocol, it is now possible to explore the collateral vessel outcome associated with an IVC branch variation.

The acquired MOTSA data demonstrates that a thin slab improves contrast by mitigating time of flight dependent signal losses. By dividing the thickness and matrix size of the slab in half (15mm, res=64) compared to the in-plane FOV ($30mm^2$), res=128^2), blood typically remains in the slab for a smaller amount of time compared to a thicker slab of equivalent TR while maintaining isometric voxel size. This not only improves the mean contrast of the vessel, but also results in a smoother signal intensity profile along a vessel by mitigating the gradual signal drop along a longer comparative slab. This thin slab strategy also increases the sensitivity to small vessels that flow orthogonal to the excitation direction (vessels that travel in the axial plane), through the same mechanism of reducing blood transit time through the slab. Additionally, setting the voxel size isometrically results in the ability to resolve a vessel spatially regardless of which logical axis it resides on, further improving the ability to resolve tortuous or non cranial-caudal oriented vessels.

A limitation of our method is that it is difficult to quantify the smallest detectable vessel, since vessel signal is dependent on size, volumetric flow, direction of flow, and non-laminar/turbulent effects. Due to restrictions on how long mice could be anesthetized, the smallest achievable isometric voxel resolution was 100 µm for large extents (about 12 slabs), and 50 µm for smaller extents (about 4 slabs).

Conclusion

This appendix describes a high resolution MOTSA protocol capable of imaging small, low velocity vessels in both healthy mice and models of arterial and venous occlusion. This method is able to consistently detect morphological changes in collateral arteries and veins over time, which now enables the ability to reliably and longitudinally visualize changes in mouse models of vascular occlusion.

BIBLIOGRAPHY

[1] Ogawa S, Lee T, Nayak AS, Glynn P. Oxygenation-sensitive contrast in magnetic resonance image of rodent brain at high magnetic fields. Magnetic Resonance in Medicine 1990;14:68–78.

[2] Belliveau JW, Kennedy DN, McKinstry RC, Buchbinder BR, Weisskoff RM, Cohen MS, Vevea JM, Brady TJ, Rosen BR. Functional mapping of the human visual cortex by magnetic resonance imaging. Science 1991;254:716–719.

[3] Ogawa S, Tank DW, Menon R, Ellermann JM, Kim SG, Merkle H, Ugurbil K. Intrinsic signal changes accompanying sensory stimulation: Functional brain mapping with magnetic resonance imaging. Proceedings of the National Academy of Sciences of the United States of America 1992;89:5951–5955.

[4] Mansfield P. Multi-planar image formation using NMR spin echoes. Journal of Physics C: Solid State Physics 1977;10.

[5] Glover GH. Spiral imaging in fMRI 2012. doi: 10.1016/j.neuroimage.2011.10.039.

[6] Larkman DJ, Hajnal JV, Herlihy AH, Coutts GA, Young IR, Ehnholm G. Use of multicoil arrays for separation of signal from multiple slices simultaneously excited. Journal of Magnetic Resonance Imaging 2001;13:313–317.

[7] Pruessmann KP, Weiger M, Scheidegger MB, Boesiger P. SENSE: Sensitivity encoding for fast MRI. Magnetic Resonance in Medicine 1999;42:952–962.

[8] Sodickson DK, Griswold MA, Jakob PM. SMASH imaging. Magnetic resonance imaging clinics of North America 1999;7:237–54.

[9] Griswold MA, Jakob PM, Heidemann RM, Nittka M, Jellus V, Wang J, Kiefer B, Haase A. Generalized Autocalibrating Partially Parallel Acquisitions (GRAPPA). Magnetic Resonance in Medicine 2002;47:1202–1210.

[10] Feinberg DA, Moeller S, Smith SM, Auerbach E, Ramanna S, Glasser MF, Miller KL, Ugurbil K, Yacoub E. Multiplexed Echo Planar Imaging for Sub-Second Whole Brain FMRI and Fast Diffusion Imaging. PLoS ONE 2010; 5:e15710.

[11] Palmer OR, Chiu CB, Cao A, Scheven UM, Diaz JA, Greve JM. In vivo characterization of the murine venous system before and during dobutamine stimulation: implications for preclinical models of venous disease. Annals of Anatomy 2017;214:43–52.

[12] Crouch AC, Manders AB, Cao AA, Scheven UM, Greve JM. Cross-sectional area of the murine aorta linearly increases with increasing core body temperature. International Journal of Hyperthermia 2018;34:1121–1133.

[13] Castle PE, Scheven UM, Crouch AC, Cao AA, Goergen CJ, Greve JM. Anatomical location, sex, and age influence murine arterial circumferential cyclic strain before and during dobutamine infusion. Journal of Magnetic Resonance Imaging 2019;49:69–80.

[14] Crouch AC, Cao AA, Scheven UM, Greve JM. In Vivo MRI Assessment of Blood Flow in Arteries and Veins from Head-to-Toe Across Age and Sex in C57BL/6 Mice. Annals of Biomedical Engineering 2019. doi: 10.1007/s10439-019-02350-w.

[15] Palmer OR, Braybrooks GG, Cao AA, Diaz JA, Greve JM. Collateral vein dynamics in mouse models of venous thrombosis: Pathways consistent with humans. Thrombosis Research 2019;182:116–123.

[16] Anderson WA. Electrical current shims for correcting magnetic fields. Review of Scientific Instruments 1961;32:241–250.

[17] Nishimura DG. Principles of Magnetic Resonance Imaging. ; 1996.

[18] Scheffler K, Lehnhardt S. Principles and applications of balanced SSFP techniques. European Radiology 2003;13:2409–2418.

[19] Zur Y, Wood ML, Neuringer LJ. Motion-insensitive, steady-state free precession imaging. Magnetic Resonance in Medicine 2005;16:444–459.

[20] Bangerter NK, Hargreaves BA, Vasanawala SS, Pauly JM, Gold GE, Nishimura DG. Analysis of multiple-acquisition SSFP. Magnetic Resonance in Medicine 2004;51:1038–1047.

[21] Elliott AM, Bernstein MA, Ward HA, Lane J, Witte RJ. Nonlinear averaging reconstruction method for phase-cycle SSFP. Magnetic Resonance Imaging 2007;25:359–364.

[22] Çukur T, Lustig M, Nishimura DG. Multiple-profile homogeneous image combination: Application to phase-cycled SSFP and multicoil imaging. Magnetic Resonance in Medicine 2008;60:732–738.

[23] Jung KJ. Synthesis methods of multiple phase-cycled SSFP images to reduce the band artifact and noise more reliably. Magnetic Resonance Imaging 2010; 28:103–118.

[24] Cukur T. Accelerated phase-cycled SSFP imaging with compressed sensing. IEEE Transactions on Medical Imaging 2015;34:107–115.

[25] Wang Y, Shao X, Martin T, Moeller S, Yacoub E, Wang DJ. Phase-cycled simultaneous multislice balanced SSFP imaging with CAIPIRINHA for efficient banding reduction. Magnetic Resonance in Medicine 2016;76:1764–1774.

[26] Ilicak E, Senel LK, Biyik E, Çukur T. Profile-encoding reconstruction for multiple-acquisition balanced steady-state free precession imaging. Magnetic Resonance in Medicine 2017;78:1316–1329.

[27] Schär M, Kozerke S, Fischer SE, Boesiger P. Cardiac SSFP Imaging at 3 Tesla. Magnetic Resonance in Medicine 2004;51:799–806.

[28] Bandettini PA, Wong EC, Hinks RS, Tikofsky RS, Hyde JS. Time course EPI of human brain function during task activation. Magnetic Resonance in Medicine 1992;25:390–397.

[29] Glover GH. Overview of functional magnetic resonance imaging 2011. doi: 10.1016/j.nec.2010.11.001.

[30] Luo Q, Gao JH. Modeling magnitude and phase neuronal current MRI signal dependence on echo time. Magnetic Resonance in Medicine 2010;64:1832–1837.

[31] Scheffler K, Seifritz E, Bilecen D, Venkatesan R, Hennig J, Deimling M, Haacke EM. Detection of BOLD changes by means of a frequency-sensitive trueFISP technique: Preliminary results. NMR in Biomedicine 2001;14:490–496.

[32] Miller KL, Hargreaves BA, Lee J, Ress D, DeCharms RC, Pauly JM. Functional brain imaging using a blood oxygenation sensitive steady state. Magnetic Resonance in Medicine 2003;50:675–683.

[33] Noll DC, Schneider W. Theory, simulation, and compensation of physiological motion artifacts in functional MRI. In Proceedings - International Conference on Image Processing, ICIP, 1994, volume 3. pp. 40–44. doi: 10.1109/ICIP.1994.413892.

[34] Van de Moortele PF, Pfeuffer J, Glover GH, Ugurbil K, Hu X. Respiration-induced Bo fluctuations and their spatial distribution in the human brain at 7 Tesla. Magnetic Resonance in Medicine 2002;47:888–895.

[35] Murphy K, Birn RM, Bandettini PA. Resting-state fMRI confounds and cleanup. NeuroImage 2013;80:349–359.

[36] Zhao X, Bodurka J, Jesmanowicz A, Li SJ. B0-fluctuation-induced temporal variation in EPI image series due to the disturbance of steady-state free precession. Magnetic Resonance in Medicine 2000;44:758–765.

[37] Lange T, Zaitsev M, Buechert M. Correction of frequency drifts induced by gradient heating in 1H spectra using interleaved reference spectroscopy. Journal of Magnetic Resonance Imaging 2011;33:748–754.

[38] Hu X, Le TH, Parrish T, Erhard P. Retrospective estimation and correction of physiological fluctuation in functional MRI. Magnetic Resonance in Medicine 1995;34:201–212.

[39] Glover GH, Li TQ, Ress D. Image-based method for retrospective correction of physiological motion effects in fMRI: RETROICOR. Magnetic Resonance in Medicine 2000;44:162–167.

[40] Human Connectome Project. HCP 3T Imaging Protocol Overview 2019. http://protocols.humanconnectome.org/HCP/3T/imaging-protocols.html.

[41] Behzadi Y, Restom K, Liau J, Liu TT. A component based noise correction method (CompCor) for BOLD and perfusion based fMRI. NeuroImage 2007; 37:90–101.

[42] Thomas CG, Harshman RA, Menon RS. Noise reduction in BOLD-based fMRI using component analysis. NeuroImage 2002;17:1521–1537.

[43] Beissner F, Schumann A, Brunn F, Eisenträger D, Bär KJ. Advances in functional magnetic resonance imaging of the human brainstem. NeuroImage 2014; 86:91–98.

[44] Perlbarg V, Bellec P, Anton JL, Pélégrini-Issac M, Doyon J, Benali H. CORSICA: correction of structured noise in fMRI by automatic identification of ICA components. Magnetic Resonance Imaging 2007;25:35–46.

[45] Churchill NW, Yourganov G, Spring R, Rasmussen PM, Lee W, Ween JE, Strother SC. PHYCAA: Data-driven measurement and removal of physiological noise in BOLD fMRI. NeuroImage 2012;59:1299–1314.

[46] Churchill NW, Strother SC. PHYCAA+: An optimized, adaptive procedure for measuring and controlling physiological noise in BOLD fMRI. NeuroImage 2013;82:306–325.

[47] Ward HA, Riederer SJ, Grimm RC, Ehman RL, Felmlee JP, Jack CR. Prospective multiaxial motion correction for fMRI. Magnetic Resonance in Medicine 2000;43:459–469.

[48] Thesen S, Heid O, Mueller E, Schad LR. Prospective acquisition correction for head motion with image-based tracking for real-time fMRI. Magnetic Resonance in Medicine 2000;44:457–465.

[49] Schulz J, Siegert T, Bazin PL, Maclaren J, Herbst M, Zaitsev M, Turner R. Prospective slice-by-slice motion correction reduces false positive activations in fMRI with task-correlated motion. NeuroImage 2014;84:124–132.

[50] Speck O, Hennig J, Zaitsev M. Prospective real-time slice-by-slice motion correction for fMRI in freely moving subjects. Magnetic Resonance Materials in Physics, Biology and Medicine 2006;19:55–61.

[51] Lee CC, Grimm RC, Manduca A, Felmlee JP, Ehman RL, Riederer SJ, Jack CR. A prospective approach to correct for inter-image head rotation in FMRI. Magnetic Resonance in Medicine 1998;39:234–243.

[52] Verma T, Cohen-Adad J. Effect of respiration on the B0 field in the human spinal cord at 3T. Magnetic Resonance in Medicine 2014;72:1629–1636.

[53] Sutton BP, Noll DC, Fessler JA. Dynamic field map estimation using a spiral-in/spiral-out acquisition. Magnetic Resonance in Medicine 2004;51:1194–1204.

[54] Noll DC, Fessler JA, Sutton BP. Conjugate phase MRI reconstruction with spatially variant sample density correction. IEEE Transactions on Medical Imaging 2005;24:325–336.

[55] Hofer DC. NMR field frequency lock system 1978.

[56] Henry PG, van de Moortele PF, Giacomini E, Nauerth A, Bloch G. Field-frequency locked in vivo proton MRS on a whole-body spectrometer. Magnetic Resonance in Medicine 1999;42:636–642.

[57] Lee J, Santos JM, Conolly SM, Miller KL, Hargreaves BA, Pauly JM. Respiration-induced B0 field fluctuation compensation in balanced SSFP: Real-time approach for transition-band SSFP fMRI. Magnetic Resonance in Medicine 2006;55:1197–1201.

[58] Van Gelderen P, de Zwart J, Starewicz P, Hinks R, Duyn J. Real-time shimming to compensate for respiration-induced B0 fluctuations. Magnetic Resonance in Medicine 2007;57:362–368.

[59] Barmet C, Wilm BJ, Kasper L, Ruff CC, Stephan KE, Pruessmann KP. fMRI with concurrent magnetic field monitoring. In ISMRM 19th Annual Meeting, 2011. p. 3609.

[60] Duerst Y, Wilm BJ, Dietrich BE, Vannesjo SJ, Barmet C, Schmid T, Brunner DO, Pruessmann KP. Real-time feedback for spatiotemporal field stabilization in MR systems. Magnetic Resonance in Medicine 2015;73:884–893.

[61] Guo S, Noll DC. Comparison of Oscillating Steady State to GRE BOLD for fMRI. In ISMRM 27th Annual Meeting, 2019. p. 1170.

[62] Miller KL. FMRI using balanced steady-state free precession (SSFP). NeuroImage 2012;62:713–9.

[63] Parker DL, Gullberg GT. Signal-to-noise efficiency in magnetic resonance imaging. Medical Physics 1990;17:250–257.

[64] Logothetis NK. What we can do and what we cannot do with fMRI 2008. doi: 10.1038/nature06976.

[65] Hayasaka S, Laurienti PJ. Comparison of characteristics between region-and voxel-based network analyses in resting-state fMRI data. NeuroImage 2010; 50:499–508.

[66] Goense J, Bohraus Y, Logothetis NK. fMRI at high spatial resolution implications for BOLD-models. Frontiers in Computational Neuroscience 2016;10.

[67] Feinberg DA, Cvetesic N, Beckett A. Pushing the limits of ultra-high resolution human brain imaging with SMS-EPI demonstrated for columnar level fMRI. NeuroImage 2018;164:155–163.

[68] Bullmore E, Brammer M, Williams SCR, Rabe-Hesketh S, Janot N, David A, Mellers J, Howard R, Sham P. Statistical methods of estimation and inference for functional MR image analysis. Magnetic Resonance in Medicine 1996; 35:261–277.

[69] Monti M. Statistical Analysis of fMRI Time-Series: A Critical Review of the GLM Approach. Frontiers in Human Neuroscience 2011;5.

[70] Lund TE, Madsen KH, Sidaros K, Luo WL, Nichols TE. Non-white noise in fMRI: Does modelling have an impact? NeuroImage 2006;29:54–66.

[71] Hargreaves BA, Vasanawala SS, Pauly JM, Nishimura DG. Characterization and reduction of the transient response in steady-state MR imaging. Magnetic Resonance in Medicine 2001;46:149–158.

[72] Zur Y, Wood ML, Neuringer LJ. Spoiling of transverse magnetization in steady-state sequences. Magnetic Resonance in Medicine 1991;21:251–263.

[73] Foxall DL. Frequency-Modulated Steady-State Free Precession Imaging. Magnetic Resonance in Medicine 2002;48:502–508.

[74] Benkert T, Ehses P, Blaimer M, Jakob PM, Breuer FA. Dynamically phase-cycled radial balanced SSFP imaging for efficient banding removal. Magnetic Resonance in Medicine 2015;73:182–194.

[75] Benkert T, Ehses P, Blaimer M, Jakob PM, Breuer FA. Fast isotropic banding-free bSSFP imaging using 3D dynamically phase-cycled radial bSSFP (3D DYPR-SSFP). Zeitschrift fur Medizinische Physik 2016;26:63–74.

[76] Slawig A, Wech T, Ratz V, Tran-Gia J, Neubauer H, Bley T, Köstler H. Multi-frequency reconstruction for frequency-modulated bSSFP. Magnetic Resonance in Medicine 2017;78:2226–2235.

[77] Slawig A, Wech T, Ratz V, Neubauer H, Bley T, Köstler H. Frequency-modulated bSSFP for phase-sensitive separation of water and fat. Magnetic Resonance Imaging 2018;53:82–88.

[78] Datta A, Nishimura DG, Baron CA. Banding-free balanced SSFP cardiac cine using frequency modulation and phase cycle redundancy. Magnetic Resonance in Medicine 2019;82:1604–1616.

[79] Roeloffs V, Rosenzweig S, Holme HCM, Uecker M, Frahm J. Frequency-modulated SSFP with radial sampling and subspace reconstruction: A time-efficient alternative to phase-cycled bSSFP. Magnetic Resonance in Medicine 2019;81:1566–1579.

[80] Björk M, Ingle RR, Gudmundson E, Stoica P, Nishimura DG, Barral JK. Parameter estimation approach to banding artifact reduction in balanced steady-state free precession. Magnetic Resonance in Medicine 2014;72:880–892.

[81] Xiang QS, Hoff MN. Banding artifact removal for bSSFP imaging with an elliptical signal model. Magnetic Resonance in Medicine 2014;71:927–933.

[82] Hoff MN, Andre JB, Xiang QS. Combined geometric and algebraic solutions for removal of bSSFP banding artifacts with performance comparisons. Magnetic Resonance in Medicine 2017;77:644–654.

[83] Fessler JA. Michigan Image Reconstruction Toolbox (MIRT) 2019. https://web.eecs.umich.edu/∼fessler/code/.

[84] Wansapura JP, Holland SK, Dunn RS, Ball WS. NMR relaxation times in the human brain at 3.0 tesla. Journal of Magnetic Resonance Imaging 1999; 9:531–538.

[85] Nielsen JF, Noll DC. TOPPE: A framework for rapid prototyping of MR pulse sequences. Magnetic Resonance in Medicine 2018;79:3128–3134.

[86] Buehrer M, Pruessmann KP, Boesiger P, Kozerke S. Array compression for MRI with large coil arrays. Magnetic Resonance in Medicine 2007;57:1131–1139.

[87] Webster JG, Vilanova R, Visioli A. The Proportional-Integral-Derivative (PID) Controller. In Wiley Encyclopedia of Electrical and Electronics Engineering, John Wiley & Sons, Inc., 2017, pp. 1–15. doi: 10.1002/047134608x.w1033.pub2.

[88] Cardiovascular diseases (CVDs). https://www.who.int/news-room/fact-sheets/detail/cardiovascular-diseases-(cvds).

[89] Schaper W, Schaper J. Arteriogenesis, volume 17 of Basic Science for the Cardiologist. Boston, MA: Springer US; 2004. doi: 10.1007/b111191.

[90] Heil M, Wagner S, Schaper W. Arterial regeneration by collateral artery growth (arteriogenesis). Drug Discovery Today: Disease Models 2004;1:265–271.

[91] Heil M, Eitenmüller I, Schmitz-Rixen T, Schaper W. Arteriogenesis versus angiogenesis: similarities and differences. Journal of Cellular and Molecular Medicine 2006;10:45–55.

[92] Werner GS. Collaterals: how important are they? Heart 2007;93:778–779.

[93] Palmer-Kazen U, Wahlberg E. Arteriogenesis in Peripheral Arterial Disease. Endothelium 2003;10:225–232.

[94] Heil M, Ziegelhoeffer T, Wagner S, Fernández B, Helisch A, Martin S, Tribulova S, Kuziel WA, Bachmann G, Schaper W. Collateral Artery Growth (Arteriogenesis) After Experimental Arterial Occlusion Is Impaired in Mice Lacking CC-Chemokine Receptor-2. Circulation Research 2004;94:671–677.

[95] Limbourg A, Korff T, Napp LC, Schaper W, Drexler H, Limbourg FP. Evaluation of postnatal arteriogenesis and angiogenesis in a mouse model of hind-limb ischemia. Nature protocols 2009;4:1737–46.

[96] Greve JM, Chico TJ, Goldman H, Bunting S, Peale FV, Daugherty A, van Bruggen N, Williams SP. Magnetic resonance angiography reveals therapeutic enlargement of collateral vessels induced by VEGF in a murine model of peripheral arterial disease. Journal of magnetic resonance imaging : JMRI 2006; 24:1124–32.

[97] Wagner S, Helisch A, Bachmann G, Schaper W. Time-of-flight quantitative measurements of blood flow in mouse hindlimbs. Journal of magnetic resonance imaging : JMRI 2004;19:468–74.

[98] Meisner JK, Niu J, Sumer S, Price RJ. Trans-illuminated laser speckle imaging of collateral artery blood flow in ischemic mouse hindlimb. Journal of biomedical optics 2013;18:096011.

[99] Veal JR. The mode of development of collateral venous circulation in the extremities. American Heart Journal 1940;19:275–282.

[100] Beckman MG, Hooper WC, Critchley SE, Ortel TL. Venous Thromboembolism. A Public Health Concern 2010. doi: 10.1016/j.amepre.2009.12.017.

[101] Diaz JA, Obi AT, Myers DD, Wrobleski SK, Henke PK, Mackman N, Wakefield TW. Critical review of mouse models of venous thrombosis. Arteriosclerosis, thrombosis, and vascular biology 2012;32:556–62.

[102] Parker DL, Yuan C, Blatter DD. MR angiography by multiple thin slab 3D acquisition. Magnetic Resonance in Medicine 1991;17:434–451.

[103] Jacoby C, Böring YC, Beck A, Zernecke A, Aurich V, Weber C, Schrader J, Flögel U. Dynamic changes in murine vessel geometry assessed by high-resolution magnetic resonance angiography: A 9.4T study. Journal of Magnetic Resonance Imaging 2008;28:637–645.

[104] Diaz JA, Hawley AE, Alvarado CM, Berguer AM, Baker NK, Wrobleski SK, Wakefield TW, Lucchesi BR, Myers DD. Thrombogenesis with continuous blood flow in the inferior vena cava. A novel mouse model. Thrombosis and haemostasis 2010;104:366–75.